TESE DE DOUTORAMENTO

FISSION DYNAMICS INVESTIGATED IN INVERSE KINEMATICS IN REACTIONS INDUCED BY RELATIVISTIC ^{236}U PROJECTILES

Manuel Feijoo Rodríguez

ESCOLA DE DOUTORAMENTO INTERNACIONAL DA UNIVERSIDADE DE SANTIAGO DE COMPOSTELA

PROGRAMA DE DOUTORAMENTO EN FÍSICA NUCLEAR E DE PARTÍCULAS

SANTIAGO DE COMPOSTELA

2021

USC
UNIVERSIDADE
DE SANTIAGO
DE COMPOSTELA

DECLARACIÓN DO AUTOR DA TESE

FISSION DYNAMICS INVESTIGATED IN INVERSE KINEMATICS IN REACTIONS INDUCED BY RELATIVISTIC 236U PROJECTILES

D. Manuel Feijoo Rodríguez

Presento a miña tese, seguindo o procedemento axeitado ao Regulamento, e declaro que:

1) A tese abarca os resultados da elaboración do meu traballo.
2) De selo caso, na tese faise referencia ás colaboracións que tivo este traballo.
3) A tese é a versión definitiva presentada para a súa defensa e coincide coa versión enviada en formato electrónico.
4) Confirmo que a tese non incorre en ningún tipo de plaxio doutros autores nin de traballos presentados por min para a obtención doutros títulos.

En Santiago de Compostela, a 06 de Maio de 2021

Asdo. Manuel Feijoo Rodríguez

USC
UNIVERSIDADE
DE SANTIAGO
DE COMPOSTELA

AUTORIZACIÓN DO DIRECTOR / TITOR DA TESE

FISSION DYNAMICS INVESTIGATED IN INVERSE KINEMATICS IN REACTIONS INDUCED BY RELATIVISTIC 236U PROJECTILES

D./Dna. José Fernando Benlliure Anaya
D./Dna. José Luis Rodríguez Sánchez

INFORMA/N:

Que a presente tese, correspóndese co traballo realizado por D. Manuel Feijoo Rodríguez , baixo a miña dirección, e autorizo a súa presentación, considerando que reúne os requisitos esixidos no Regulamento de Estudos de Doutoramento da USC, e que como director desta non incorre nas causas de abstención establecidas na Lei 40/2015.

.

En Santiago de Compostela, a 06 de Maio de 2021

USC
UNIVERSIDADE
DE SANTIAGO
DE COMPOSTELA

Agradecimientos

El trabajo realizado durante este tiempo hubiese sido mucho más complicado sin el apoyo, ayuda y consejo de muchas personas, dentro y fuera del ámbito laboral. Es momento, por tanto, de expresar mi agradecimiento a todas ellas. Me gustaría decir que intentaré ser breve, pero para una vez que tengo la oportunidad, lo que intentaré será decir lo que me apetezca y no olvidarme de nadie. Y no ser demasiado intenso...

Me gustaría empezar mencionando a Pepe y José Luis, mis dos directores de tesis, por todo el esfuerzo realizado para que este trabajo saliese adelante. A ellos les agradezco todas las horas que han dedicado, la confianza que han depositado en mí y el buen trato que siempre me han dado. Con el permiso de Pepe, me gustaría remarcar la labor de José Luis, por su paciencia y por haberse involucrado activamente desde mucho antes de entrar como director. Espero que estéis tan satisfechos de este trabajo como lo estoy yo.

Quisiera agradecer también al resto de compañeros de trabajo que he tenido durante estos años. Gracias a Lola por elegirme para este puesto a través de la FPI. A Héctor y Pablo por echarme una mano cuando R3BRoot se me atascaba. A todos los compañeros de despacho que he tenido por las risas y cafés que nos tomábamos cuando la pandemia lo permitía. Hago extensivo también mi agradecimiento al resto de compañeros de la parte de nuclear y a todos con los que he podido compartir la enriquecedora labor de la docencia, sin duda de lo más gratificante que me llevo de esta etapa.

I would also like to thank the colleagues from the SOFIA collaboration, the CALIFA team and other members of the GSI. The fruitful physical discussions we have been able to share have definitely helped to the development and progress of this work. I am also grateful to the GSI organization for giving me the chance of stay there for a total of 5 months and participate in top-class nuclear physics experiments.

Teño a sorte de contar cun entorno familiar que sempre me apoiou, sen o cal esta etapa, e calquera outra, sería moito máis complicada e aburrida. A

miña nai e miña irmá Caro, por sempre facerme sentir querido. Por coidarme, apoiarme constantemente e estar orgullosas de min. Por saber que sempre poderei contar con vós para o que necesite. Sabedes que vós comigo tamén. A miña avoa Carolina, pola súa bondade e por estar cada día máis nova, aínda que ela diga o contrario. Aos meus tíos e primos, polo cariño que sempre me transmiten. A Carlos e Inma, por aguantarme 77 soles.

Gustaríame facer unha pequena mención ás persoas que non puideron acompañarme todo o que eu quixera e a bo seguro que estarían felices de verme chegar ata aquí. A meu pai, meus avós e, sobre todo, a meu tío Po, de quen tanto me lembro.

Parte importante de este éxito se lo debo a las amistades que han estado conmigo desde mucho antes de empezar la tesis. A mis amigos de Física, por haber compartido, carrera, máster, doctorado, unos buenos perros, tremendas turras por Whatsapp y otras cosas que será mejor guardárselas para distinta ocasión. Y más que nos quedan, cómo se viene. A mis amigos de Medicina, porque aunque ahora nuestros caminos se hayan separado un poco, todos los momentos que hemos pasado juntos los tengo muy presentes y los llevo siempre conmigo. Espero seguir contando con vosotros en el futuro (como amigos mejor que como médicos, a poder ser). No me puedo olvidar de los que están ahí desde antes de tener uso de razón, que son mis amigos de Monforte. Da igual el tiempo que pase, siempre tengo la sensación cuando nos juntamos de que todo está como siempre, como si no pasase el tiempo, y eso me da la vida. A todos ellos, espero que pronto podamos celebrarlo como se merece, que ya lo echo de menos.

A María. He escrito, borrado y vuelto a escribir muchas veces este párrafo y he llegado a la conclusión de que nada de lo que diga va a hacer justicia a todo lo que haces por mí, pero lo voy a intentar. Cuando empecé esta etapa tenía distintas ilusiones, planes y expectativas. Pero el haberte conocido supera, con mucho, cualquiera de ellas. Esa no la vi venir. Gracias por nuestro día a día, por los viajes que hemos hecho y nos quedan por hacer, por aguantarme (sabes que hago lo que puedo), por compartir nuestra felicidad y hacerme mirar al futuro siempre con optimismo. En definitiva, gracias por quererme como lo haces. Espero que esta etapa lleve a otra mejor y así sucesivamente, por lo menos, 100 años más. *Prefiero verte que ganar la guerra.*

Y ya está. Al final sí he sido breve. Creo. E intenso. Os animo a que sigais leyendo a partir de aquí, aunque reconozco que no es lectura ligera. Avisados estáis.

USC
UNIVERSIDADE
DE SANTIAGO
DE COMPOSTELA

Contents

USC UNIVERSIDADE DE SANTIAGO DE COMPOSTELA

Introduction

The origin of nuclear physics as an independent field of knowledge can be dated to 1 March 1896 when Henri Becquerel discovered radioactivity [1]. Becquerel found out that uranium salts generated black tracks on photographic plates. The radiation responsible was first interpreted as penetrating UV-radiation since W. Rontgen had discovered x-rays a year before. Marie Curie later introduced the word radioactivity to define this phenomenon. The posterior development and evolution of nuclear physics is closely related to the discovery of the atomic nucleus. The discovery of the electron by J. J. Thomson at the end of the 19th century led the way to other significant discoveries such as the forementioned atomic nucleus, where the positive charge of the atom is concentrated, by Rutherford (1911) or the transmutations of elements (1919) [2]. However, the atomic nucleus knowledge was misunderstood until 1932, when J. Chadwick proved the existence of a massive particle similar to protons but with spin $\frac{1}{2}$ and isospin $-\frac{1}{2}$, which was named neutron. This breakthrough furnished scientists with a particle able to penetrate atomic nuclei without expenditure of large amounts of energy. From 1934 to 1939, investigations of the reaction between a neutron and uranium were carried out by several scientists, culminating with the discovery of nuclear fission by O. Hahn, F. Strassman, L. Meitner and O.R. Frisch [3, 4].

Nuclear fission is commonly explained as the process by which a heavy nucleus splits into two fragments of comparable mass, as a consequence of the large-scale collective motion of nuclear constituents. The evolution of the fission process depends on the initial conditions of the fissioning system (such as its excitation energy, angular momentum and shape) and on the form of its potential energy as a function of the deformation and mass asymmetry. Thus, fission results to be a particularly complex reaction mechanism still lacking of a satisfactory and complete microscopic description. First theoretical explanation of the fission process was early given by Bohr and Wheeler [5] on the basis of the liquid-drop model but further research carried out along the 20th century revealed, through the investigation of new experimental

observables, that the evolution of the fissioning system can not be fully explained in terms of statistical approaches and pointed out the requirement of dynamical descriptions. These dynamical models should take into account the coupling between the intrinsic and collective excitations of the nuclear constituents as well as a realistic description of the nuclear structure. However, the amount of degrees of freedom involved in the process still makes the complete microscopical description of the dynamical evolution of the interacting nucleons a challenge for nuclear theory [6].

To address this limitation, time dependent mean-field approaches, such as Hartree-Fock technique has recently allowed for considerable progress in the quasi-microscopic description of the process [7]. Other alternatives find their support in the use of transport theories based on Fokker-Plank or Langevin equations [8]. The evolution of this kind of approaches allows to describe with good accuracy relevant features of deeply inelastic heavy-ion collisions. In this case, a dissipation coefficient (β, in units of s^{-1}) is introduced to couple the intrinsic and collective degrees of freedom allowing to study how the internal excitation energy is transformed into deformation energy between the initial excited states at small nuclear deformation and the scission point, in which the fissioning system breaks into the two fission fragments [9]. This will be the main approximation followed in the present work as these model calculations provide a satisfactory description of the fission process although the exact value of the nuclear dissipation coefficient and its possible dependence on temperature and deformation are still open questions [10, 11].

In last decades, it was demonstrated that nuclear fission plays a significant role in the rapid-neutron capture process (r-process) in stellar nucleosynthesis [12]. The r-process consists of consecutive neutron capture and beta decay in an environment with high neutron flux, which has not been completely identified for long [13, 14]. In particular, the importance of fission inside this process lies on the phenomena known as fission cycling, which limits the mass range of the r-process path having a direct impact on nuclide abundance. A correct understanding of the fission process itself will allow to provide a more accurate model description of the observed nuclei abundances in the Universe [15, 16]. It is also worth to mention the implication of nuclear fission in several aspects of the society, highlighting its use in nuclear reactors to generate energy [17] or in medicine for the production of medical radiotracers [18]. Furthermore, fission at high excitation energies is also extremely important for the development of spallation neutron sources in Accelerator Driven System (ADS) technologies [19].

The experimental investigation of fission is neither exempt of difficulties.

First experiments, yielding isotopic distributions, were performed using the direct kinematics technique, at the mass spectrometer Lohengrin [20] based on thermal-neutron induced reactions [21]. This technique only allowed for the identification in atomic and mass number of the light fission fragments due to the fact that the velocities of the heavy ones were too small to measure the atomic number with precision. It was not until the end of the 1990s decade, with the development of heavy ion accelerators, when the inverse kinematics technique started to be used [22]. In this experimental technique the heavy nucleus undergoing fission is accelerated up to relativistic energies. While in the direct kinematics technique the fission fragments are almost back-to-back released in the laboratory frame, in inverse kinematics they are emitted in a narrow cone in forward direction, and with considerably higher velocities, making its detection much easier. First measurements based on this technique were performed at the GSI facilities using the FRS spectrometer [23], where only one of the two fragments was detected and identified in atomic and mass number. Later, the novel experiment carried out by K.H. Schmidt and collaborators [24] provided for the first time the identification of both fragments in atomic number. Recently, similar experiments have also been carried out at the GANIL facility using transfer- and fusion-induced fission reactions in inverse kinematics, being able to completely identify one of the fission fragments in charge and mass, while the other one was only identified in atomic number [25, 26]. In the last few years, the SOFIA [27, 28] collaboration made an incredible effort to overcome the restrictions of conventional fission experiments in order to obtain complete isotopic identification of both fission fragments.

In this work, we propose to use the inverse kinematics technique and the SOFIA experimental setup to study dissipative effects in the fission process measuring reactions induced by projectiles of ^{236}U at 720A MeV in thick uranium and aluminum targets. One of the driving ideas for this work is to complete the investigation carried out by J.L. Rodriguez-Sanchez [29], where the dissipative effects were studied using the reaction ^{208}Pb+p at 500A MeV. The main conclusion of this work is that the diffusion process until the saddle point and the dissipative process from saddle to scission could be described by using similar values for the dissipation parameter coupling intrinsic and collective degrees of freedom.

The range of initial excitation energies covered with the reaction ^{208}Pb+p at 500A MeV is rather large. However, the range in deformation is limited. We propose then to extend the range in deformation by using ^{236}U projectiles. The SOFIA experimental setup will allow to determine the atomic and mass number of the fission fragments, giving access to relevant observables in order

to constrain the value of the dissipation parameter and to investigate its eventual dependence on deformation. Other works have explored the fission dynamics for the presaddle stage using uranium isotopes like ^{238}U [30] or ^{234}U [31]. The complete identification of the fission fragments will allow us to extend this study and address the postsaddle dynamics. We will also study the role of the angular momentum gained by the prefragment after the collision and the level densities of the deformed nuclei in the description of the fission process.

One of the main limitations of fission investigations in inverse kinematics is the poor characterization of the initial state of the fissioning system in terms of isotopic composition, excitation energy and angular momentum. To partially overcome this limitation, in the second part of this work we propose an upgrade of this experimental approach. In order to get a better control of the first stage of the reaction, we present a conceptual proposal to induce fission using quasi-free *(p,2p)* reactions [32]. Coupling the SOFIA fission detection setup with the R^{3}B detectors, namely the CALIFA [33] calorimeter and a Silicon tracker, the four-momentum of the two outgoing protons would be measured with relative good accuracy. The momenta of the outgoing protons will give us for the first time access to the excitation energy of the fissioning system by using the missing mass method. Simultaneously, the SOFIA setup will allow us to identify in atomic and mass number the two fission fragments produced by the decay of the remnant compound nucleus. Thus, this novel experiment will provide us new possibilities for a complete experimental characterization of the fission process.

The structure of the present dissertation is organized as follows: Chapter 1 reviews the present understanding of fission, focusing on its dynamical features and different approaches to describe the evolution of the fissioning system. Additionally, the most important observables sensitive to dissipation are discussed. Chapter 2 is devoted to present the experimental methodology used in this work to measure and characterize both fission fragments. Precise details of each detector behaviour and information about the calibrations needed to determine the atomic and mass number of the fission fragments are provided. Chapter 3 is dedicated to the analysis and interpretation of obtained results. We will compare our results to existing data and to model calculations to study the dynamical properties of the fission process. Chapter 4 is focused on the search of new ideas to study fission, in particular, the use of *(p,2p)* quasi-free scattering reactions to induce fission. Advanced simulations are carried out, whose results shed valuable information for the fission experiments performed during the 2021 GSI experimental campaign. Finally, the main results of this work are summarized in the conclusions.

USC
UNIVERSIDADE
DE SANTIAGO
DE COMPOSTELA

Chapter 1

Present understanding of fission

The main objective of this chapter is to compile the most relevant features about the dynamics of the fission process, specially at high excitation energies. The first and second sections of this chapter provide a brief description of the present understanding of the nuclear fission process, introducing the most important ingredients of the fission mechanism. Section 1.3 gives an overview of the most used observables for the investigation of the fission process dynamics. Finally, we describe in section 1.4 the investigation proposed in this work.

1.1 The fission process: general overview

Fission is a complex nuclear reaction consisting in the split of a heavy nucleus in two lighter fragments as a consequence of a large-scale collective motion of the nucleons. The transition of the fissioning system from its excited initial state until it breaks into two fragments can be described as a two-step process. Firstly, the fissioning nucleus, that has gained some excitation energy due to a nuclear collision, deforms until it reaches to the top of the fission barrier, at the so-called saddle point. During this deformation process, the competition between the surface energy and the Coulomb energy defines the fission barrier. The surface energy increases with the deformation of the nuclear system while the Coulomb energy decreases, being the total energy of the system the sum of both quantities. At the beginning of the fission process the surface energy increases faster than the Coulomb energy, making the total energy positive until reaching the saddle point. At this moment, the Coulomb energy starts to decrease much faster, so the total energy reaches a maximum and then starts to go down. When the nuclear system passes the saddle point, the fission process becomes irreversible. After

that, the system deforms until it arrives to the scission point where the two fission fragments are formed sharing the excitation energy available at this point [34]. Finally, Coulomb repulsion accelerates both fragments until they are completely split and their corresponding deexcitation chains are followed until their excitation energies fall below the lowest particle-emission threshold.

In the study of the fission process, a division between its static and dynamical properties can be done. The static properties are those defined by the potential energy governing this process according to the degrees of freedom relevant for fission, mainly the quadrupole moment and the mass asymmetry. The dynamical properties are related to the energy released in the process and the timescales involved. The fission time can be divided into two main components: the time to reach the saddle point and the saddle-to-scission time. These timescales depend on the isotopic composition and excitation energy of the fissioning nuclei, being the total fission time around $10^{-19} - 10^{-20} s$ [10].

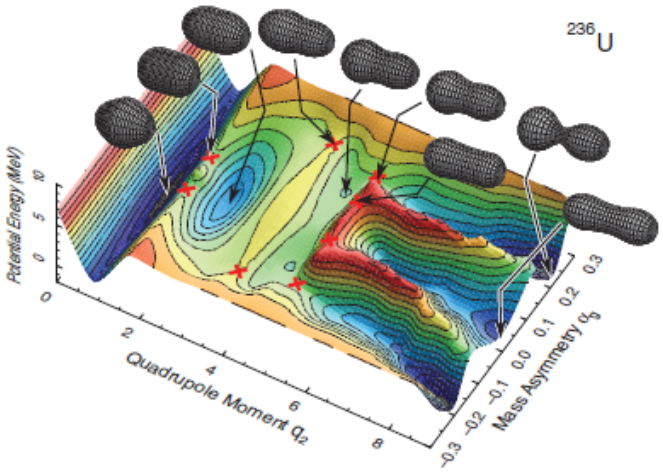

Figure 1.1: *Potential energy landscape for ^{236}U as a function of the quadrupole moment and mass asymmetry. Red crosses indicate the location of different saddle points. Figure taken from [35].*

The initial conditions of the fissioning system, namely its atomic and mass number, excitation energy and angular momentum, are relevant to determine how the system will evolve. As shown in figure 1.1, the evolution of the process is guided by the form of its potential energy landscape that is a

function of the deformation, represented by the quadrupole moment, and the mass asymmetry. To reach the saddle point, where fission will be decided, the fissioning system needs to overcome the fission barrier. Depending on the quadrupole coordinate and the mass asymmetry, the saddle point will be placed in different spots marked by the red crosses in figure 1.1. Additionally, the population of the different valleys represented in the potential landscape depends on the initial excitation energy gained by the compound nucleus with respect to the ground state. The origin of these valleys is due to nuclear shell closure effects. In actinides, lower excitation energies correspond to asymmetric fission modes while high excitation energies result in symmetric contributions. This fact is one of the main differences between fission induced by Coulomb excitation and nuclear fragmentation [4, 36]. The dynamical evolution of the process from the initial state to the scission point involves a complex interplay between single-particle (microscopic) and collective (macroscopic) effects. These degrees of freedom are coupled using a dissipation parameter, that describes the energy transfer between them.

Regarding the experimental investigation of fission, first experiments providing information on the nature of the fission fragments made use of the direct kinematics technique [20]. These experiments showed outstanding results, being able to measure the fission yields as a function of the mass, nuclear charge or kinetic energy of some actinides and pre-actinides. However, this experimental technique presents some intrinsic limitations. First one is the impossibility to access to short-lived fissioning systems. Second, the low velocity acquired by the fragments limits the charge identification to fission fragments with an atomic number below Z=42. The lower velocities acquired by the heavier ones produce charge states fluctuations and prevent their identification. Because of that, the complete identification of both fission fragments can not be achieved using the direct kinematics technique.

To overcome this limitation, in the late 1990s the experimental paradigm changed. The inverse kinematics came up led by the evolution of heavy ion accelerators [22]. Its main advantage comes from the energy boost of the fission fragments, helping to their correct identification. The first measurements were performed at the GSI facility using coulex-, fragmentation- and spallation-induced fission reactions [37]. With the help of the FRS spectrometer, one of the two fission fragments was detected and identified in atomic and mass number. Later, the novel experiment carried out by K.H. Schmidt and collaborators [24] provided the identification of both fragments in atomic number for the first time. Recently, new experiments at GANIL, making use of transfer- and fusion-induced fission

reactions [25, 26], were able to completely identify one of the fission fragments in atomic and mass number, while the other could be identified in atomic number. In the recent years, the SOFIA collaboration [27, 28] designed a novel setup specially focused on fission investigations. This setup, together with the inverse kinematics technique, allowed for the first time a complete identification in atomic and mass number of both fission fragments simultaneously.

1.2 Dynamics of the fission process

The dynamical aspects of the fission process are governed by the motion of the nuclear constituents, the energy released in the coupling between degrees of freedom and the typical timescales that the fissioning systems presents along the fission path. Some of these fission features are often described using fully dynamical microscopic models based on Hartree-Fock methods [38] or macroscopic-microscopic models [39]. However, these theoretical models fail in the prediction of some key observables such as the mass-yield curve due to the complexity of the involved many-body calculations. Moreover, a complete microscopic calculation requires long computing time, even with the use of the most powerful computers.

Due to the fact that fission involves a huge amount of degrees of freedom, the word microscopic should not be treated as an ab initio many-body theory. Fully microscopic or first principle descriptions, sometimes used to characterize particular approaches for systems with a small number of nucleons, can not be used for fission theory, being all these models phenomenological at some level. Thus, the description of the fission process is done with the help of macroscopic variables [16]. In this sense, transport theories can describe the evolution of the fissioning system in terms of intrinsic and collective degrees of freedom. Intrinsic excitations are based on the states of the individual constituents and form a heat bath. Collective modes correspond to the coordinate motion of part or all the nucleons, *ie*, vibrations, rotations and all kind of deformations. The projection of the many-body problem onto a macroscopic scale using the most relevant coordinates introduces the notion of coupling, consisting in the energy exchange between the collective degrees of freedom and the heat bath.

In this sense, dynamical properties will be of utmost importance to describe the coupling between intrinsic and collective degrees of freedom, specifically at high-excitation energies where the effect of dynamics is more evident. Thus, the passage over the saddle point is described as a diffusion

process where the coupling between intrinsic and collective degrees of freedom is parametrized as a function of a dissipation parameter. This dissipation parameter introduces a time delay of the collective motion of the fissioning system, the so-called transient time, owing to the irreversible energy flow from collective modes to intrinsic excitations. The different approaches carried out during the years to describe fission will be presented below, from the early statistical description of the process given by Bohr and Wheeler to the time-dependent models.

1.2.1 The statistical approach by Bohr-Wheeler

During the evolution of the fissioning system from its initial state up to the saddle point, behaving as a compound nucleus, fission decay probabilities are determined from macroscopic variables. On the basis of statistical models, the probability of a specific decay channel i of a compound nucleus with neutron number N, proton number Z and excitation energy E is expressed as:

$$W_i(N,Z,E) = \frac{\Gamma_i(N,Z,E)}{\sum_k \Gamma_k(N,Z,E)} \tag{1.1}$$

where Γ_i is the decay width for a given channel. In the case of an excited compound nucleus, the main decay modes governing its deexcitation process are particle evaporation and fission [40]. Regarding the first, the most precise description is the proposed by Hauser and Fesbach in 1952 [41]. This formalism is used to determine the decay width for neutron or light-charged particle emission. The first accurate description of the fission decay width was portrayed by Bohr and Wheeler in 1939 [5], who based their approach on the statistical model of nuclear reactions and introduced the concept of transition states, in analogy with chemical reactions [42]. The transition states at the fission barrier are populated in thermal equilibrium according to this approach and the fission probability is determined by the passage over these states [43]. Thus, the transition-state fission decay width can be written as follows:

$$\Gamma_{BW} = \frac{1}{2\pi\rho_i(E_i,J_i)} \int d\epsilon \rho_{sad}(E_i - B_f(J_i) - \epsilon) \tag{1.2}$$

being E_i and J_i are the excitation energy and angular momentum of the compound nucleus, ρ_{sad} is the level density at the saddle point, $\mathrm{B}_f(\mathrm{J}_i)$ is the fission barrier height and ϵ is the kinetic energy along the fission path.

Fission barriers are usually described from the spin-dependent ones proposed by Sierk [44]. Regarding the level density at saddle point, the easiest way to calculate it can be done using the Fermi-gas model [45] according to the expression:

$$\rho(E) = \frac{\sqrt{\pi}}{12} \frac{\exp(S)}{a^{1/4} E^{5/4}} \tag{1.3}$$

In this equation, E is the excitation energy of the system and a is the level density parameter, in units of MeV^{-1} that can be calculated using the parametrization obtained by Ignatyuk [46]. S accounts for the entropy of the system, obtained as $S = 2\sqrt{a \cdot E}$.

1.2.2 Kramers' stationary solution

Despite the statistical approach given by Bohr and Wheeler describes rather well the fission probabilities at low excitation energies, similar to the height of the fission barrier, the possible coupling and energy transfer between intrinsic and collective degrees of freedom was not considered. In 1940, Kramers was the first to propose the description of fission as a diffusion process within the framework of transport theories. He suggested that the fission rates calculated by Bohr and Wheeler were too high, due to the slowing down in the motion caused by the energy dissipation from intrinsic to collective degrees of freedom. However, the formulation given by Bohr-Wheeler was very successful interpreting fission experimental results until the experiments carried out by Gavron and collaborators in 1981 [47], where it failed to reproduce the first data on pre-scission neutron multiplicities. This failure was interpreted as an evidence for dissipative effects.

Thus, the evolution of the fissioning nucleus up to the saddle point is described as a diffusion process across the fission barrier. At high-excitation energies, the dissipative effects play an important role in the coupling between intrinsic (excitation energy) and collective (deformation) degrees of freedom. The model proposed by Kramers is based on the description of the fissioning nucleus by the Fokker-Planck type equation of motion, addressing the reduction of the fission width predicted by Bohr and Wheeler (equation 1.2) with the inclusion of the so-called Kramers factor, K. This factor has explicit dependence with the dissipation parameter (β) responsible for coupling intrinsic and collective degrees of freedom, governing the energy transfer between them. Thus, the width predicted by Kramers can be expressed as follows:

$$\Gamma_f^K = \Gamma_{BW} \cdot K = \Gamma_{BW} \cdot \left(\left[1 + \left(\frac{\beta}{2\omega_0} \right)^2 \right]^{\frac{1}{2}} - \frac{\beta}{2\omega_0} \right) \tag{1.4}$$

where ω_0 represents the frequency of the harmonic oscillator describing the potential at the saddle-point deformation.

Thus, this stationary approach describes more accurately the evolution of the fission process. The nucleus motion along the deformation coordinate is slowed down preventing it to cross the saddle point with a certain probability and, therefore, the fission chance is reduced because the nucleus cools down by evaporation.

1.2.3 Time-dependent approaches

Ground-to-saddle dynamics

Until now, the approaches to describe the fission decay width have been based on statistical and stationary assumptions. The results obtained by Gavron and collaborators [47] lead the way to investigate the transient effects on the temporal evolution of the fissioning system. Following the Kramers' work, Weidenmüller [48], Grangé and collaborators [9] used the diffusion model to study how the quasi-stationary flow over the fission barrier is attained. In this case, the dynamics of the fission process can be modelled by using the forementioned transport models based on the Langevin or Fokker-Planck equations (FPE) that in a general form can be written as:

$$\frac{dV}{dt} = -\frac{1}{m}\frac{\partial V(x)}{\partial x} - \beta v - \frac{F(t)}{m} \tag{1.5}$$

where x represents the deformation degree of freedom, V the potential energy landscape, *F(t)* is a stochastic force and β the dissipation parameter.

A numerical solution of the FPE was obtained for the first time to describe the fission process, considering that the initial system presented a spherical shape with high excitation energy (more than 100 MeV) and low angular momentum. Thus, a time-dependent fission decay, $\Gamma_f(t)$, was found by calculating the probability flux across the saddle point. This proved that the fissioning system needs a time delay or transient time until the stationary flux across the fission barrier is reached. This transient time appears only at high excitation energies where the average decay time of the fissioning system is similar to the relaxation time of the fission degrees of freedom, causing a reduction of the fission probability.

In figure 1.2, the fission rates obtained from the transition-state model developed by Bohr-Wheeler (red dotted line) and from Kramers stationary solution (blue dashed line) are shown. Later, in 1986, Bhatt and collaborators [49], proposed an exponential in-growth time-dependent function to describe the fission probability. According to this approach, in the early stage of the process, $\Gamma_f(t)$ is completely suppressed. The transient time is the time interval needed by the fissioning system to reach the 90% of the stationary fission rate described by Kramers.

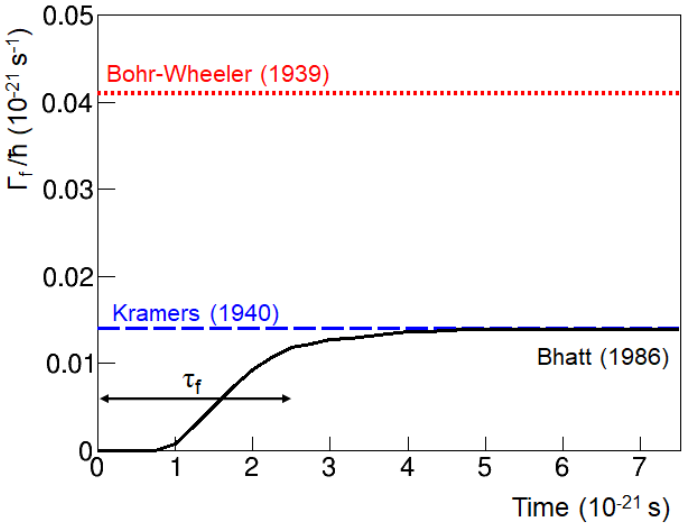

Figure 1.2: *Fission rate as a function of time. Red dotted line correspond to Bohr-Wheeler fission rate and blue dashed line represents Kramers fission rate. The solid line is obtained from [49], consisting in a numerical solution of the FPE for A=248, beta* $= 5 \cdot 10^{-21} s^{-1}$ *and T= 2 MeV.*

The transient time is closely related to the energy transfer rate between collective and intrinsic degrees of freedom. Its relation with the dissipation coefficient, β, can be written as [49]:

$$\tau_f = \begin{cases} \frac{1}{\beta} ln\left(\frac{10B_f}{T}\right) & \text{for } \beta < 2\omega_{gs}, \\ \frac{\beta}{2\omega_{gs}^2} ln\left(\frac{10B_f}{T}\right) & \text{for } \beta > 2\omega_{gs}. \end{cases} \tag{1.6}$$

where ω_{gs} is the harmonic oscillator frequency at ground state, B_f the fission barrier and T the nuclear temperature. There are two different regimes defined by β; one refers to an overdamped regime where the energy transfer

between degrees of freedom is fast ($\beta < 2\omega_{gs}$) while in the second one, the transference of energy is also fast but the time to reach the stationary regime is increased due to the damping of the motion of the collective degrees of freedom in the deformation space [49].

Recently, the work performed by Jurado and collaborators [50] pictured a more accurate description of the fission flow over the fission barrier from an analytical solution of the FPE. The obtained time-dependent fission decay width can be expressed as follows:

$$\Gamma_f(t) = K \cdot \Gamma_{BW} \cdot \frac{W_n(x = x_b; t, \beta)}{W_n(x = x_b; t \to \infty, \beta)} \tag{1.7}$$

The parameter $W_n(x = x_b; t, \beta)$ is the normalized amplitude of the probability distribution at the saddle-point deformation, x_b. In the case of a parabolic nuclear potential, this probability distribution presents the following gaussian form:

$$W_n(x = x_b; t, \beta) = \frac{1}{\sqrt{2\pi\sigma}} \cdot \exp\left(-\frac{x_b^2}{2\sigma^2}\right) \tag{1.8}$$

where σ accounts for a time dependent width, being also dependent on the nuclear temperature, the curvature of the potential at its ground state and the dissipation coefficient [51].

We will follow this result to calculate the fission decay probabilities in our model calculations. Other works, such as the performed by W. Ye and collaborators [52] used a numerical solution of the Langevin equations coupled to the statistical decay model to study fission dynamics [53]. The main inconvenient of this kind of theoretical approaches is the huge computing time needed. In this sense, the approximations based on the statistical model including a time factor to describe the dynamics provide rather accurate results and much less computing issues.

Saddle-to-scission dynamics

To precisely describe the dynamics of the fission process beyond the saddle point, one can follow the work done by Hofmann and Nix [54]. From the Kramers′ dynamical description of the fission process, an analytical solution of the average saddle-to-scission time, τ_{ss}, was found as:

$$\tau_{ss} = \left(\left[1 + \left(\frac{\beta_{ss}}{2\omega_0^{sad}}\right)^2\right]^{\frac{1}{2}} - \frac{\beta_{ss}}{2\omega_0^{sad}}\right)\tau_{ss}^0 \tag{1.9}$$

In this equation, the first term is identical to the Kramers factor in equation 1.4, with β_{ss} representing the dissipation parameter between the saddle and the scission point and being ω_0^{ss} the frequency of the inverted oscillator potential at the saddle point. The factor τ_{ss}^0 refers to the non-dissipative saddle to scission time, which is calculated using the analytical expression:

$$\tau_{ss}^0 = \frac{2}{\omega_0^{sad}} R\left(\left[\frac{\Delta V}{T_{sad}}\right]^{\frac{1}{2}}\right) \tag{1.10}$$

where *R(z)* is a function introduced and tabulated by Rosser [55]. T_{sad} describes the nuclear temperature at the saddle point, that can be expressed in terms of the excitation energy and the level density parameter, a, making use of the Fermi-gas model as:

$$T_{sad} = \sqrt{E/a} \tag{1.11}$$

ΔV represents the potential energy difference between the saddle and the scission points. The analytical expression of this parameter can be obtained approximating the potential shape around the saddle point to an inverted oscillator of frequency ω_0^{sad} as:

$$\Delta V = \frac{1}{2} M (\omega_0^{sad})^2 X^2 \tag{1.12}$$

Here, X represents the deformation coordinate of the fissioning system at the scission point with respect to that at the saddle point, defined as the elongation undergone by the system during its evolution. M is the mass inertia of the system. Considering the nucleus as an irrotational and incompressible flow, this term can be calculated as [56]:

$$M = \frac{A_{fiss}}{4}\left(1 + \frac{17}{15}\exp\left[-\frac{128}{51}\left(\frac{r}{R_0} - \frac{3}{4}\right)\right]\right) \tag{1.13}$$

Where A_{fiss} refers to the mass of the fissioning system and the ratio r/R_0 is related to the shape of the nucleus in terms of its quadrupole deformation at the saddle point β_q^{sad}:

$$\frac{r}{R_0} = 1 + \frac{2}{3}\beta_q^{sad} \tag{1.14}$$

To finish, the deformation coordinate of the system X can be obtained according to the difference of the deformation coordinates between the saddle

and the scission points, $X = X_{scs} - X_{sad}$. X_{sad} represents the increase of the nuclear radius from the ground state deformation to the saddle point and can be obtained in terms of β_q^{sad} [57] as:

$$X_{sad} = r_0 A_{fiss}^{1/3} \left(1 + \frac{2}{3}\beta_q^{sad}\right) \tag{1.15}$$

and X_{scs} is deduced on the basis of the distance between the two spheroids defining the incipient fission fragments at the scission point [58] according to the expression:

$$X_{scs} = r_0 A_1^{1/3} \left(1 + \frac{2}{3}\beta_1^{scs}\right) + r_0 A_2^{1/3} \left(1 + \frac{2}{3}\beta_2^{scs}\right) + d \tag{1.16}$$

where A_1 and A_2 are the fission fragment masses, β_1^{scs} and β_2^{scs} the corresponding quadrupole deformations at the scission point with d representing the tip distance between the two spheroids, whose value is between 2 and 3 fm [59].

1.3 Observables to investigate fission dynamics

1.3.1 Experimental signatures

The investigation of fission dynamics from an experimental point of view requires the determination of the fission times. This is, however, a really challenging task. Some techniques, based on crystal blocking [60] or on the electronic K-vacancy-lifetime [61], provide direct measurements of fission timescales. However, the sensitivity of these methods is limited to around $10^{-18}-10^{-19}$ s. Considering the typical fission timescales, we only have access to upper limits of the fission time distribution using these techniques [10].

Other approaches to probe fission timescales consist in measuring the number of light particles or γ rays emitted by the fissioning system before the scission point. The longer the time to reach the scission point, the larger the number of emitted particles or γ ray. Therefore, these observables can be used as fission clocks, accessing to the total fission time from the ground state configuration to the scission point. This led to huge progress in the understanding of fission dynamics. However, it is not possible to distinguish experimentally if these particles were emitted in the presaddle or in the postsaddle stage. Therefore, to obtain information about the timescales on

both stages and to study transient effects, one needs to make use of other observables sensitive to pre- and postsaddle fission dynamics and access to these times with the help of model calculations.

The optimal experimental conditions to study fission dynamics are achieved when the fissioning system presents high excitation energies, low angular momentum and small initial deformation [9]. Equations 1.6 and 1.9 allow to obtain the transient time and the saddle-to-scission time from the temperature at saddle point (directly related with the excitation energy) and the ground-to-saddle and saddle-to-scission dissipation parameters, respectively. The fission timescales can be inferred with the help of observables sensitive to dissipation and transient effects. In the next pages, we will introduce the most commonly used observables to investigate the dynamics of the fission process at high excitation energies, with the focus on those that will be later discussed in Chapter 3. We will distinguish between observables sensitive to the presaddle dynamics and those sensitive to the postsaddle dynamics, with the aim of constraining the dissipation parameter for both stages.

1.3.2 Presaddle observables

The investigation of presaddle observables will allow to characterize a stage governed by small deformations. The transient time is other important feature of this stage, so these observables also bring the possibility to access to its value. The two main observables used for describing the dynamical properties in this stage are explained below.

Total and partial fission cross sections

Fission cross sections are one of the most generally used observables to investigate the transient effects during the evolution of the fissioning system up to the saddle point. The description of the diffusion process across the barrier in terms of dissipation reduces the fission cross sections in comparison to the statistical model predictions [62, 30]. This is explained due to the transient time that the system needs to surpass the fission barrier. During this time delay, the probability of fission decreases, being other deexcitation channels, such as the emission of light particles, possible.

Thus, the fission cross section reveals as an interesting observable to study the transient effects in the fission process. An example can be found in the work of Jurado and collaborators [30], depicted on figure 1.3. Using a $^{238}U+CH_2$ fission reaction, the measured partial fission cross sections as

a function of the sum of the atomic numbers of the final fission fragments are displayed (black dots) and compared with different model calculations. Solid dashed line corresponds to the statistical Bohr and Wheeler model, described by equation 1.2, while other curves represent model calculations based on the time-dependent fission width expressed in equation 1.7. The calculations performed with a dissipation parameter of $\beta = 2 \cdot 10^{21} s^{-1}$ are able to reproduce the experimental data with accuracy. This result confirms the need of transient effects, as the statistical model overestimates the values of the partial fission cross sections, especially for light fissioning systems produced with higher excitation energies.

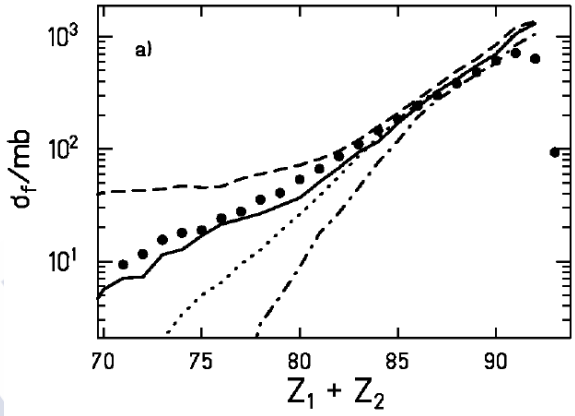

Figure 1.3: *Partial fission cross sections (black dots) compared with different model calculations [30]. The dashed line is obtained with the Bohr-Wheeler model. The solid, the dotted, and the dashed-dotted lines show calculations including dynamical effects using* $\beta = 2 \cdot 10^{21} s^{-1}$, $\beta = 0.5 \cdot 10^{21} s^{-1}$ *and* $\beta = 5 \cdot 10^{21} s^{-1}$, *respectively.*

Width of the atomic number distribution of the fission fragments

The temperature at the saddle point (T_{sad}) is another parameter that can be used to understand the fission dynamics since the modification of the fission probability during the transient time changes the excitation energy at the saddle point, hence the temperature (see equation 1.11).

This quantity can not be measured directly, making necessary to use other observables. In this case, the widths of the atomic number and mass distributions of the fission fragments are the most suitable observables to access to this parameter, which is related to the temperature at the saddle point as [63, 64]:

$$\sigma_Z^2 = \frac{Z_{fiss}^2 T_{sad}}{16(d^2V/d^2\nu)} \quad \text{and} \quad \sigma_A^2 = \frac{A_{fiss}^2 T_{sad}}{16(d^2V/d^2\nu)} \tag{1.17}$$

being $d^2V/d^2\nu$ the second derivative of the potential with respect the mass-asymmetry degree of freedom at the saddle point, represented by ν. Z_{fiss} and A_{fiss} are the atomic and mass numbers of the fissioning nucleus. Due to the neutron excess of the fragments formed beyond the saddle point, the evaporation of neutrons is favored over the proton emission [65], so the width of the atomic number distribution of the fission fragments results in a more reliable observable to constrain the temperature at the saddle point. Based on these ideas, the first work where this observable was proposed to study fission dynamics was carried out by Benlliure and collaborators [37]. Then, other works have also used this observable to constrain model calculations [30, 66]. In particular, Schmitt and collaborators [67, 31] investigated the transient effects using peripheral relativistic heavy ion collisions and the width of the distribution in atomic number of the final fission fragments. Model calculations for different nuclei confirm that transient effects are needed to reproduce the measurements, as seen in figure 1.4.

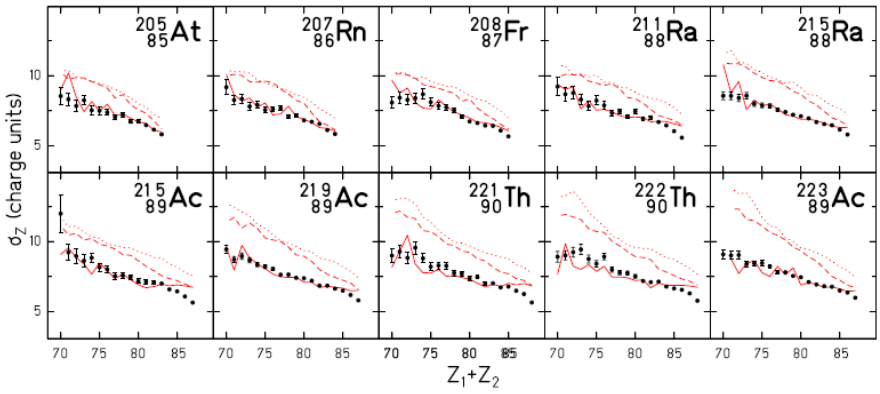

Figure 1.4: *Standard deviation of the charge distribution of the fission fragments as a function of Z_1 + Z_2. Experimental data (black dots) for different nuclei is compared with statistical (dotted lines) and Kramers (dashed lines) calculations as well as time-dependent approximation (full lines) type calculations [51]. In the two latter cases, $\beta = 4.5 \cdot 10^{21} s^{-1}$. Figure taken from [67].*

Dashed and dotted lines represent calculations performed using the Kramers and the Bohr-Wheeler approaches, overestimating the experimental data. Calculations including transient effects in fission with a dissipation

parameter of $\beta = 4.5 \cdot 10^{21} s^{-1}$ describe accurately the experimental data. In this case, the dissipation parameter is slightly higher than the one obtained by B. Jurado. This discrepancy can be explained due to the fact that the initial deformation of the nuclei under study was not taken into account in the calculations performed by Jurado and collaborators, something that was proved to be relevant in [68].

1.3.3 Postsaddle observables

In the second stage of the fission process, the fissioning system evolves from the saddle until the scission point increasing its deformation. Using observables sensitive to the evolution of the initial nuclei from the ground state configuration to the scission point, the postsaddle dynamical effects can be studied. In this work, we will focus on the observable proposed by Rodriguez et al [69], the average neutron excess of the final fission fragments.

Average neutron excess

Defined as the average neutron number over the atomic number of the final fission fragments $<N/Z>$, this observable is sensitive to presaddle and postsaddle dynamics, as the final neutron number of the fragments depends on the neutron evaporation along the complete fission path and even from the two nascent fragments. Therefore, the final neutron excess of each fragment will be affected on the initial excitation energy gained by the fissioning system. This observable will be useful to obtain information on the saddle-to-scission time, parametrized as a function of the postsaddle dissipation parameter (1.9). The larger this time is, the more neutrons can be emitted during the saddle-to-scission stage.

The work by Rodriguez and collaborators uses ^{208}Pb+p spallation-induced fission reactions to study the dynamics of fission at high excitation energy and low angular momentum and initial deformation. These authors were able to constrain the value of the presaddle dissipation parameter, measuring fission cross sections and the width of the fission fragments atomic number distribution (explained in section 1.3.2), and also the postsaddle dissipation parameter with the average neutron excess of the fission fragment isotopic distributions. In figure 1.5, the average neutron excess is depicted as a function of $Z_1 + Z_2$ and compared with model calculations. First conclusion is that predictions obtained using a statistical time in the transit from saddle-to-scission (dashed double-dotted line) overestimate the neutron excess of the fission fragments for lighter systems, making relevant the introduction of dissipation. In this work, the presaddle

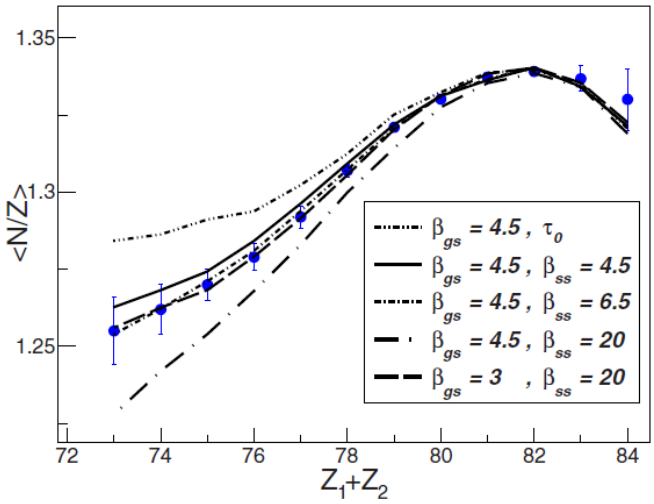

Figure 1.5: *Average neutron excess over the atomic number of the final fission fragments as a function of their total charge compared to model calculations using different assumptions on the magnitude of the dissipation parameter from ground to saddle and from saddle to scission. τ_0 corresponds to the saddle-to-scission statistical time. Figure taken from [70].*

dissipation parameter was $\beta_{gs} = 4.5 \cdot 10^{21} s^{-1}$. Thus, the calculation that better describes the measurements corresponds to a postsaddle dissipation parameter of $\beta_{ss} = 6.5 \cdot 10^{21} s^{-1}$. The conclusion is that there is not a sizeable dependence of the dissipation parameter on deformation.

1.4 Proposed investigation

1.4.1 Dissipative effects in fission reactions induced by relativistic ^{236}U projectiles

The main objective of this work is to contribute to the study of fission dynamics giving answer to several questions that have been under discussion in the recent years. The description of the pre- and postsaddle dissipation parameter has been a widely investigated topic, obtaining different results. The most important ones are summarized in figure 1.6. A correct determination of this parameter will allow to access to the typical fission times and to study its dependence with deformation [10, 71]. Using fusion-fission reactions, some works have been able to constrain the values of β for small and large deformations, using as observables the

pre- and post-scission multiplicities of neutrons or γ rays [72, 73, 74, 75]. The most significant result of those works is an apparent dependence of the dissipation parameter required to describe the fission dynamics with deformation. The dissipation parameter at small deformations (red dots) is between $\beta_{gs} = 2 - 6 \cdot 10^{21} s^{-1}$ while at large deformations (blue dots) is larger than $\beta_{gs} = 20 \cdot 10^{21} s^{-1}$ in most cases.

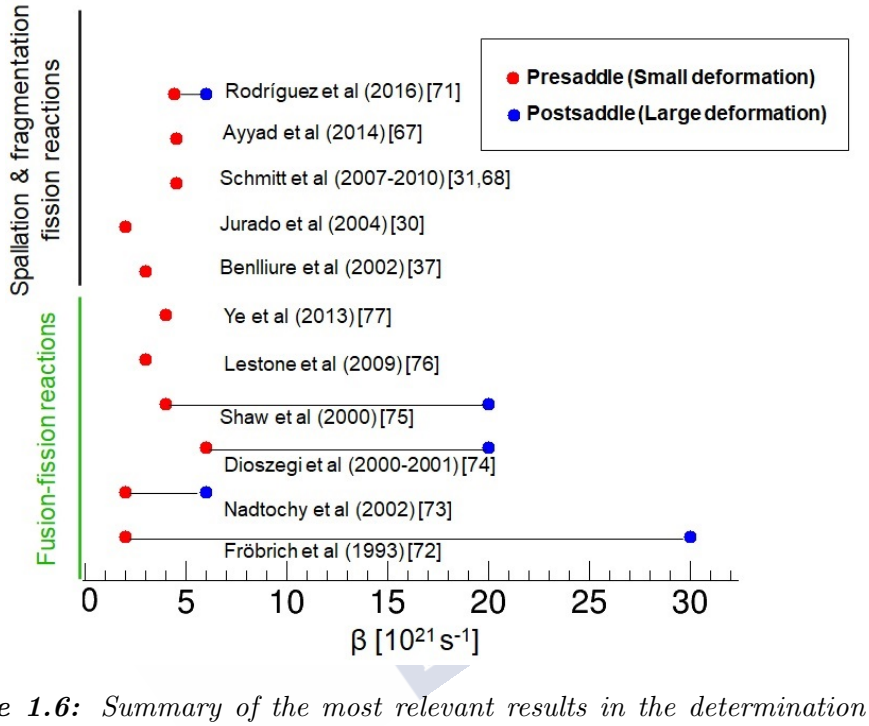

Figure 1.6: *Summary of the most relevant results in the determination of the dissipative coefficient from spallation-, fragmentation- and fusion-induced fission reactions. Red and blue dots correspond to pre- and postsaddle dissipation parameters, respectively.*

Other works, mainly measuring fission probabilities or charge distributions were able to constrain the value of the dissipation parameter only in the presaddle regime, using both fusion-fission [76, 77] and spallation- or fragmentation-induced fission reactions [37, 30, 67, 31, 66], establishing it around $\beta_{gs} = 4.5 \cdot 10^{21} s^{-1}$. Recently, the improvements in the experimental technique allowed for the identification of both fission fragments in atomic and mass number, giving access to observables sensitive to both stages using spallation-induced fission reactions. The value of the postsaddle dissipation parameter was obtained for the first time in this kind of reactions measuring the average neutron excess of the fission fragments [70]. The value of the dissipation parameter between saddle and scission that best described the

data was $\beta_{ss} = 6.5 \cdot 10^{21} s^{-1}$, very similar to the presaddle dissipation parameter. This result seems to contradict the previously obtained using fusion-fission reactions. The main difference between both types of induced fission is the large angular momentum gained by the compound nucleus in fusion-fission reactions, that could affect the conclusions drawn for such experiments. In this sense, fragmentation or spallation fission reactions seem to be better suited to perform this kind of studies.

In this PhD dissertation, we will make use of ^{236}U fragmentation-induced fission reactions in thick uranium and aluminum targets at relativistic energies (around 720A MeV) in inverse kinematics. Thanks to the powerful SOFIA setup, both fission fragments can be identified in atomic and mass number and observables sensitives to pre- and postsaddle configurations can be obtained. This will allow us to study the dynamics of the fission process at high excitation energies and to constrain the dissipation parameter at both fission stages.

The value of the β presaddle parameter is rather well established. We aim to confirm previous findings but in particular to investigate other parameter affecting the description of the fission process as the angular momentum or level densities. We will make use of different model calculations using the intra-nuclear cascade model INCL [78, 79] and the abrasion model ABRABLA [80].

Regarding the saddle-to-scission configuration, one of the driving ideas for this work is to complete the investigation of Rodriguez and collaborators [70] using a different nucleus, ^{236}U, to constrain the value of the postsaddle dissipation parameter and study its dependence with deformation. The range of deformations achieved in ^{236}U fragmentation-induced fission reactions is larger than in ^{208}Pb+p spallation-induced fission reactions. In figure 1.7, the deformation coordinates covered in both reactions at the saddle and the at scission point, defined by equations 1.15 and 1.16, are shown as a function of the sum of the atomic number of the fission fragments. Left panel shows the deformation coordinate at saddle for fragments produced in ^{208}Pb+p reaction (dashed black line) and for ^{236}U+Al (full black line). Fragments from ^{236}U reactions present larger deformation values. Right panel shows the same at scission point. In this case, the deformation coordinate depends basically on the mass number of the fission fragments at scission. For the same $Z_1 + Z_2$ value, the excitation energy is larger in ^{236}U due to the fact that more protons have been removed. This induces more neutron evaporation, presenting shorter deformation coordinates.

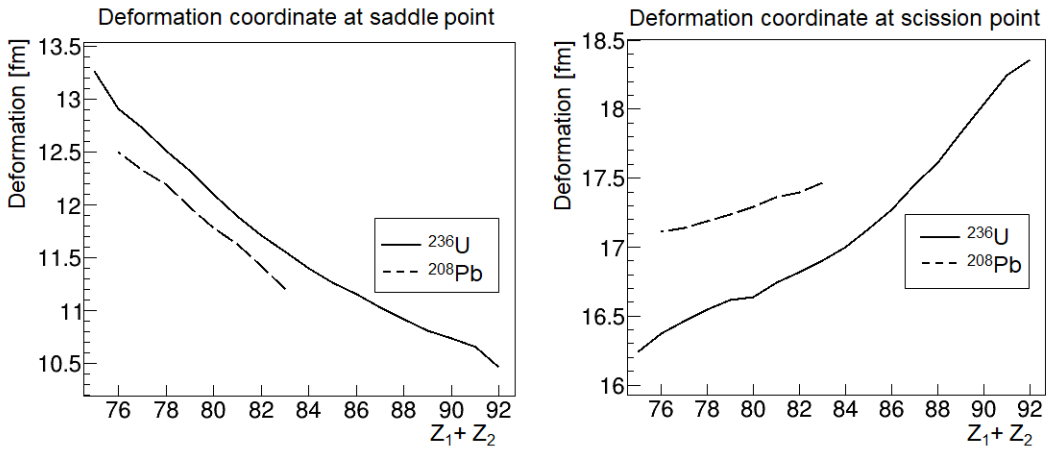

Figure 1.7: *Deformation coordinate as a function of Z_1 + Z_2 at saddle point (left) and at scission point (right).*

1.4.2 Future options to investigate fission dynamics in inverse kinematics

In the last section of this thesis, we propose to improve the experimental technique to overcome one of the main limitations of the present investigations, the impossibility to measure or constrain the initial excitation energy of the fissioning nucleus. In nuclear-induced fission, this quantity is evaluated using model calculations, while in coulex-induced fission, the excitation energy gained by the fissioning system is obtained from the range covered by the giant-dipole resonance (GDR) excitation.

We aim to go a step further using *(p,2p)* reactions to induce fission. This reaction mechanism will allow to determine the excitation energy gained by the *(A-1, Z-1)* remnant undergoing fission from the kinematics of the two protons emitted. Measuring their kinetic energies, as well as their trajectories, one is able to reconstruct their four-momentum and extract the excitation energy of the process using the missing mass spectroscopy. To carry out these measurements, we propose to combine the SOFIA setup with the R^3B (Reactions with Relativistic Radioactive Beams) detectors. These detectors, consisting of the CALIFA proton calorimeter and a silicon tracker surrounding the liquid hydrogen target region, will measure the two *(p,2p)* outgoing protons. In order to explore the possible implementation of a *(p,2p)*-induced fission experiment, realistic simulations will be presented and discussed in Chapter 4.

USC
UNIVERSIDADE
DE SANTIAGO
DE COMPOSTELA

Chapter 2

Experimental Methodology and Data Analysis

In this chapter we provide a detailed description of the experimental methodology used in this work. We will explain the experimental setup specially designed for the investigation of fission in inverse kinematics, which allowed us to separate fission from other reaction channels. This setup permits the identification in atomic and mass number of the secondary beams coming from the FRS to Cave C, which impinge on an active target located at the entrance of Cave C. We will explain carefully the procedure to identify and select the fission events in order to reconstruct both fission fragments in atomic and mass number. Finally, we will describe the corrections and reconstruction method utilized to determine the isotopic distribution of the fission fragments.

2.1 Introduction

Despite the fission process has been discovered more than 80 years ago, the study and complete characterization in charge and mass of both fission fragments is complicated. The information on full isotopic distributions has been scarce until a few years ago, where both fission fragments were identified in charge and mass simultaneously in the experiments performed by the SOFIA (Studies On FIssion using Aladin) collaboration at GSI. Within the framework of this collaboration, two experimental campaigns have been realized to the date. The first one was conducted in August 2012 [27, 28] measuring a wide range of fissioning systems (^{234}U, ^{235}U, ^{238}U, ^{237}Np and ^{238}Np). Two years later, in October 2014, new measurements were performed with the main goal of measuring ^{236}U. In this second experiment, named

SOFIA-2 [81], the experimental setup was slightly changed and upgraded, increasing its detection efficiency. In this work, our study will be focused on the ^{236}U fissioning system, measured also in the previous experiment but with limited statistics. It is a very interesting nucleus to study, lying its importance, among other reasons, on the fact that fission of ^{236}U is the analog of the ^{235}U(n,f), the main reaction in the majority of nuclear reactors [82].

For this investigation, in order to avoid inherent limitations of direct kinematics measurements, the most useful experimental approach is the use of the inverse kinematics technique, which permits to accelerate heavy ions into relativistic energies [24]. It is used for producing secondary beams that will eventually induce fission. This technique allows for the access to short lived unstable nuclei and the production of high velocity fission fragments emitted in forward direction, making easier their detection. The combination of this technique with the SOFIA innovative experimental setup enabled the complete identification of fission fragments (mass and nuclear charge) for the first time, representing a real breakthrough in the study of fission process and permitting to measure isotopic yields with high precision [69].

Moreover, the use of an active target [83] made of four layers, with different atomic numbers, allows for the investigation of the two reaction different mechanisms to induce fission: electromagnetic interaction (Coulex) and nuclear fragmentation [84]. Coulex fission is produced in high Z targets, interacting the projectile with the coulomb field of the target with an interaction impact parameter relatively high. On the other hand, fission induced by nuclear fragmentation is a much less peripheral process, produced when fission is induced in low Z targets. The result is an excitation energy of about one order of magnitude higher in fission induced by nuclear fragmentation than in coulex-induced fission.

2.2 The GSI facility

2.2.1 Overview

To obtain these highly energetic beams, the experiment was carried out at the GSI facility. GSI is the unique worldwide facility capable of providing a ^{238}U primary beam at an energy up to 1 GeV per nucleon, needed to produce secondary radioactive beams at high energies. A display of the facility is shown in Figure 2.1.

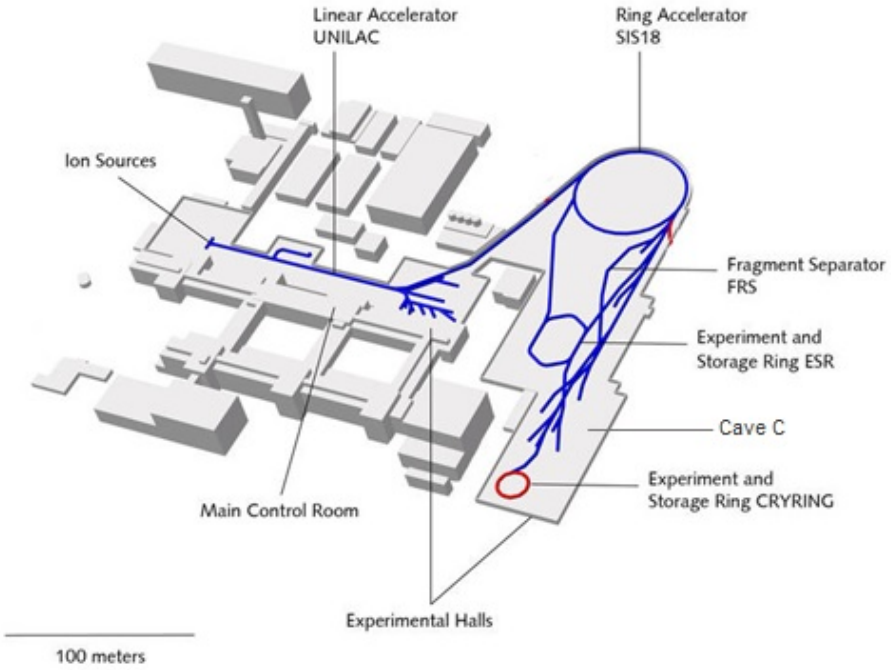

Figure 2.1: *Overview of the accelerators and experimental areas at the GSI facility, adapted from [85].*

To reach such high energies, ions have to go through different acceleration stages. The starting point of the GSI accelerator facility are the ion sources [86]. It is in these devices where the ions are generated by stripping electrons off the shell of the atoms. There are different types of ion sources, depending on the ions produced, which range from hydrogen (Z=1) to uranium (Z=92). Once produced, ions are injected into the UNILAC (UNIversal Linear ACcelerator) [87], where they experience a first acceleration stage across its 120 meters of length, being able to reach velocities up to 20 percent of the speed of light. After that, they continue their way through the ring accelerator SIS18 [88], a synchrotron with a circumference of 218 meters that can boost ions velocity up to 90 percent of the velocity of light. After this second acceleration phase, our desired beam of ^{238}U at 1A GeV is generated. Then, the collision with a beryllium target placed right before the FRagment Separator (FRS) generates a broad range of nuclei in a fragmentation reaction. The FRS is a recoil spectrometer which allows to select among the secondary ions created, those of interest. Tuning the dipoles accordingly, only a few ions reach the last focal plane and enter in the Cave C, at Experimental Hall II, where SOFIA setup is placed. Finally, thanks to the presence in the Cave C of ALADIN (A Large Acceptance DIpole

magNet) [89] and a series of detectors developed by the SOFIA group, the identification of both fission fragments in atomic and mass number can be done with high accuracy.

2.2.2 The FRS

The FRS is a high resolution achromatic spectrometer that consists of several identical sections, each equipped with a 30 degree dipole magnet, a magnetic quadrupole triplet and a doublet, being able to analyze heavy-ion beams with magnetic rigidity from 5 to 18 Tm [23, 90]. Magnetic hexapoles placed directly in front of and behind each dipole correct second order image aberrations. Their angular acceptance results to be 20π mm mrad in the horizontal coordinate and 40π mm mrad in the vertical coordinate, with a momentum acceptance of $\Delta p/p=2\%$. Considering a beam spot size at the target of around 2-3 mm, the dispersion of 6.8 cm/% in the central focal plane allows a magnetic rigidity resolving power of 1600. On its original configuration, FRS has four sections (S1, S2, S3,S4), with a length of flight of around 35 meters. Depending on the aim of the experiment, there are four more sections that can be used, as shown in Figure 2.2, going up to S8 for the current experiment. The dispersion at the end of this plane is 11.0 cm/%.

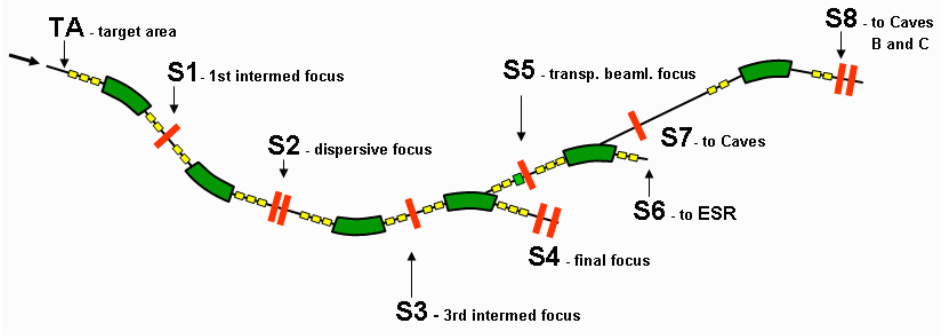

Figure 2.2: *Scheme of the Fragment Separator (FRS) with all its available sections. Each section has a dipole (green) and different quadrupoles (yellow). Hexapoles are shown in red. Picture obtained from [91].*

The FRS was designed to provide isotopically pure secondary beams of all elements up to Z=92 in the energy range of 100-2000A MeV. All the above-mentioned characteristic allows to separate the nuclei produced in fragmentation reactions according to atomic and mass number using the

known as Bρ-ΔE-Bρ analysis method, consisting of two steps: a first mass over charge ratio selection based on magnetic rigidity analysis and another selection based on the ions' energy loss in a dedicated material (degrader). Finally, just ions with a very similar mass and atomic number as the interested nucleus arrive at the end of the facility. More information will be given in section 2.3.

2.2.3 Fission Experimental Setup

This novel setup gives the chance to select the fissioning system among those reaching the Cave C after passing the FRS and induce fission, detecting the fission fragments produced. To do this above-mentioned identifications, the use of the ΔE-Bρ-ToF technique permits to unambiguously identify both the fissioning nuclei and the fission fragments.

Energy losses are directly measured in two ionization chambers, a Triple MUSIC for secondary beam and a Twin MUSIC [92] for fission fragments.

The mass number can be computed with the use of a magnetic dipole. When ions traverse the magnet, they are deflected according to their magnetic rigidity (Bρ). Thus, the mass number can be obtained using the following equation:

$$B\rho = \frac{p}{Q} = \frac{A}{q \times e} u\beta\gamma c \tag{2.1}$$

being B the magnet magnetic field [T], ρ the ion's curvature radius [m], p the momentum of the ion [kg m/s], q the atomic charge [C], A the mass number, e the elementary charge [C], u the atomic mass [kg], β the ratio of the ion velocity to the speed of light, γ the Lorentz Factor($\gamma = 1/\sqrt{1-\beta^2}$) and c the speed of light [m/s].

Magnetic rigidity can be calculated using the tracking detectors. For the secondary beam, position can be tracked with S2 scintillator and a MWPC (Multi-Wire Proportional Counter) [93] located at the entrance of Cave C and for fission fragments one can extract the trajectory using the angle in the Twin MUSIC and position measurements in the MWPCs. Combining this information accordingly, the magnetic rigidity is obtained.

$\beta\gamma$ factor is extracted from ToF measurements and the reconstruction of the path length. For secondary beam, two scintillator detectors [94], with the S2 scintillator acting as start and the Cave C scintillator as a stop, secondary beam ToF is measured and the velocity can be extracted together with the FRS path length of 135 m. For fission fragments, the Cave C scintillator acts

as a start and the stop signal is given by a ToF Wall [95] placed at the end of the fission fragments flight path as shown in figure 2.3.

So knowing the atomic number, the magnetic rigidity and the $\beta\gamma$ factor, the mass number can be deduced from equation 2.1. As the observables measured to fully identify both secondary beam and fission fragments are the energy loss (ΔE), the magnetic rigidity Bρ and the Time-of-Flight (ToF), this is the reason why this identification method is called ΔE-Bρ-ToF technique. Further details of the detectors and the analysis will be given in the following sections.

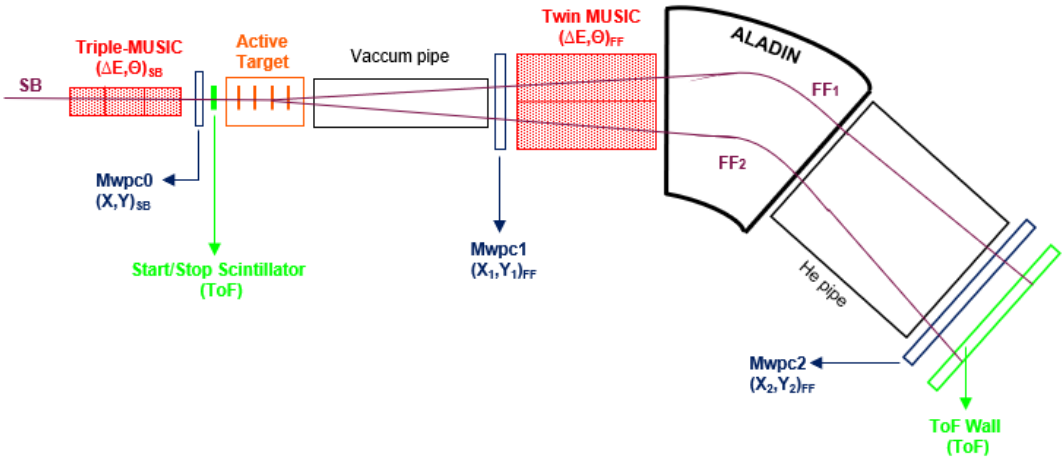

Figure 2.3: *Scheme of the experimental setup. Secondary beam fissioning nuclide is selected before the active target, where fission takes place. Fission fragments are also identified using the set of detectors after the target and the ALADIN magnet.*

2.3 Fragmentation of the primary beam

The ^{236}U secondary beam is produced after a fragmentation reaction of ^{238}U primary beam ions in a target of 1036 mg/cm^2 beryllium [96]. A niobium foil with a thickness of 223 mg/cm^2 acts as a stripper [97], minimizing charge states contamination. Among all the ions produced in the primary fragmentation reaction, FRS makes a two steps efficient selection, just keeping those of interest. The specific FRS configuration used for the experiment is displayed in figure 2.4.

First, a pure magnetic rigidity analysis is made between S0 and S2, selecting ions with a similar mass over charge ratio, since these reaction

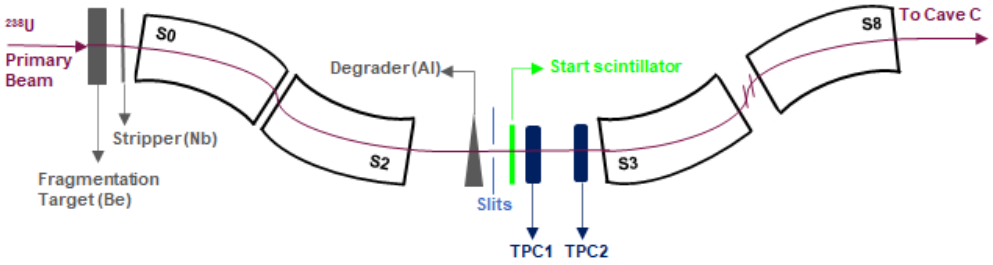

Figure 2.4: *FRS schematic configuration used to carry the secondary beam to the experimental room.*

products have approximately the same velocity. So, at this point an A/Z selection is performed, considering fully-ionized fragments. To achieve a full isotopic separation, a second independent selection needs to be done, from S2 to S8, which consists in a Z selection process. A thick layer of matter, in this case aluminum with a mass thickness of 2220 mg/cm^2, was placed at S2, acting as an energy degrader. Hence, the fragments slow down and their energy losses are analyzed in the last two dipole stages, performing a selection in atomic number. This combined Bρ-ΔE-Bρ analysis allows a complete identification in atomic and mass number. The selection process can be visualized in figure 2.5.

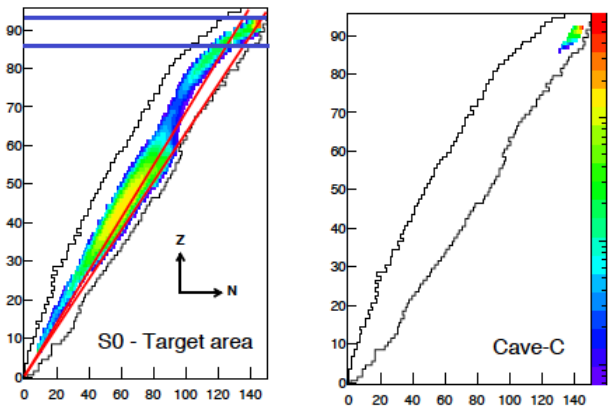

Figure 2.5: *FRS selection process. Left: Ions produced after fragmentation reaction. Red lines include the Bρ selection done in first two dipoles and blue the Z selection in last stage. Right: Selected isotopes reaching the Cave C. Image adapted from [98].*

2.4 Secondary beam Identification

The first part of the experimental setup (figure 2.3) allows for the identification, on an event-by-event basis, of the fissioning nucleus we are interested in. In this section, detailed information of each detector will be given, explaining the observables measured as well as the calibrations required to extract them and to unambiguously select the projectile nuclei of ^{236}U.

2.4.1 Triple MUSIC

Triple MUSIC specifications

The atomic number of the secondary beam can be extracted from the energy loss measured in the Triple MUSIC (MUlti-Sampling Ionization Chamber). The detector is composed of three symmetric and independent ionization sections, consisting of a cathode and a segmented anode plane inside a gas volume. These sections are separated by stripping niobium foils, as displayed in figure 2.6, in order to minimize charge states contamination. However, as charge states are anyhow present, each section performs an independent energy loss measurement and their combination allows to reject the charge states. Technical information of the detector, regarding sizes, voltages and gas filling for the experiment is listed in table 2.1.

Gas Mixture	30% CH_4; 15% CF_4; 15% He; 40% Ar
Pressure	1.02 bar
Voltage of anodes	+650 V
Voltage of cathode plane	-2600 V
Distance cathode-anode	83 mm
External volume	200 x 200 x 600 mm^3
Strippers	80 μm Niobium

Table 2.1: *Triple MUSIC technical information. The composition of the gas mixture filling the detector is specific for this experiment.*

Besides, taking another look at Figure 2.6, we observe that each of the three sections presents two screening rectangular anodes on both ends, to preserve the homogeneity of the electric field inside the chamber, and three pairs of trapezoidal shaped-like anodes in the middle. From each trapezoidal anode, an energy loss and drift time measurement is performed.

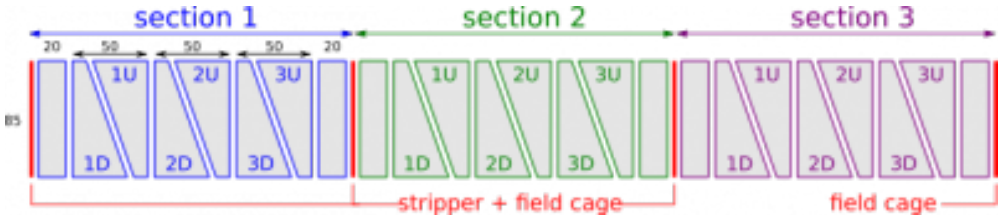

Figure 2.6: *Triple MUSIC side view.*

From the energy loss measurements, one can also extract the Y position of the ion along the trajectory. Since the energy loss depends on the amount of matter traversed and as the width of the anodes is gradually changed along the Y-axis, the difference of the energy loss between two complementary anodes on a pair directly permits to obtain the ion's vertical position with an uncertainty of around 1 mm.

In addition, the ion's X-position and horizontal angle can be obtained from drift time measurements of each anode. Knowing the drift velocity, the distance between the ionization point and the anode plane can be extracted on an event-by-event basis. Finally, knowing the distance between anodes, a raw value of horizontal angle can be computed.

Determination of the secondary beam atomic number

The energy loss measurements carried out in the Triple MUSIC allows for the identification of the secondary beam atomic number. For this purpose, the detector needs to be calibrated. Also, corrections of possible dependencies with different parameters are performed in order to improve the resolution. In the following, we wil describe the most relevant corrections. More detailed information can be found in reference [99].

1. It is necessary to align the gain of each anode in order to be able to treat each anode measurement as an absolute value that can be directly compared between them. The alignment basically consists in removing the dependence of the energy loss with the Y position. Consequently, when the gains of two anodes in a pair are aligned, the sum of weighted energy losses in a pair should not vary with the Y position of the ion.

2. Once these gains are aligned inside all pair of anodes, we need to align all nine pair of anodes gains. This can be simply done by choosing one of the anodes as reference (in our case, the anode 4) and by calculating

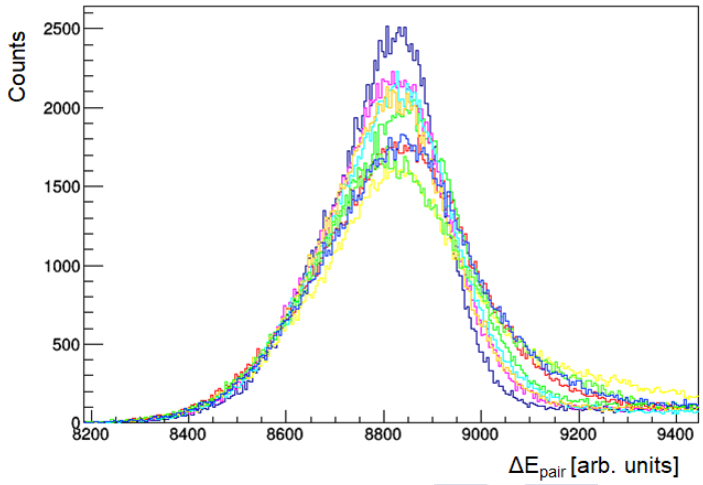

Figure 2.7: *Aligned energy losses for all Triple MUSIC pair of anodes. Each color represents a different pair.*

its energy loss as the sum of the two anode signals of this pair. Then, calculating the centroid of the distribution, a correction factor is applied for the other pair of anodes, consisting of just a simple ratio between its centroid value and the reference centroid value. After these two corrections, the energy losses are aligned for all anodes as shown in figure 2.7.

3. Next step is about improving the energy loss resolution per section in order to separate different charge and charge states. For each section, the total energy loss is considered as the sum of the energy loss measured on each pair. It has to be taken into account that the relative energy loss value between different charges is more important than the absolute value of the energy loss. The energy loss measured on each section depends on other parameters, such as:

   (a) The anode drift time.

   (b) The ion velocity, whose calculation will be explained in subsection 2.4.2.

   (c) The horizontal angle, that was obtained subtracting the drift time of two different anodes. In order to be more precise, we used the drift time values of anodes 2 and 14. The result is an angular value in arbitrary units.

Correcting these three dependencies is enough to improve the energy loss resolution and eventually identify the secondary beam in atomic number.

4. At this point, the three different and independent energy loss measurements for each section are available. Combining this information, the atomic number identification is completed. For this, two different plots are shown in figure 2.8. The red circle indicates the energy loss of ions with an atomic number Z=92. Events that are simultaneously inside these two gates correspond to Z=92 fully stripped events.

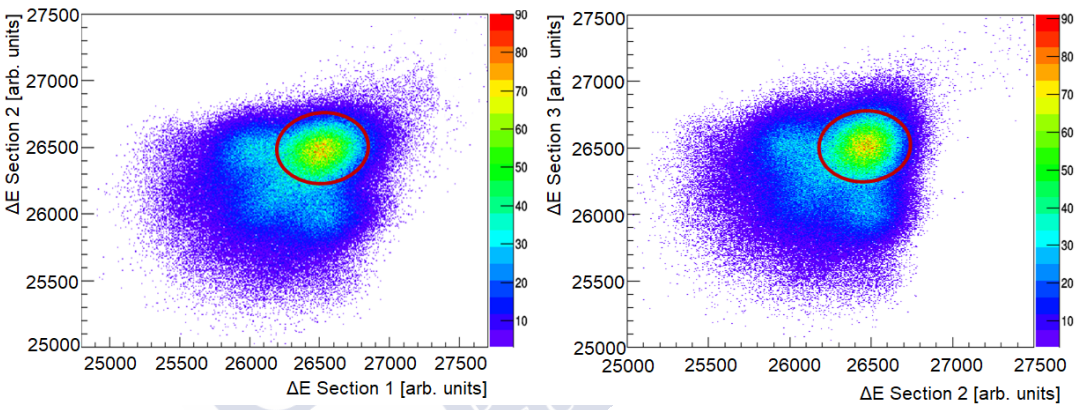

Figure 2.8: *Comparison of the ΔE for sections 1 and 2 (left) and 2 and 3 (right). Events simultaneously inside the two red circles correspond to Z=92 fully stripped ions.*

2.4.2 Scintillators

SOFIA Scintillators specifications

For this experiment, two scintillators were used to carry out time-of-flight (ToF) and position measurements with a separation in flight path of around 135 meters between them. The first scintillator was placed in the middle of the FRS focal plane, acting as a start for the ToF signal and also as a secondary beam position tracker. The second is located in the Cave C, before the Active target, working as a stop/start detector. For the secondary beam, it gives the ToF stop signal and for fission fragment the corresponding start signal. It also allows for position tracking, but as a MWPC is placed right after it, position is extracted from MWPC measurements (see section 2.4.3).

Figure 2.9 shows the S2 scintillator geometry. The Cave C scintillator has a similar structure, but with different dimensions and electronics, as detailed in table 2.2

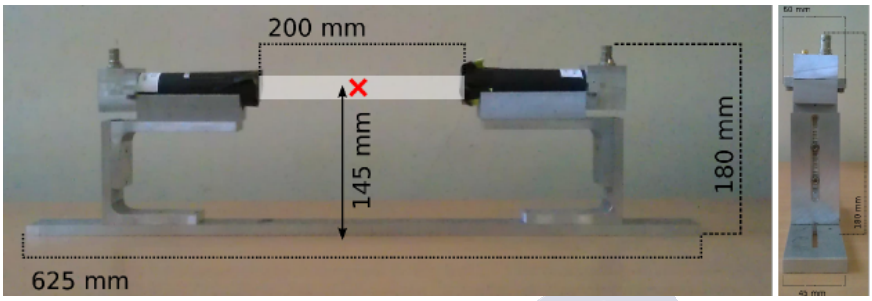

Figure 2.9: *S2 Scintillator front and side view. Two PMTs are connected on each side.*

The detectors are composed of two photomultipliers (PMTs) and a plastic scintillator in the middle. After the ionization produced in the scintillator material, visible light photons are created. These electrons fly through the photomultipliers tubes inducing via photoelectric effect a number of electrons [100], that are multiplied and accelerated by the internal electric field resulting in a detectable current pulse. The PMTs are stuck to both ends of the plastic using optical grease. The idea of using two PMTs is to cancel the effect of the ion position in the time measurements.

	START S2	STOP/START CC
Plastic Scintillator	EJ228, not quenched	EJ232, quenched
Plastic dimensions	200 x 50 x 1 mm^3	50 x 32 x 1 mm^3
PMTs Tubes	Hamamatsu 10508	Hamamatsu 6533

Table 2.2: *Technical information of the scintillator detectors used in the experiment.*

Secondary beam velocity calculation

The time signals on each scintillator are directly obtained as the mean value of both PMT time signals. Then, the raw time-of-flight is obtained by subtracting the S2 time signals to the time signals of the scintillator located at Cave C. It also has to be taken in account that S2 scintillator (S2) and

Cave C scintillator (CC) have different clock signals. They are synchronized using a common time signal, so the raw ToF is obtained as:

$$ToF_{raw} = (ToF_{CC} - Common_{CC}) - (ToF_{S2} - Common_{S2}) \tag{2.2}$$

To obtain the velocity of the secondary beams, this time-of-flight value needs to be previously calibrated. The calibration is achieved with four different runs of ^{238}U primary beam going directly to Cave C. On each run, different materials have been inserted along the beam line, so the primary beam suffers different energy losses and, subsequently, has different velocities, allowing for a linear calibration of the time-of-flight. Information about these runs is indicated in table 2.3.

Run	Target [mg/cm^2]	Stripper [mg/cm^2]	Degrader [mg/cm^2]	Velocity [cm/ns]
1	No target	No stripper	No degrader	26.24
2	No target	No stripper	Al, 2200	25.48
3	Be,1036	Nb, 223	Al, 2200	24.95
4	Be,1036	Nb, 223	Al, 3200	24.53

Table 2.3: *Information of the velocity calibration runs. The velocity of the primary beam was obtained with LISE++.*

To perform this calibration, the length of the flight (LoF) path is computed as:

$$LoF = v \times (ToF_{raw} - \Delta ToF) \tag{2.3}$$

leading to:

$$ToF_{raw} = LoF \times \frac{1}{v} + \Delta ToF \tag{2.4}$$

Using LISE ++ [101], primary beam velocity for each configuration can be obtained. Measuring the raw time-of-flight value, one can obtain the LoF and the ToF offset parameters and then use this linear calibration to obtain, event by event, the velocity of the secondary beam. The average velocity value of the secondary beam results to be 24.72 cm/ns leading to a secondary beam total kinetic energy of around 720A MeV.

Secondary beam S2 position measurement

To determine the mass number of the secondary beam, we need to measure its position at the intermediate focal plane (S2) of the FRS. The secondary beam position can be obtained using the scintillator placed at S2. From the two PMTs signals, the ion impact position can be deduced through the time difference between their signals. This arises a raw position measurement, in units of ns, that just shows how centered or displaced the secondary beam is.

To calibrate the position given by the scintillator from time units to position units, a pair of Time Projection Chambers (TPCs) [102] were placed in the FRS downstream of the START detector. For this purpose, three position calibration runs were executed. Adjusting the center position of the opening slits (see figure 2.4) ions impinge on different places on the scintillator. Combining this measurement with the ones performed by the TPCs, the position is extrapolated from linear correlation, obtaining an absolute position calibration of the secondary beam in millimeters.

2.4.3 MWPC0

SOFIA MWPC specifications

For position measurements, three Multi Wire Proportional Counters (MWPC) were used in the experiment. They essentially consist of a set of thin, parallel and equally spaced anode wires, symmetrically sandwiched between two cathode planes, creating an electric field inside a certain gas mixture (figure 2.10).

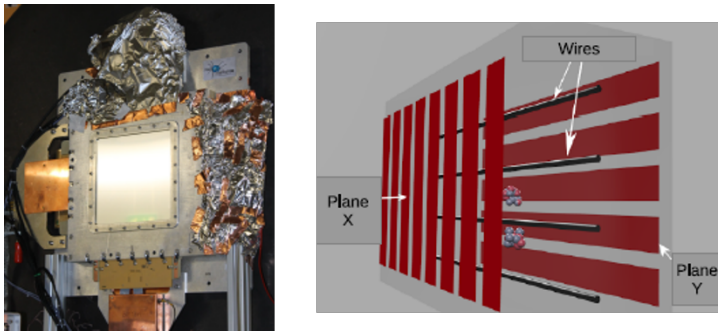

Figure 2.10: *Left: Picture of the MWPC0. Right: Schematic view. Image lend from [29]*

For secondary beam identification, one small MWPC was placed at Cave C before the active target, labeled as MWPC0. The segmentation of the cathodes in strips will allow for X (horizontal) and Y(vertical) position measurements. The resolution is significantly better for the horizontal position, which is the coordinate that directly affects to the calculation of the secondary beam mass number. Technical information of this detector can be found on table 2.4.

Gas Mixture	80% Ar; 20% CO_2
Surrounding windows	14 μm Mylar
Wire pitch	2.5 mm
Diameter of wires	25 μm
Width of X strips	3.125 mm
Width of Y strips	5 mm
Dimensions	200 x 200 mm^2
Number of strips	64 (X); 40(Y)

Table 2.4: *MWPC0 technical information*

Secondary beam position measurement at Cave C

To determine the secondary beam position at Cave C, the charge deposition on each strip of the MWPC0 is collected on an event-by-event basis. The position of the ions at the MWPC is defined by the centroid of their charge distribution, obtained by fitting the charge deposited in the pads around the ion passage position. This fit has to be carried out using a centroid-finding reconstruction algorithm. In this work, we made use of the secant squared method function (SECHS) explained in [103]. Thus, the position of the secondary beam at the entrance of Cave C can be extracted.

2.4.4 Secondary beam mass over charge ratio

Using the information extracted from the detectors, namely the atomic number from TriMUSIC, the velocity from scintillators and the beam positions from S2 scintillator and MWPC0, the secondary beam can be fully identified. From equation 2.1, knowing the values of the corresponding constants and considering a fully stripped ion, one can write:

$$\frac{A}{q} = \frac{B\rho_{S2->CC}}{3.107 \times \beta\gamma} \tag{2.5}$$

The $\beta\gamma$ parameter is directly obtained from the velocity. $B\rho_{S2->CC}$ refers to the magnetic rigidity of the secondary beam from S2 to Cave C, calculated as follows:

$$B\rho_{S2->CC} = (B\rho_{S2->CC})_0 \times \left(1 + \frac{\Delta X_{S2}}{D_{S0->S2}} + \frac{\Delta X_{CC}}{D_{S2->CC}}\right) \tag{2.6}$$

where $(B\rho_{S2->CC})_0$ is the magnetic rigidity of the reference ion between S2 and Cave C. The parameters $D_{S0->S2}$ and $D_{S2->CC}$ correspond to the optical dispersion presented by the FRS from S0 to S2 and from S2 to Cave C. Finally, ΔX_{S2} and ΔX_{CC} are the deviations with respect to the reference trajectory and the incident position of the secondary beam along the dispersive coordinate at S2 and Cave C, respectively. Considering the reference trajectory is centered, these are directly the horizontal positions (X) measured at S2 and Cave C.

Parameter	$(B\rho_{S2->CC})_0$	$D_{S0->S2}$	$D_{S2->CC}$
Value	11.6398 [Tm]	67.8 mm/%	110.0 mm/%

Table 2.5: *Constant parameters used for the calculation of the secondary beam mass over charge ratio.*

Therefore, the mass over charge ratio (AoQ) can be obtained by combining equations 2.5 and 2.6, resulting:

$$\frac{A}{q} = \frac{(B\rho_{S2->CC})_0 \times \left(1 + \frac{\Delta X_{S2}}{D_{S0->S2}} + \frac{\Delta X_{CC}}{D_{S2->CC}}\right)}{3.107 \times \beta\gamma} \tag{2.7}$$

In order to improve the resolution of the mass over charge ratio, its dependence with the secondary beam angle should be corrected, as shown in figure 2.11. Therefore, the final identification for the ^{236}U projectiles is obtained from equation 2.7 after this correction. In figure 2.12, it is displayed the energy loss in Triple MUSIC vs the AoQ, only for the selected Z=92 events (as explained in section 2.4.1 and depicted in figure 2.8). One can observe that for Z=92 there are two isotopes reaching the Cave, ^{236}U and ^{237}U. For further analysis, only ^{236}U projectiles will be selected. Lighter Z nuclei are not considered in this work.

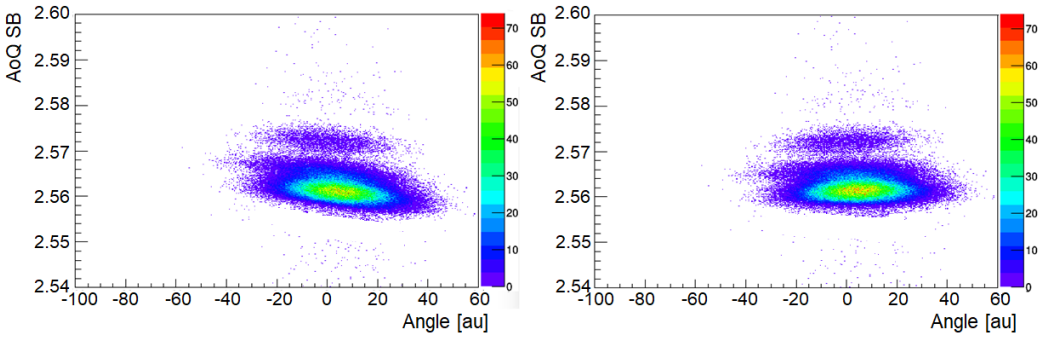

Figure 2.11: *Secondary beam AoQ ratio vs horizontal angle. Left: Uncorrected correlation. Right: Corrected correlation.*

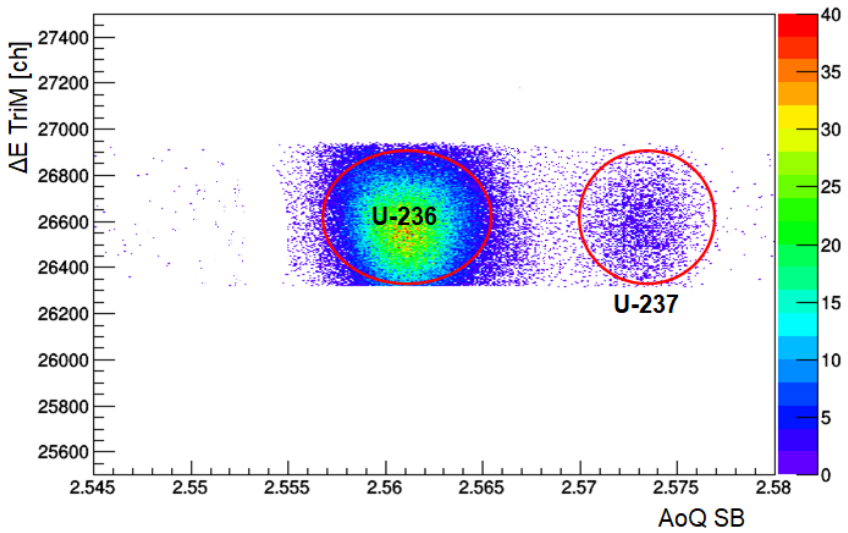

Figure 2.12: *Identification of the uranium isotopes reaching the fission target.*

2.5 Fission Fragments Identification

In this section we describe the detectors and methods used for the isotopic identification of the fission fragments. Fission reactions are induced in an active target, allowing us to determine where and how fission has been produced. After the reaction is triggered, the positions, energy loss and time-of-flight of the fission fragments are measured by the SOFIA detectors downstream of the target (see figure 2.3).

2.5.1 Active Target

SOFIA Active Target specifications

An active target is a relatively novel detector concept in nuclear physics [83]. It can work simultaneously as a target as well as a gas detector, hence its name. The SOFIA active target is a cylindrical shaped volume, filled with a gas mixture. It consists of nine layers of matter, five thin layers working as anodes and four thicker layers acting as cathodes. These four cathode layers indeed serve as targets, being sandwiched by two anode layers to create the ionization chamber volume, as seen in figure 2.13.

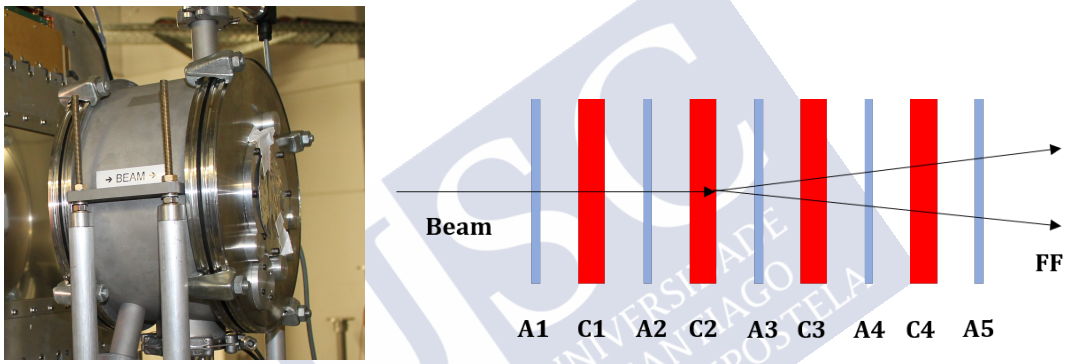

Figure 2.13: *Left: Image of the active target mounted for the experiment. Right: Sketch of the active target configuration. In this example, fission is produced in the second cathode.*

The use of target layers of a wide range of atomic number allows to trigger coulex- and fragmentation-induced fission reactions. For this purpose, three high Z target layers, two made of uranium and another one of lead, and one low Z target layer of aluminum were used. The thickness of the layers are listed in table 2.6. So, apart from the two already mentioned advantages, namely triggering fission and selecting the reaction starting point, the use of this active target has the extra advantage of inducing fission by two different ways and also measuring the total kinetic energy with good resolution.

Identification of fission location

When ions go through the active target, they ionize the gas creating a signal on each anode. From the energy losses measured on the anodes

Gas mixture	90 % Ar, 10% CH_4
Voltage of cathodes	-400 V
Distance anode-cathode	15 mm
Cathodes 1 and 2	Uranium, 600 μm
Cathode 3	Aluminum, 500 μm
Cathode 4	Lead, 125 μm
Anodes 1 and 5	Aluminum, 15 μm
Anodes 2,3 and 4	Aluminum, 50 μm

Table 2.6: *Technical information of the active target.*

upstream and downstream of a specific target layer, it is possible to know whether fission has taken place in this layer or not. The argument followed to determine the fission location can be explained using the relation between the ion energy loss and its atomic number.

According to Bethe-Bloch formula [104], the relation between the energy loss and the atomic number is: $\Delta E \propto Z^2$. Considering that fission fragments have half of the atomic number of the secondary beam, one can assume that $\Delta E_{FF} \propto \Delta E_{SB}/2$, being the energy loss measured on each anode two times lower when fission takes place than when secondary beam passes without reacting. Thereby, fission location can be unambiguously identified, distinguishing between five different cases, which are described below and displayed in figure 2.14:

Case a: If the energy loss on each consecutive anode is the same, and it is maximal, this means that the beam has passed without reacting.

Case b: If the energy loss is maximal in one anode and minimal (around half of the value) in the other, this implies that fission has occurred in the corresponding target.

Case c: If the energy loss is the same but minimal in both anodes, fission has already occurred.

Case d and e: In the other two cases, fission has occurred in one of the anodes surrounding the target.

After this identification, the percentage of fission reactions on each target is 82.3 % in the first two uranium layers (41.3 % in the first and 41.0 % in the second), 14.3 % in the aluminum layer and just 3.5 % in the last lead target.

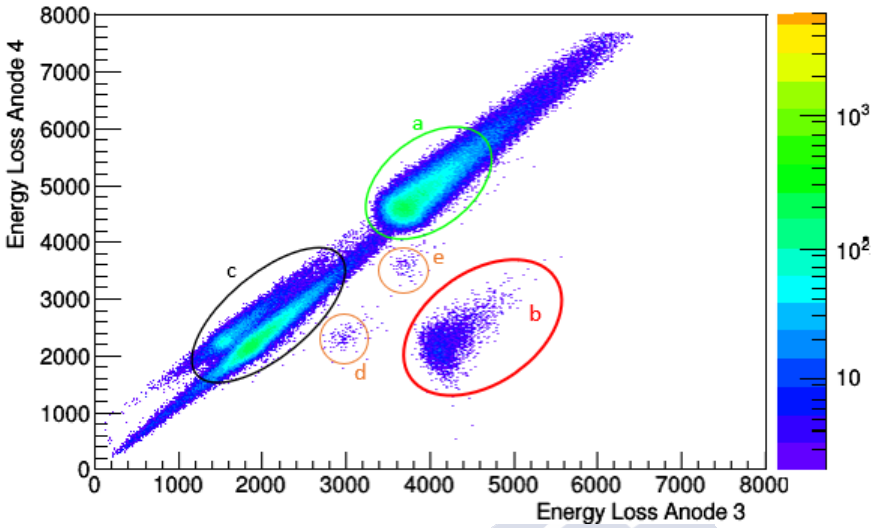

Figure 2.14: *Energy loss in surrounding aluminum's target anodes. Different cases are shown, being the same for every target layer.*

2.5.2 Twin MUSIC

Twin MUSIC specifications

The Twin MUSIC detector [92] is a double multi sampling ionization chamber dedicated to measure the energy loss of the fission fragments. An image of this detector is shown in figure 2.15.

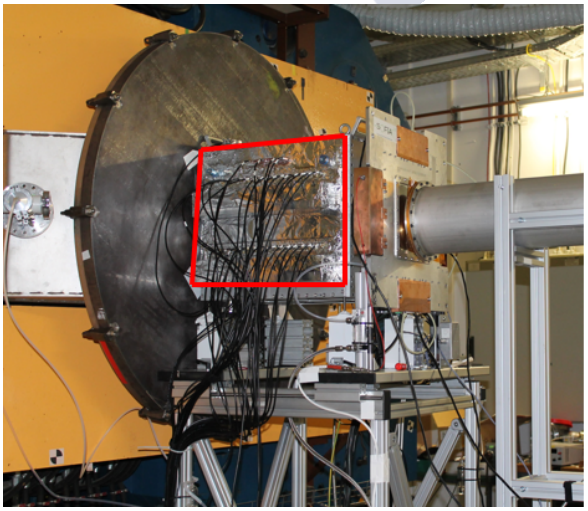

Figure 2.15: *Image of the Twin MUSIC (inside the red square) placed right before ALADIN. MWPC1 is placed in front of this detector.*

This gaseous detector consists of two vertically divided identical parts, hence its name, sharing a central cathode plane. Both anode planes are positioned near the boundaries of the detector with one on each side (right and left), being separated from the cathode by a distance of 113 mm, with a frisch grid placed very close to the anode plane. An interesting particularity of this detector is that each anode plane is also segmented into two parts, up and down, along the beam line, for a total of four identical sections (see figure 2.16). This segmentation allows for a better tracking of the fission fragments. Each half of the anode plane is composed by eighteen anodes, two screening anodes on both ends and sixteen effective anodes in the middle to perform the correspondent measurements. The technical information is summarized in table 2.7.

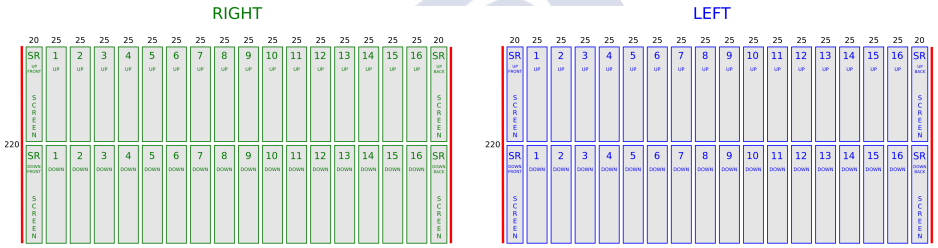

Figure 2.16: *Side view of both sides of the Twin MUSIC. They are identical and subdivided in two subsections. Effective sizes are displayed*

In the same way as in the Triple MUSIC, each internal anode returns two independent quantities: the energy loss of the ion and the drift time of the electrons from their ionization point to the anode plane. The first quantity allows for the fission fragment charge identification. The second allows to track the traveled path of the fragment and extract its horizontal angle as it will be explained below.

Gas	P75= 75% CH_4, 24.5% Ar +0.5% CO_2
Pressure	1.02 bar
Distance cathode-frisch grid	110 mm
Distance anode-frisch grid	3 mm
Active volume	110 x 220 x 400 mm^3
External volume	430 x 480 x 550 mm^3

Table 2.7: *Twin MUSIC technical information.*

Fission fragments energy loss

The Twin MUSIC allows to measure the fission fragments energy loss. As it is segmented in two parts, left and right, two independent measurements are performed on each section of the detector. So, for an ion flying through the right side of the Twin, for example, its energy loss is calculated as indicated in equation 2.8, where ΔE_{RU_i} and ΔE_{RD_i} represent the energy loss on each anode of the right upper and lower part, respectively. Note that anode 1 and anode 16 are removed out of the analysis, as they present bad signals due to the fact of being too close to the screening anodes.

$$\Delta E = \sum_{n=2}^{15} \Delta E_{RU_i} + \Delta E_{RD_i} \tag{2.8}$$

Performing these two measurements, it is possible to select only fission reactions events, separating these from fragmentation reactions or some beam events passing through the target without reacting, as seen in figure 2.17. The events inside the red triangle correspond to fission fragments and this selection will be applied for later analysis. From here, one can obtain the atomic number Z of each fission fragment, performing different corrections that will be explained in section 2.5.5.

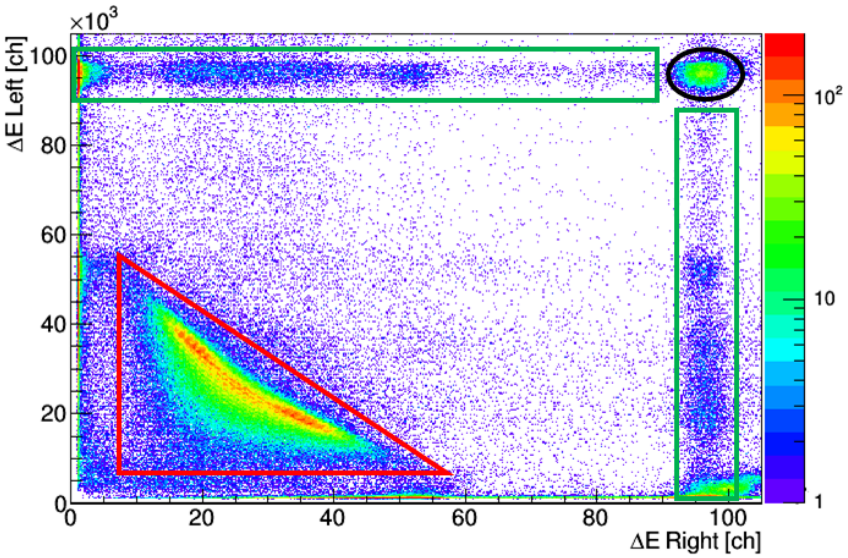

Figure 2.17: *Plot of the energy loss signals registered on both sides of the Twin MUSIC. Fission fragments are located in the red triangular window. The black circle corresponds to beam events and the green rectangles to fragmentation reaction products.*

Extraction of the horizontal angle

The second piece of information that the Twin MUSIC is able to provide is the drift time values which can be used to extract the angle in the plane XZ as follows:

1. Figure 2.18 shows an example of the drift time measured on anode 7. It is easy to recognize both the frisch grid (FG) and cathode signals (Cat). The distance between them is $D_{Cat-FG} = 110mm$, so it is straightforward to extract the drift time velocity for each anode, v_{drift}= $\frac{D_{Cat-FG}}{DT}$, being DT the drift time difference between the cathode and the frisch grid. The values obtained are very similar for all 16 anodes in a section, but a different drift velocity value for each anode is computed in order to be more precise in the analysis. The average drift velocity is around 56.5 mm/μs for left side anodes and 55.7 mm/μs for the right ones.

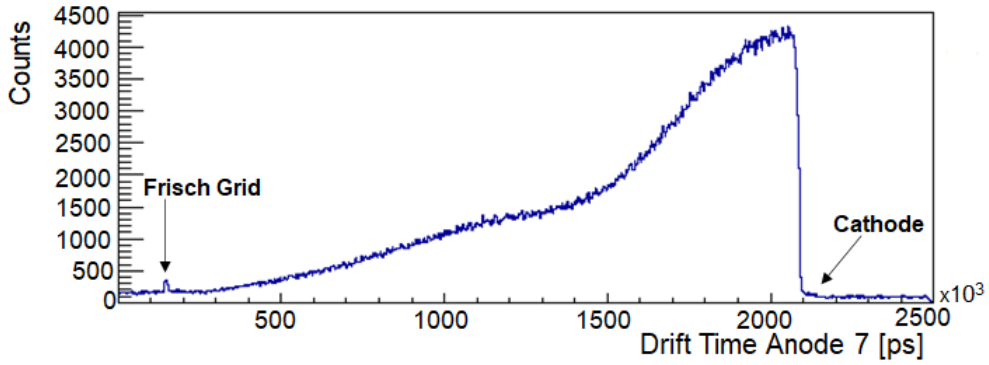

Figure 2.18: *Drift time measurement for anode 7 in the left up part. Cathode and Frisch grid signals are highlighted.*

2. Once the drift velocity is obtained, the X position of the fragments along each Twin side can be reconstructed in an event-by-event basis, as shown in figure 2.19. The dots represent the measured X position of the fragment on each anode being the horizontal angle derived from a linear fit of these positions. The difference between the measured value and the fitted value for each anode (called residual) can be obtained as well.

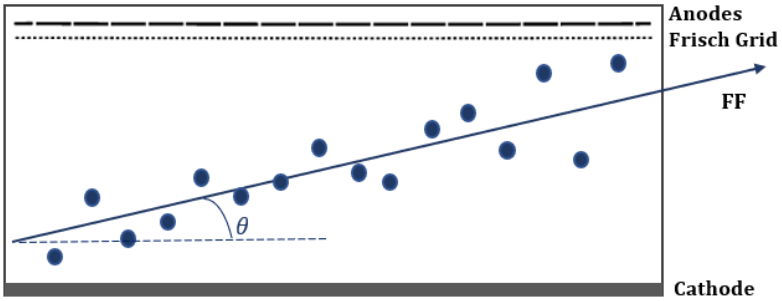

Figure 2.19: *Example of the reconstructed track of a fragment along the Twin MUSIC.*

3. The X positions previously calculated can be optimized by correcting the dependence between the residual and the measured position, by a small refinement in the drift velocity value. After this correction, the position resolution of the Twin MUSIC is obtained, being around 60 μm for the eight more internal anodes. Only these eight anodes are used to compute the horizontal angle as the resolution is worst in the most external ones. More details are given in reference [99].

4. After this correction, the horizontal angle is finally calculated for each section. The final angular distribution for fragments passing left and right is obtained, going from 0 to $\pm$ 45 mrad, peaking around $\pm$ 20 mrad.

2.5.3 MWPC1 and MWPC2

SOFIA MWPC1 and MWPC2 specifications

Two MWPCs, labeled as MWPC1 and MWPC2, are used to measure the fission fragments X and Y positions. Compared with the MWPC0 that measures the secondary beam positions, there are a few differences concerning sizes and detector design that must be commented.

MWPC1 is placed before the magnet and presents an horizontal segmentation of the X strips plane in two identical parts. This detector has then three sets of planes, two for measuring fission fragments X positions and one for measuring their correspondent Y position. The reason for this segmentation comes from the fact that two pair of positions are measured, and it is not simple to assign a pair of X and Y positions to one specific

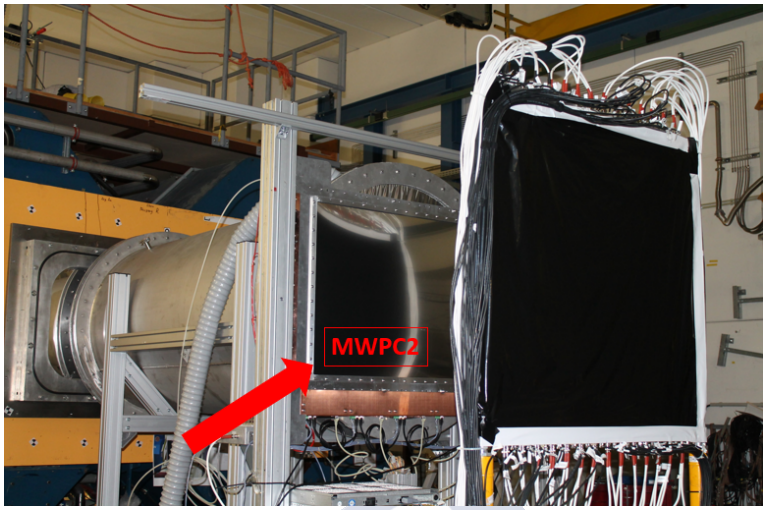

Figure 2.20: *Picture of the setup after ALADIN magnet. Red arrow points to MWPC2.*

fragment. By having the X strips plane segmented in an upper and a lower half, in the most common scenario, one fission fragment will impinge on the half beyond the beam axis and the other one will impinge on the half below, so they can be associated, respectively, with the maximum and minimum values measured for the Y position without confusion. Also, in the cases that both fragments fly through the same X half, the association can be done with other detector information.

MWPC2 has the same design as MWPC0, without the segmentation presented in MWPC1. The only relevant change lies in the dimensions, presenting more X and Y strips. This detector stands after ALADIN (see figure 2.20), having the fission fragments positions a bigger spread because of the deflection caused by the magnet. In order to guarantee a good detection efficiency, the area of the detector is increased.

Information of MWPC0 is given in table 2.4. MWPC1 presents the same particularities except for the above-mentioned extra cut in the X planes. Information about the MWPC2 is listed below:

Dimension	900 x 600 mm^2
Number of strips	287(X); 120(Y)

Table 2.8: *MWPC2 dimensions.*

Fission Fragments position measurements

To correctly associate the X and Y positions measured for both fission fragments on MWPC1 and MWPC2, the following steps have to be carried out:

1. First, two positions X and two positions Y are obtained with MWPC1. The reconstruction algorithm is the same as for the MWPC0 [103], explained in section 2.4.3. In this case, two maximal signals are looked for and two pairs of positions are measured. As explained before, each position X needs to be correctly assigned with a position Y, taking advantage of the segmentation of the X strips plane in two halves. The positions given by MWPC1 are displayed in figure 2.21, having two pairs of positions here $(X^{up}, Y^{up})_{MWPC1}$ and $(X^{down}, Y^{down})_{MWPC1}$.

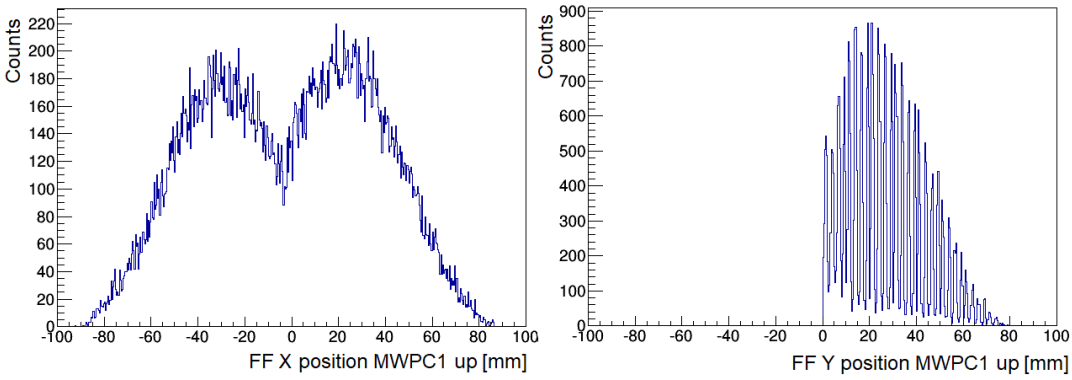

Figure 2.21: *MWPC1 X and Y positions for the upper fragment. The resolution for the Y position is appreciably worst.*

2. Then, the same is done for MWPC2. Again, two pairs of positions X and Y are measured and need to be correlated between them. This detector is not segmented, but the correct correlation is obtained by using the vertically segmented time-of-flight wall placed right after the multiwire. At the end, one has $(X^{up}, Y^{up})_{MWPC2}$ and $(X^{down}, Y^{down})_{MWPC2}$.

3. To check if the positions are well correlated for each detector, one can reconstruct the azimuthal angle (ϕ) from the fission fragments' positions measured in both MWs and calculate their difference. If everything is correct, this distribution should be centered around π rad [58], as shown in figure 2.22.

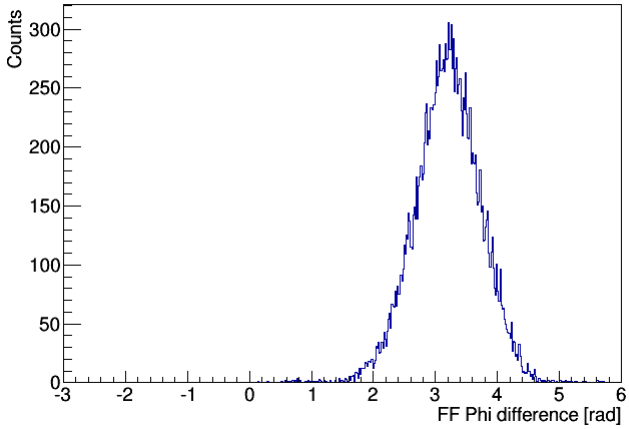

Figure 2.22: *Difference between both fission fragments ϕ coordinate obtained from positions measured in MWPC2. Peak is centered around π rad.*

4. Finally, we need to check if the positions of the fission fragments upstream and downstream ALADIN are consistently assigned. Because a dipole magnet only deflects particles in the horizontal coordinate, imposing the condition of equal sign on the Y coordinate before and after the magnet, two pairs of coordinates for each fission fragment are unambiguously assigned, as shown in figure 2.23. The position correlation shown in this figure demonstrates the correct identification of the trajectories of the two fission fragments. The small jump presented around X=0 is an artefact from the Twin MUSIC cathode.

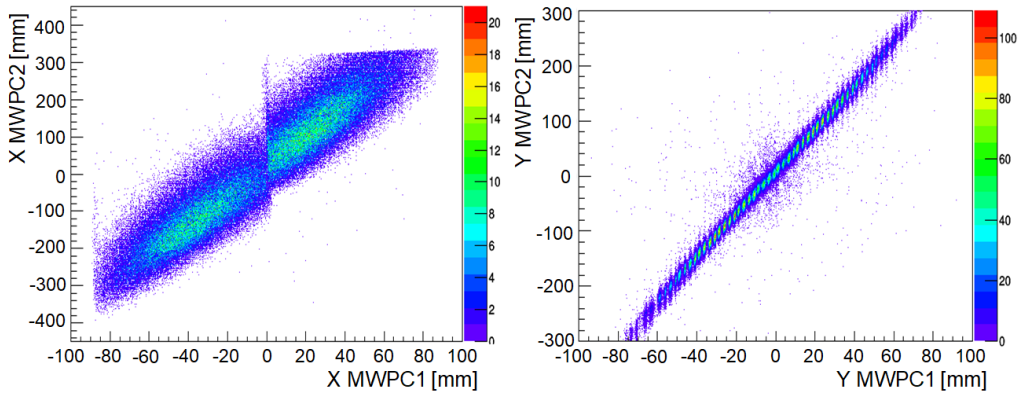

Figure 2.23: *Left: Correlation of X coordinates computed in both MWPC. Right: Correlation of Y coordinates computed in both MWPC.*

2.5.4 ToF Wall

SOFIA ToF Wall specifications

The time-of-flight measurements for the fission fragments are carried out between the plastic scintillator located at the entrance of the Cave C and the detector known as time-of-flight wall, whose specifications are treated in this section.

The SOFIA ToF Wall [94] is a set of 28 vertically-placed plastic scintillators. All of these 28 plastic slats were coupled to a pair of PMTs, one at each end. Combining the signal times provided by these two PMTs, the fragment incident time and vertical position can be derived. The absolute ToF measurement for each fission fragment is obtained as the difference between the start scintillator and the ToF Wall plus a time-of-flight offset specific for each plastic slat. Pictures of the ToF wall are displayed in figure 2.24.

Figure 2.24: *Images of the ToF Wall used in this experiment. Left: The 28 plastic slats with their correspondent pair of PMTs can be seen. Right: Wire connected ToF Wall with black wrapping protection to avoid light interference.*

The ToF wall is placed right after the MWPC2, being the last detector of the setup. As well as MWPC2, this detector presents a large surface to deal with the position spread of the fission fragments induced by the magnet. Two different photomultipliers types were used in the experiment [95], being

the ones used for the center slats, where fission fragments impinge more frequently, the most precise (check table 2.9 for complete information).

Plastic scintillator	EJ228
Active surface	5 x 900 x 600 mm^3
Number of plastic slats	28
PMTs	19 pairs of Hamamatsu 6533 in the center 9 pairs of Hamamatsu 10580 at the edges

Table 2.9: *ToF Wall technical information.*

Finally, it is also important to mention that the ToF Wall also works as fission trigger. When two fragments reach the ToF wall, four signals corresponding to the two PMTs from two different slats are produced, being this the fission trigger condition. Fragmentation events can also produce this kind of signals, so the energy signals in both sides of Twin MUSIC also help for the correct analysis, as was explained in section 2.5.2.

Time-of-flight and vertical position measurements

The subtraction between the ToF Wall and the start detector time signals gives a raw time-of-flight for the fission fragments that needs to be calibrated. In this case, the calibration is rather laborious because each plastic presents a different time offset, being necessary to calibrate all of them independently.

To perform the calibration, different ^{238}U primary beam sweep runs were used. We need that the primary beam with defined energy impinge the 28 plates of the ToF Wall. For this purpose, the magnetic field of the ALADIN dipole is changed in order to change the position of the beam downstream of the magnet.

Similar to the secondary beam time calibration, based on equation 2.4, the time offset for each plastic can be obtained as:

$$\Delta ToF_i = \frac{LoF_i}{v_{PB}} - ToF_i \tag{2.9}$$

where ToF_i is the time-of-flight measured between the start scintillator and each slat (i=1,2...,28), v_{PB} is the velocity of the primary beam computed taking int account the energy losses with LISE ++ or ATIMA [105]. LoF_i is the length of flight path for each plastic slat, using the geometrical model

explained in [99]. After the analysis of the sweep run files, a time-of-flight offset for each plastic slat is obtained.

This allows to obtain the fission fragments time-of-flight, just summing up the plastic offset to the measured time-of-flight. A small correction has to be done, considering that the start scintillator is placed before the active target, so a small part of the measured time-of-flight corresponds to secondary beam time-of-flight. Knowing the distance between this scintillator and the target where fission is produced, this contribution is easily removed. Thus, for the fission fragments, two values of the time-of-flight are measured in an event-by-event basis and need to be correctly assigned to the pair of positions previously measured in the MWPCs. To check if this assignment was correctly done, the fission fragment X coordinate measured in the MWPC2 is plotted versus the plastic hit by each fission fragments, which is equivalent to the X coordinate in the ToF Wall (figure 2.25). The correlation is linear, as expected, seeing the widths of the plastics in the plot.

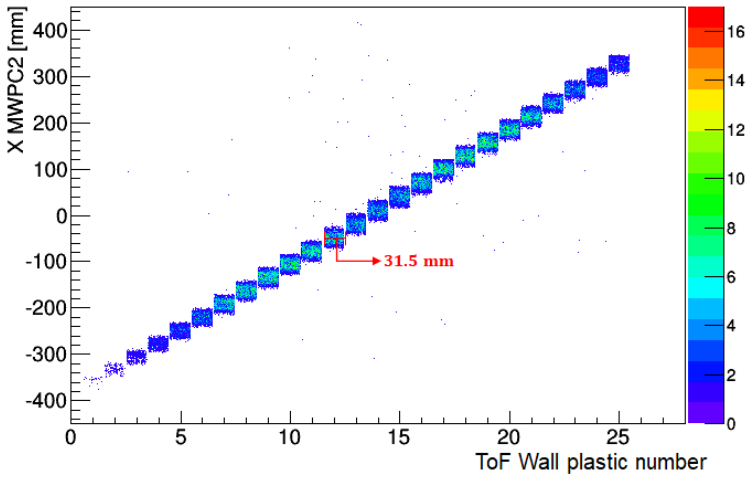

Figure 2.25: *Correlation of the X position in MWPC2 for the fission fragments as a function of the number of the ToF Wall plastic (X coordinate).*

The ToF wall can also provide a vertical position measurement for each fragment, used to correctly associate X and Y positions in MWPC2. Also, this MWPC2 can serve to calibrate the raw Y position measured in the ToF wall. In figure 2.26, the calibrated Y position obtained with the ToF wall is plotted vs the plastic slat where the fission fragment has impinged. The particular shape displayed corresponds to the kinematics of the process. This shape comes from the fact that the fission fragments are transmitted in forward direction forming a cone, with more events located externally [106].

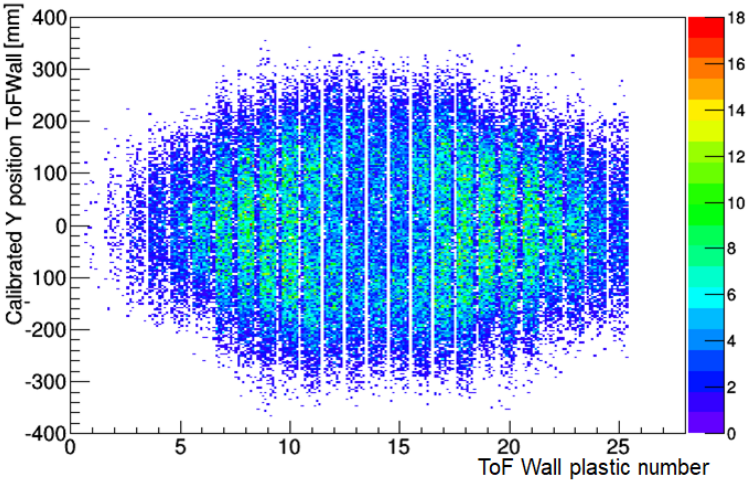

Figure 2.26: *Correlation between the Y position in the ToF Wall as a function the number of the ToF Wall plastic (X coordinate). The shape presented corresponds to the kinematics of the fission process.*

2.5.5 Determination of the atomic number of fission fragments

From the energy loss measurements performed on the Twin MUSIC, explained in section 2.5.2, the atomic number of the fission fragments can be extracted. Only fission events produced by ^{236}U in active target cathodes are going to be matter of study. In order to achieve a good identification and a correct resolution, some calibrations and corrections need to be done as it will be carefully explained below.

Time-of-flight correction

The dependence existing between the energy loss and the time-of-flight relies on the fact that the energy deposited by an ion depends on its kinetic energy. The higher it is, the lower the energy deposited. This correction is shown in figure 2.27.

Other corrections performed

Some dependencies of the energy loss with X positions in MWPC1 and MWPC2 can be corrected in order to improve the resolution. To correct the dependence with MWPC2, just a small refinement on the ToF offset value calculated in section 2.5.4 is needed. This is a minor dependence but more relevant for higher energy losses.

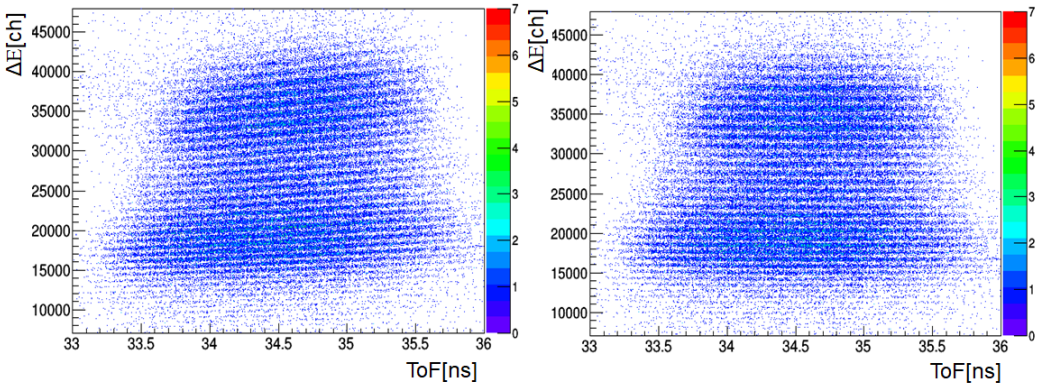

Figure 2.27: *Energy loss in the Twin MUSIC as a function of the time-of-flight for the fission fragments. Left: Uncorrected correlation. Right: Corrected correlation.*

The correction with MWPC1 position is more meaningful. As shown in figure 2.28, close to X=0 mm there is an important drop. This drop is an effect emerging from the central cathode of the Twin MUSIC, as the ionization electrons produced there may be poorly absorbed or even go through the opposite section of this detector. So these events are simply removed. Then, a small linear dependence is also noticed, being the energy loss (and thus the atomic number) slightly lower for higher X values. This is also corrected and resolution is improved.

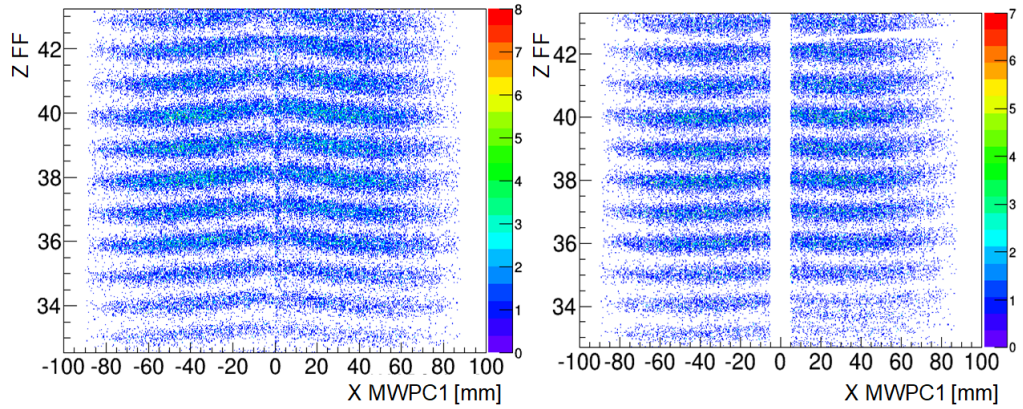

Figure 2.28: *Fission fragment atomic number vs MWPC1 X position. Left: Close to X=0, cathode effect is important and resolution is degraded. Right: Events close to X=0 are removed and the dependence is corrected.*

Z identification from corrected energy loss

Once the energy loss is corrected, the energy loss spectrum of the fission fragments is shown in 2.29. Each peak corresponds to one particular atomic number.

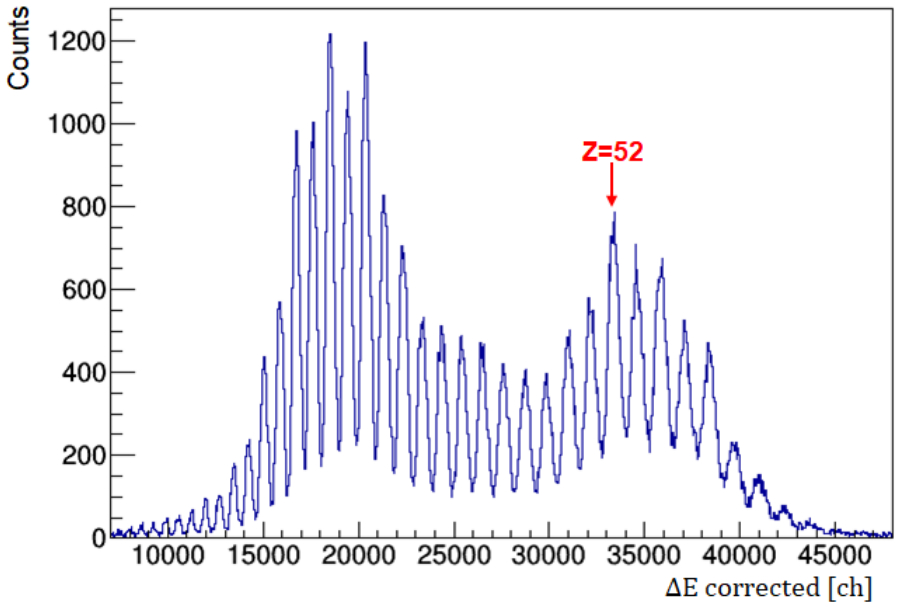

Figure 2.29: *Energy loss in the Twin MUSIC after the forementioned corrections. Lighter nuclei present better resolution than heavier ones.*

To perform a correct assignment, only fissions produced on the first two uranium target layers have been selected. In these targets, fission is induced by coulex reactions. In this kind of processes, the elements with an even atomic number are more produced than their neighbors [107]. So this permits to assign to the highest peak on the heavy fragment group (higher energy loss) an even Z, which in our case is going to be assigned to Z=52, in order to obtain a dominant peak in Z=92 when both fission fragments atomic numbers are summed up. According to that, the other peaks are associated with its correspondent atomic number. Then, we can pass from energy loss to atomic number considering that ΔE is directly proportional to Z^2.

Atomic number efficiency correction

The transmission of the fission fragments through the experimental setup presents several geometrical constraints that should be studied in order to obtain the correct atomic number spectra.

The first limitation comes from the Twin MUSIC, where the atomic number is deduced. In this detector there is a dead zone produced by the central cathode losing the events passing close to it. Additionally, there is the possibility of both fission fragments flying through the same section (out of the four available) of the detector, making impossible their distinction. Other limitation comes from the MWPCs, more specifically from the pipes placed in front of them. There are some fragments that can hit the wall of the pipes, not being able to reach the detectors. Finally, the bigger constrain presented by the experimental setup is caused by the time-of-flight wall geometry. Due to the bigger angular aperture of the light fragments, some of them will not reach the ToF-Wall. Moreover, the lighter fragments will produce less energy deposition in the ToF-Wall plastic, resulting in lower detection efficiency. It has also been explained that the central plastics have better PMTs, due to the fact that most part of the fission fragments will reach them. This translates in a better intrinsic efficiency to convert the energy loss into light. The geometrical efficiency of the setup was obtained and is displayed in figure 2.30, on the basis of the work described in [99]. The mean efficiency is close to 90% but it decreases quickly and equally for heavier and lighter fragments.

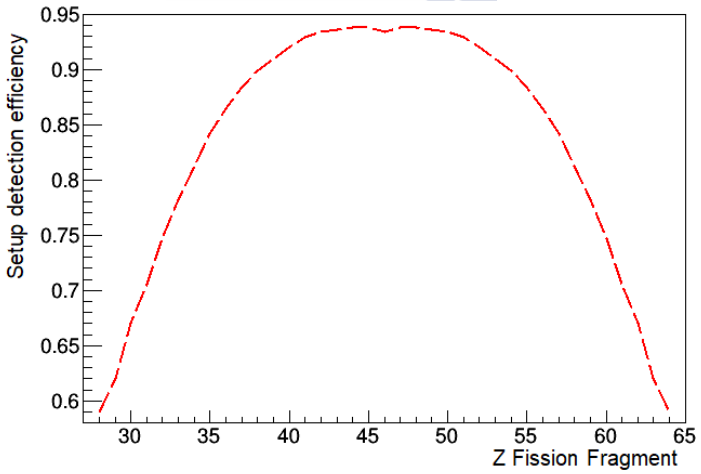

Figure 2.30: *Experimental setup detection efficiency. Figure obtained on the basis of the work described in [99].*

Fission fragments Z distribution obtained with different targets

Fission can be triggered in any of the four active target layers. The analysis will be focused on the study of the fission reactions ^{236}U+U and ^{236}U+Al, so the fission fragments Z distribution for these two reactions are displayed in 2.31. Fissions induced in the lead target are not considered due to the low statistics. The resolution obtained is around 0.36 units of charge for the lightest fragments and around 0.43 for the heaviest ones.

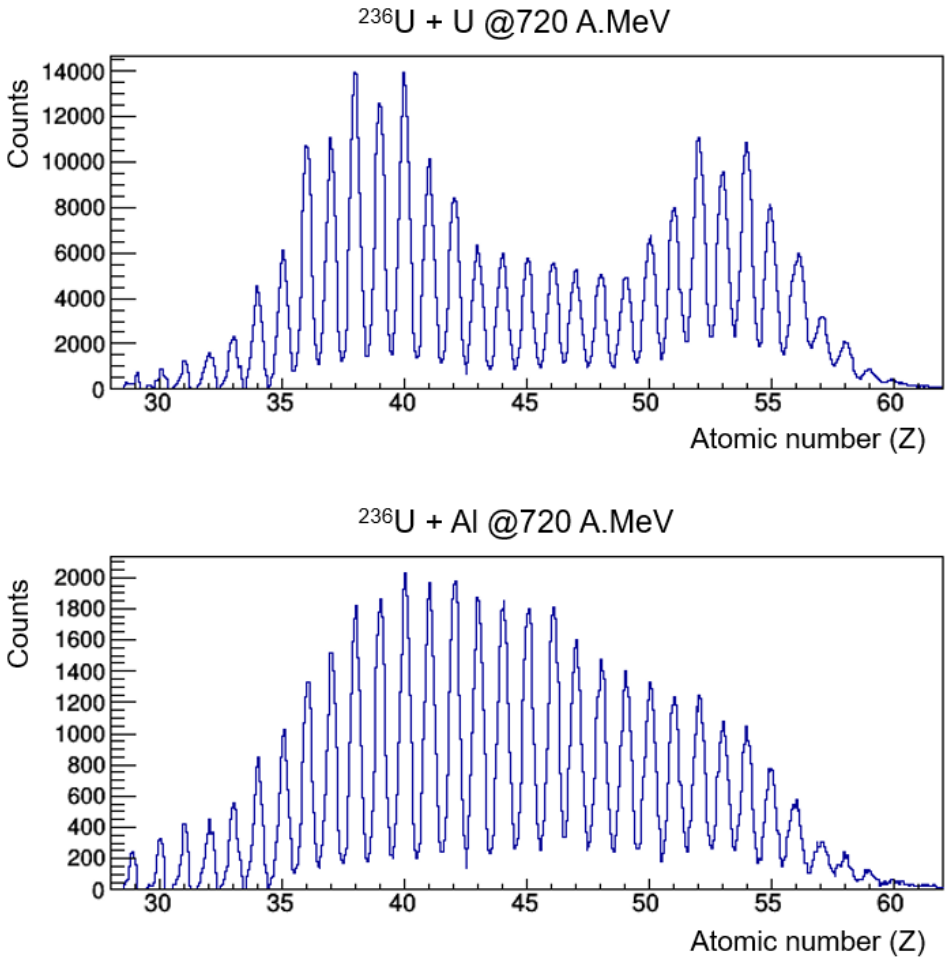

Figure 2.31: *Atomic number of fission fragments for the ^{236}U+U (upper panel) and the ^{236}U+Al reactions (lower panel).*

Fragmentation-induced fission reactions are dominant on the Al target and also has a contribution in reactions on the two U layers, even though here the coulex contribution is dominant. One can observe the differences

between those processes in the atomic number distributions, being symmetric when fission is induced by nuclear collision and asymmetric for those induced by coulex [108]. Moreover, in figure 2.32, we display the sum of the fission fragments atomic number. The contribution to Z=92 is much bigger for U target layers than Al, due to coulex-induced fission contribution. Other systems require the loss of protons, being the interaction with the electromagnetic field not enough to induce this loss. It is observed a small peak in Z=93, coming from charge-exchange reactions [109]. Further details will be explained and analyzed in the next chapter. In figures 2.33 and 2.34 the atomic number correlation of both fission fragments from fission of ^{236}U in the uranium and aluminum target are presented as scatter plots.

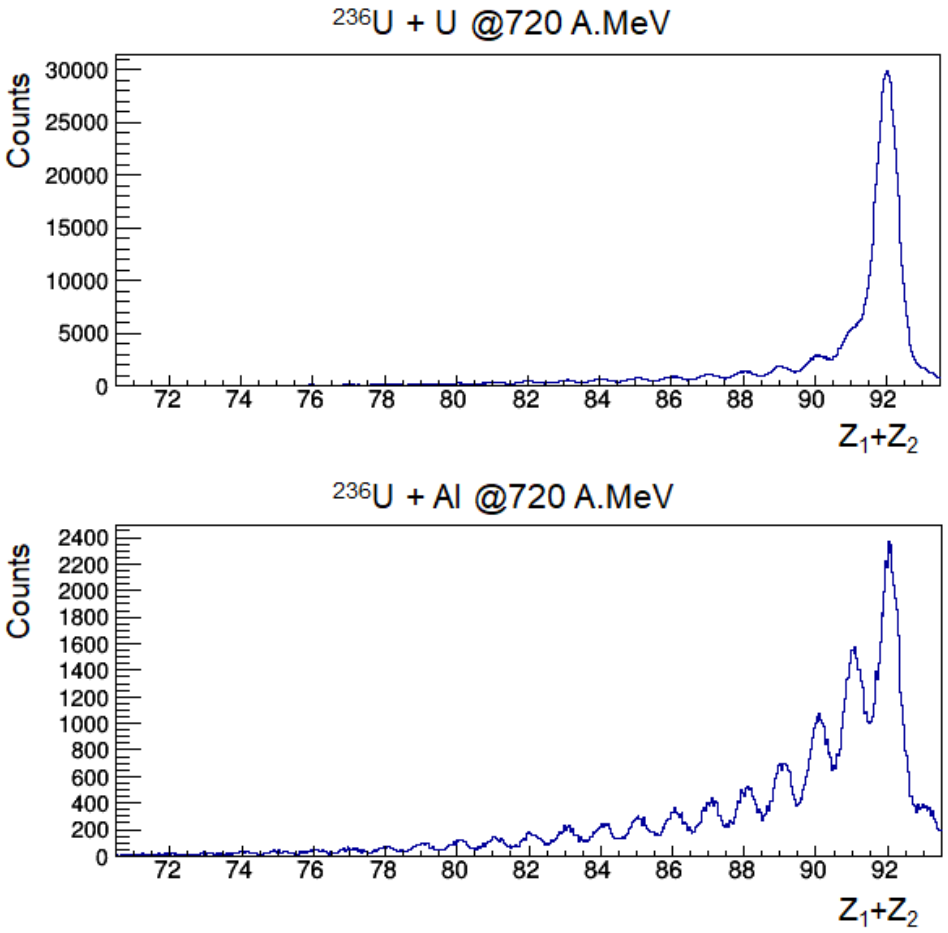

Figure 2.32: *Sum of the fission fragments atomic number, for ^{236}U+U (upper panel) and for ^{236}U+Al reaction (lower panel).*

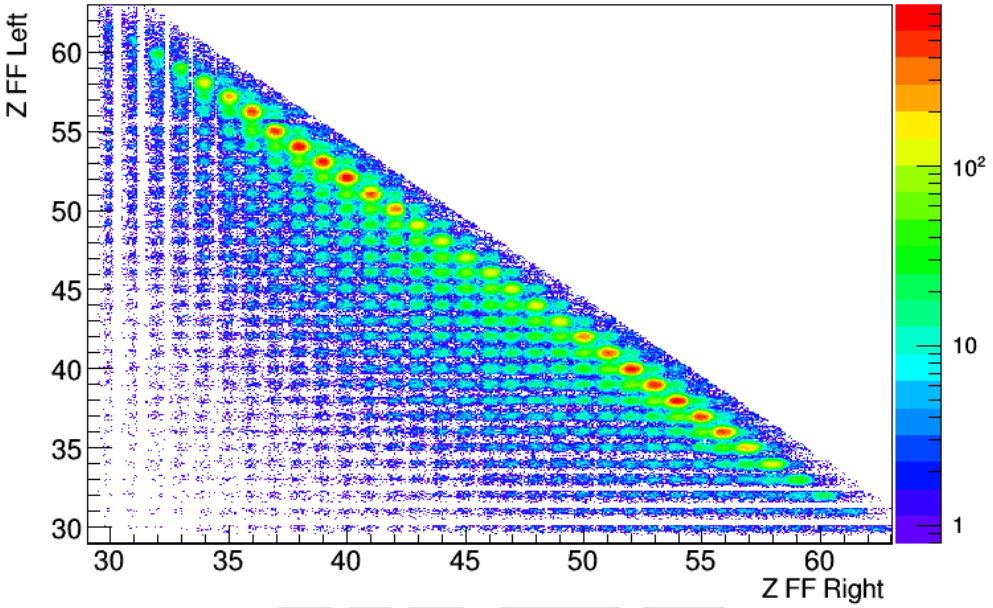

Figure 2.33: *Scatter plot of both fission fragments atomic number produced in* ^{236}U*+U reactions.*

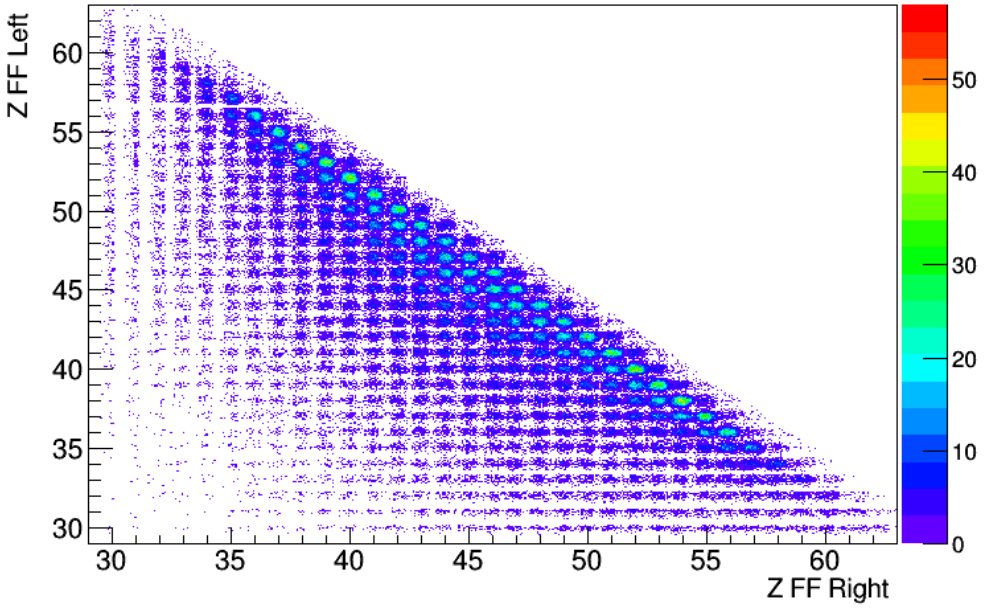

Figure 2.34: *Scatter plot of both fission fragments atomic number produced in* ^{236}U*+Al reactions.*

2.5.6 Determination of the mass number of the fission fragments

The derivation of the mass number of the fission fragments permits the complete identification of the produced nuclei. From the position and angle measurements explained in sections 2.5.3 and 2.5.2, respectively, the fission fragment trajectory can be reconstructed, hence its curvature radius and magnetic rigidity. Then, together with the time-of-flight measurements and the atomic number, the mass number is deduced. In order to get a good resolution and separate the fission fragments masses, the tracking and time-of-flight resolution requirements are strict. The detectors used in the experiment should present the following resolutions, given in FWHM:

Detector	Resolution
MWPC1	200 μm (X); 1 mm (Y)
MWPC2	300 μm (X); 1 mm (Y)
Twin MUSIC	60 μm (X); 0.5 mrad (θ)
ToF Wall	40 ps (ToF); 3 mm(Y)

Table 2.10: *Resolutions required for the detectors used in the present experiment.*

From equation 2.1, knowing the values of the corresponding constants and considering fully stripped fission fragments with q=Z, the equation can be rewritten to obtain the mass number as follows:

$$A = \frac{B\rho \times Z}{3.107 \times \beta\gamma} \tag{2.10}$$

On the basis of the work carried outby Adrich [110], the motion of a charged particle through the ALADIN magnetic field can be described using a geometrical model, which allows to compute the deflection of the particle trajectory inside a constant magnetic field. The fragment trajectory and its magnetic rigidity can be reconstructed following the equations described in [99], which are specifically adapted for this experimental setup. They are computed from the measured positions before and after the magnet and also the horizontal angle and other fixed parameters like the detector positions and the magnet bending power. Then, with the ToF measurements, velocity is also known and therefore $\beta\gamma$.

Time-of-flight resolution

The time resolution obtained in the experiment can be determined using a set of runs with primary beam and without the active target in the beam line. Measuring the time-of-flight between the start scintillator placed in Cave C and the ToF Wall, the width of the time-of-flight distribution will mostly correspond to the time-of-flight resolution. In figure, 2.35, the time-of-flight distribution for a ^{238}U primary beam measurement at 750A MeV is shown. Fitting the distribution to a gaussian function, a time-of-flight resolution of around 78 ps is found.

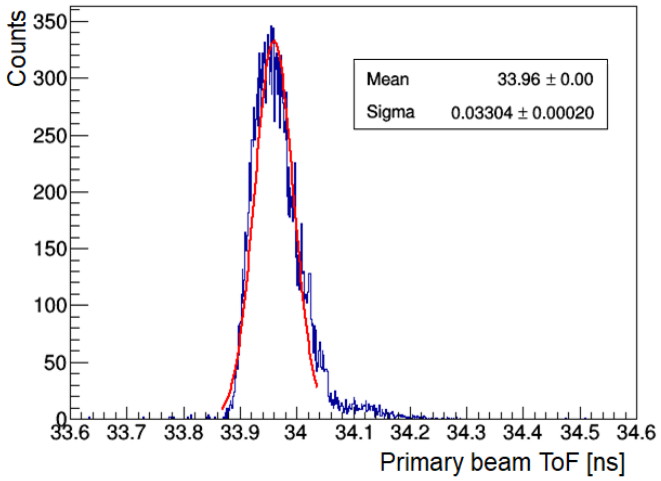

Figure 2.35: *Time-of-flight of the primary beam measured at Cave C. The legend shows the gaussian fit parameters.*

This width is not exactly the intrinsic resolution of the time-of-flight measurement, as there are some other effects that can broaden the distribution. They need to be evaluated and subtracted to obtain a more precise value. First is the trajectory spread caused by the magnet. This spread has been evaluated and results to be of 2 mm, so the effect over the time-of-flight will be 8 ps. Also, the primary beam presents a momentum spread of around 0.1%. Taking into account that the Cave C flight path is approximately 8.1 m, this spread produces an uncertainty of 18 ps over the time-of-flight. The last effect is the straggling induced by the detectors at the Cave C. As the active target was removed, the straggling comes mainly by the gas mixtures of the detectors. Using ATIMA [105] to compute this straggling, its uncertainty over the time-of-flight is estimated to be 11 ps. So these three

contributions are small in comparison with the 78 ps obtained for the primary beam time-of-flight. Assuming that the uncertainty sources are independent, they can be quadratically subtracted to the above obtained value, resulting in an intrinsic resolution in the time-of-flight measurement of 74 ps, nearly twice worse than the expected one. This translates in an important loss of resolution in the mass reconstruction, resulting to be between 0.9-1.0 units of mass for the lighter fragments and between 1.4-1.5 for the heavier ones.

Besides, during the experiment the scintillator placed at Cave C was damaged during a setting with primary beam, causing a yellow spot observed after the experiment. This produced a non-uniform propagation of light to both sides, causing an important loss of resolution for ToF measurements. In figure 2.36 (right), the raw position measured by this scintillator is plotted as a function of the MWPC0 position. If everything was correct, correlation should be linear as both detectors stand one against each other, as can be observed in 2.36 (left), where the same is plotted for a primary beam run, before the scintillator was damaged.

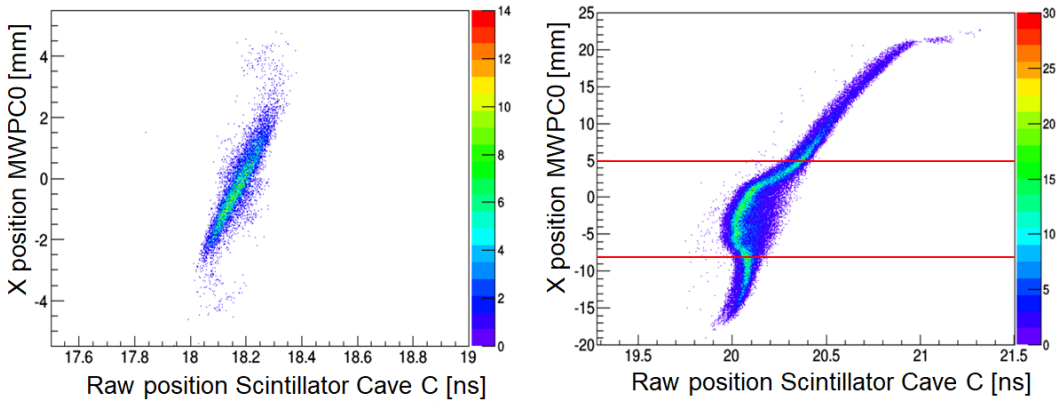

Figure 2.36: *Left: MWPC0 X position vs CC scintillator raw position for the scintillator correctly working. Right: Same correlation after the scintillator was damaged. The highlighted region shows the affected zone, causing a non-linear light propagation.*

This will cause two different effects. First one, is a dependence of the mass value obtained with the position of the primary beam, that can be corrected. Second, is a much likelier degradation of the intrinsic resolution of the detector, that can not be exactly computed as there is no primary beam files with the scintillator damaged. In any case, the mass resolution over all the regions will be more than one unit of mass, making impossible to determine with accuracy the mass number in an event-by-event basis.

Mass number distribution

In spite of the loss of mass resolution, if the analysis is correctly performed, the mass distribution for both fission fragments can be obtained. For the study we aim to do in the following chapter, knowing the average mass distributions of both fission fragments should be enough. The main complication derived by the loss of mass resolution lies in how to calibrate the fission fragment mass number.

To perform this calibration, the analysis will be limited to ^{236}U+U reaction, selecting fission events with no proton removal, *i.e.*, the fissioning system $Z_1 + Z_2 = 92$. The reason of this selection is due to the fact that the contribution of coulex fission is mainly dominant. This will allow to use the sum of both fission fragments mass number to perform the calibrations. In other works, the emission of neutrons in coulex-induced fission has been widely studied [111, 112, 113]. The main conclusions extracted are that for these processes, the average loss of neutrons is around 4. As for this system also exists a small contribution of fragmentation fission (around 22 % as will be explained later), our mass sum distribution should start in A=236 and should present a peak around A=231, corresponding to an estimated loss of 5 neutrons, on average.

To perform a correct mass calibration, the trajectory has to be adjusted changing it in small steps of distance. Also, in the highlighted region showed in 2.36 (right), only the zone with more statistics is selected, rejecting the other events. After this selection, the dependence induced by this damage in the mass number can be corrected. Thus, the sum of the fission fragments mass number is shown in figure 2.37. The mass distribution starts in A=236, as expected, with very few events above this value, that can be an effect of the loss of resolution in the mass number identification. Then, the peak of the distribution is centered around A=231, corresponding to an average loss of 5 neutrons. The tail observed below A=225 correspond to fragmentation-induced fission events.

Once the mass number is calibrated, the distribution of masses for fission induced in the uranium and aluminum targets is displayed in figure 2.38, under the condition of $Z_1 + Z_2 = 92$. For fission events induced by the uranium target, the valley in the medium mass region presents fewer statistics than for those produced in the aluminum target. This is due to the fact that fragmentation-induced fission is dominant in the aluminum target, losing more neutrons in the process and shifting the mass distribution to lighter values. The correlation between both fission fragments mass number for the forementioned fission induced reactions is displayed in figure 2.39.

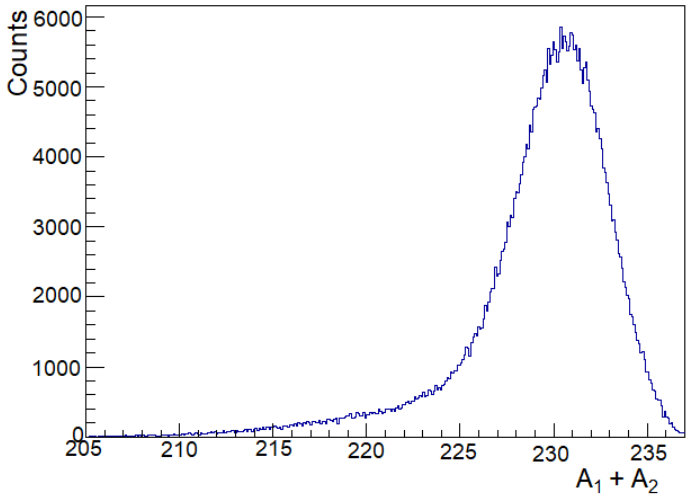

Figure 2.37: *Sum of the fission fragments mass number for* ^{236}U*+U fission reactions under the condition of* $Z_1 + Z_2 = 92$.

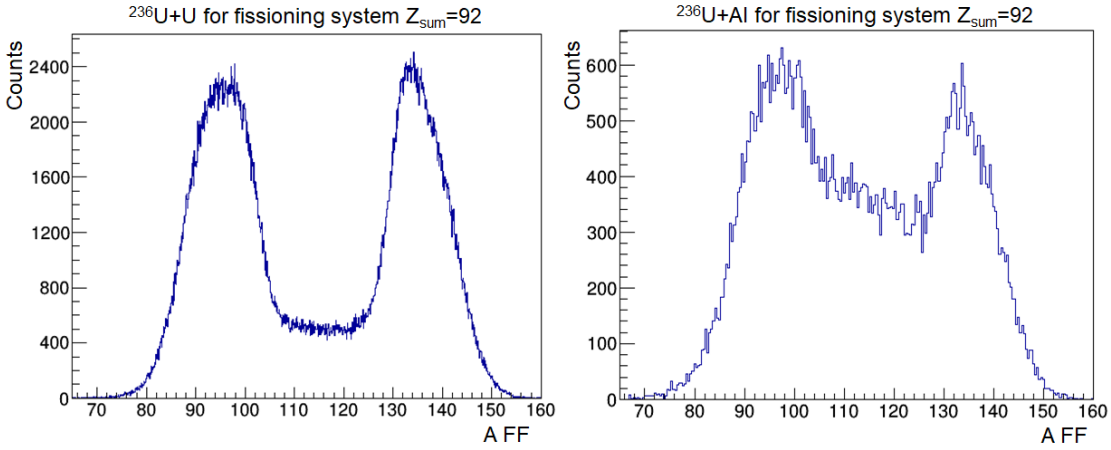

Figure 2.38: *Fission fragments mass distribution for* ^{236}U*+U (left) and for* ^{236}U*+Al (right) fission events, under the condition of* $Z_1 + Z_2 = 92$.

In order to confirm that the mass calibration is correctly done, we aim to compare the mass yield obtained for coulex-induced fission in this work with other published data. Specifically, the work compiled by Crouch [114] contains several mass yields for fission reactions induced with thermal, fast and 14-MeV neutrons. Among all the yields under study, fission yields produced in 14-MeV neutron-induced fission reactions on ^{235}U will serve as

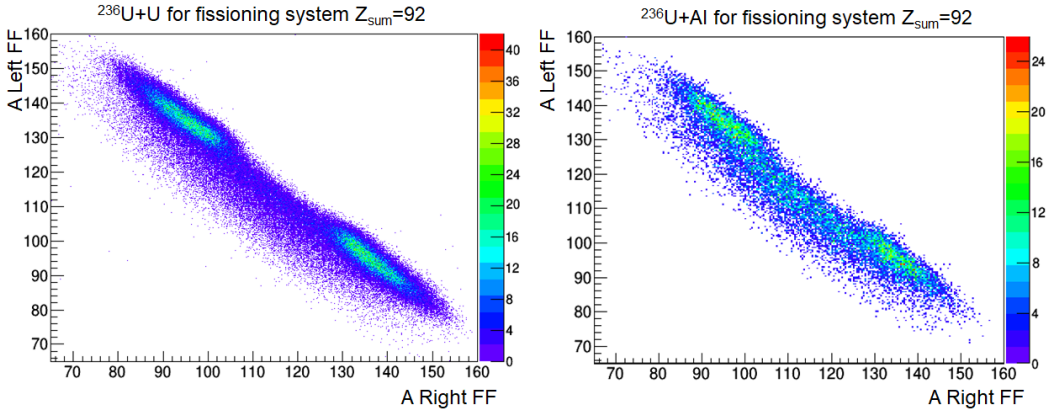

Figure 2.39: *Fission fragments mass correlation for ^{236}U+U (left) and for ^{236}U+Al (right) fission events, under the condition of $Z_1 + Z_2 = 92$.*

a reliable comparison with our data. First, because the compound nucleus formed in this reaction and hence the fissioning system is ^{236}U. Second, the neutron energy selected for this reaction is in the range of the excitation energy for coulex-induced fission achieved in the present experiment.

To compare the mass distribution with the obtained in the present experiment, the fragmentation contribution needs to be removed. For this, the mass sum distributions presented in the ^{236}U+U and ^{236}U+Al induced fission reactions will be adjusted until both match in the tail, corresponding to fragmentation contribution. This is displayed in figure 2.40 (left). The mass sum spectra for fission induced in the aluminum target is multiplied by a factor of 3.04. Thus, the fragmentation contribution results to be around 22% for the fissioning system $Z_{sum} = 92$ in ^{236}U+U fission reactions. In figure 2.40 (right) the mass spectra for both reactions is plotted, normalizing the spectra for fission induced in the aluminum target. The fragmentation contribution is removed by simple subtracting both spectra.

Figure 2.41 shows the mass yields for ^{236}U+U coulex-induced fission compared with the spectra obtained in [114] for 14-MeV neutron-induced fission on ^{235}U. The agreement is satisfactory, being the peaks centered around the same mass value, $A \approx 96$ for the light peak and $A \approx 135$ for the heavier one. Also, the medium mass region covers in both nearly 20 units of mass. The only small difference is found in the medium mass yield, that is slightly lower for the present data. This can be understood in terms of the excitation energy gained in coulex-induced fission, which has been estimated to be around 10 to 12 MeV [82].

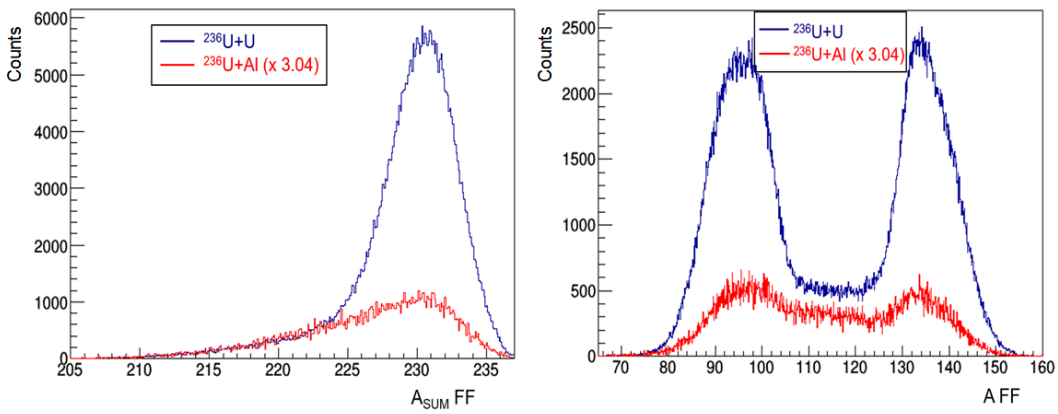

Figure 2.40: *Right: Mass sum spectra for ^{236}U+U (blue) fission reaction and normalized mass sum spectra for ^{236}U+Al (red) to match and subtract fragmentation fission contribution. Left: Mass spectra for the forementioned reactions.*

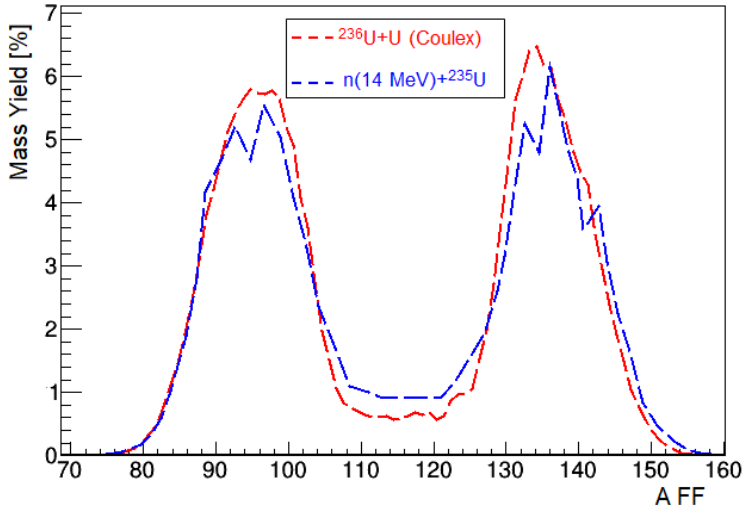

Figure 2.41: *Mass yield for ^{236}U+U coulex-induced fission (red) compared with the obtained in reference [114] for 14-MeV neutron-induced fission reactions on ^{235}U (blue).*

Finally, the mass distributions obtained in the present experiment for fission induced in the uranium and aluminum targets are displayed in figure 2.42. All the fissioning systems are included, so mass distributions are shifted

to lighter values as expected due to the loss of protons for $Z_{sum} < 92$ fissioning systems. The correlation between the masses of both fission fragments are shown in figure 2.43 and 2.44.

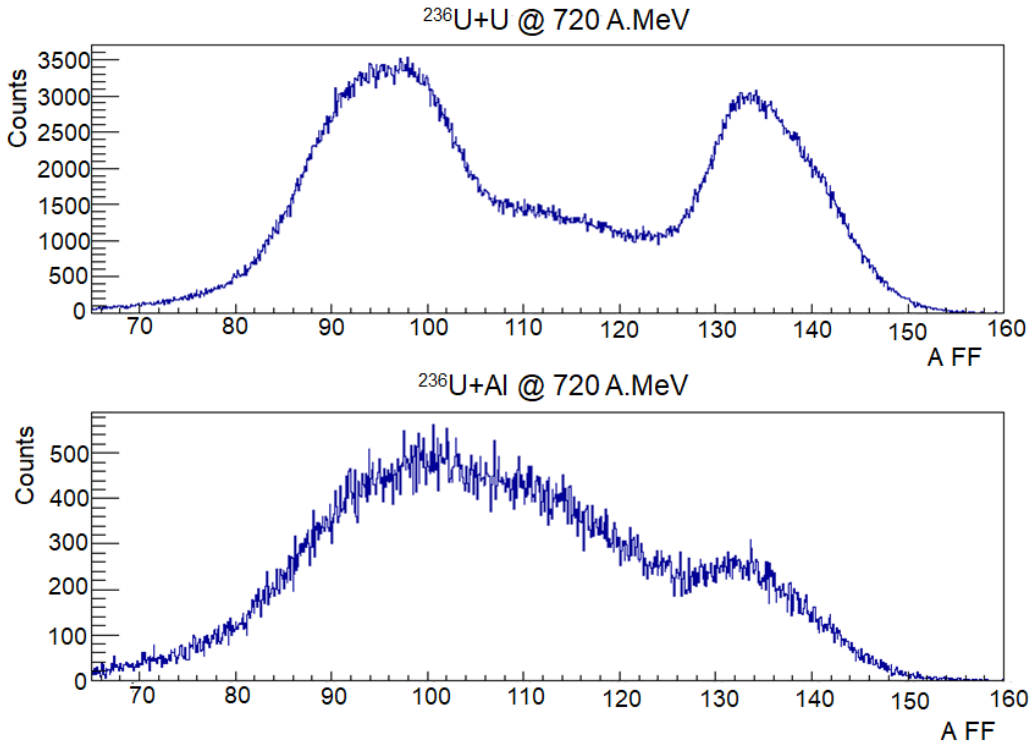

Figure 2.42: *Mass number of the fission fragments for ^{236}U+U (upper pannel) and for ^{236}U+Al reactions (lower pannel).*

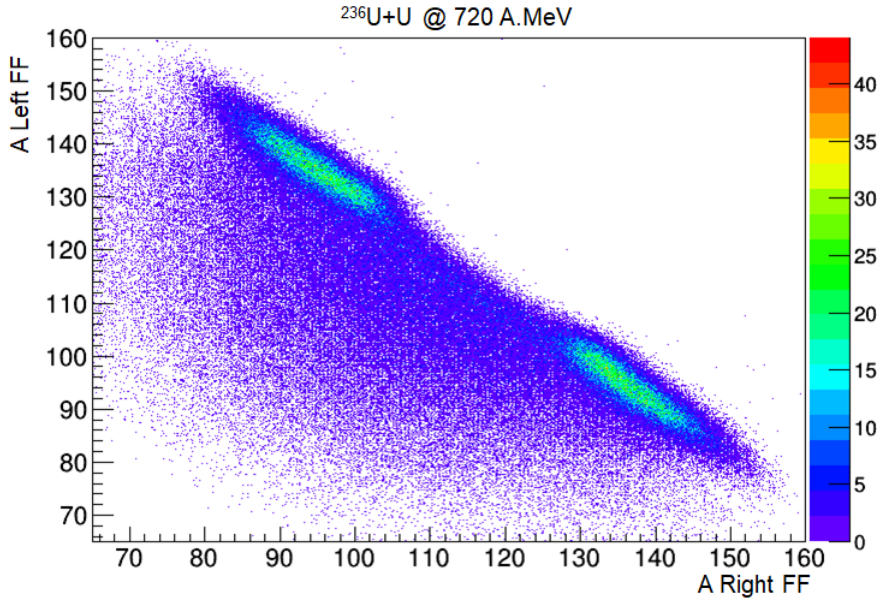

Figure 2.43: *Scatter plot of both fission fragments mass number produced in* ^{236}U*+U reaction.*

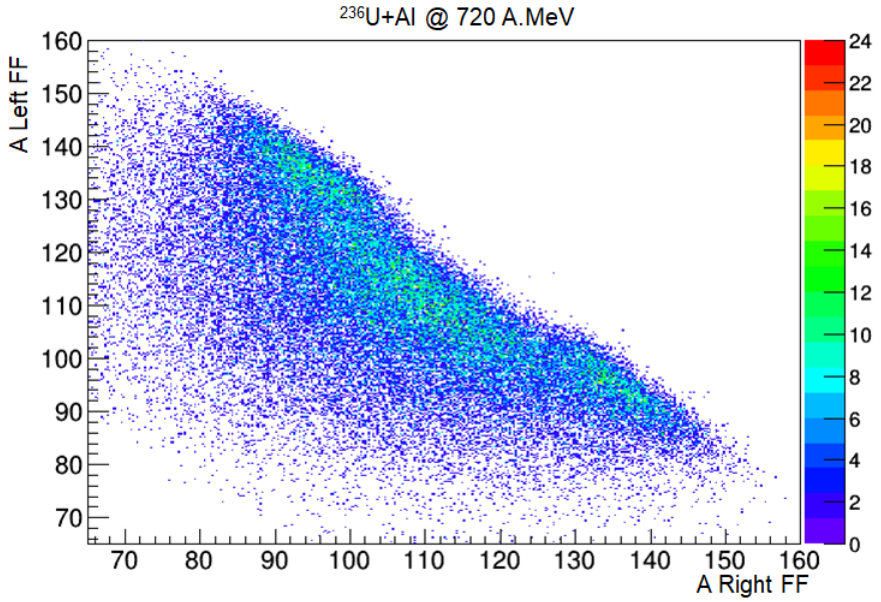

Figure 2.44: *Scatter plot of both fission fragments mass number produced in* ^{236}U*+Al reaction.*

USC
UNIVERSIDADE
DE SANTIAGO
DE COMPOSTELA

Chapter 3

Results on the investigation of the fission dynamics

This third chapter is dedicated to study the fission dynamics from the initial state of the fissioning nuclei to the saddle point and from saddle to the scission configuration. Different experimental observables will be obtained and carefully analyzed for fission reactions induced in the uranium and aluminum target. These results will be compared with other experimental data and with different model calculations to study the fission dynamics at high excitation energy. The dependence of the dissipation parameter with deformation will be explored as well as the influence of the level densities or the angular momentum gained by the fissioning system on the description of the fission process.

3.1 Presaddle dynamics

The first stage of the fission process includes the transition from the initial state of the compound nucleus to the saddle point. As discussed in chapter 1, different experimental observables have been proposed to investigate the dynamics of the fission process at small deformations, such as the partial fission cross sections or the width of the fission fragments atomic number distribution. In this work, we will use ^{236}U fission reactions induced in uranium and aluminum targets at 720A MeV to study these observables. The experimental data will be compared for both fission reactions, in order to see how dependent are with the entrance channel, as well as with other existing data. Then, the data will be used to investigate fission dynamics using model calculations. Specifically, we aim to study the dissipation parameter more suitable to describe the data. Furthermore, we will investigate the influence

of other critical parameters in the description of the fission process, such as the angular momentum gained by the fissioning system and the level densities of the deformed nuclei.

3.1.1 Partial fission yields

Fission partial cross sections as a function of the sum of the atomic number of both fission fragments, $Z_1 + Z_2$, are one of the most interesting observables to study fission dynamics in the presaddle stage [30, 115, 116]. In this work, the partial fission yields are obtained dividing the number of measured fissions for each $Z_1 + Z_2$ system to the total number of fissions, correcting both values for the efficiency of the setup. The sum of the atomic numbers of both fission fragments corresponds to the atomic number of the fissioning system at saddle point, considering that the probability of evaporating protons beyond the saddle point is much lower than the probability of neutron evaporation. This is justified due to the fact that fission fragments are neutron-rich and the main deexcitation channel will be neutron emission. In figure 3.1, the partial fission yields for ^{236}U+U (left) and ^{236}U+Al (right) fission reactions are displayed as a function of $Z_1 + Z_2$. Experimental uncertainties are determined and can be observed when they exceed the size of the marker. A disclaimer should be done here, as in this experiment it was not possible to measure the total fission cross sections, due to the fact that the only trigger used to collect the data was trigger fission, so no beam events passing through the target without reacting were triggered.

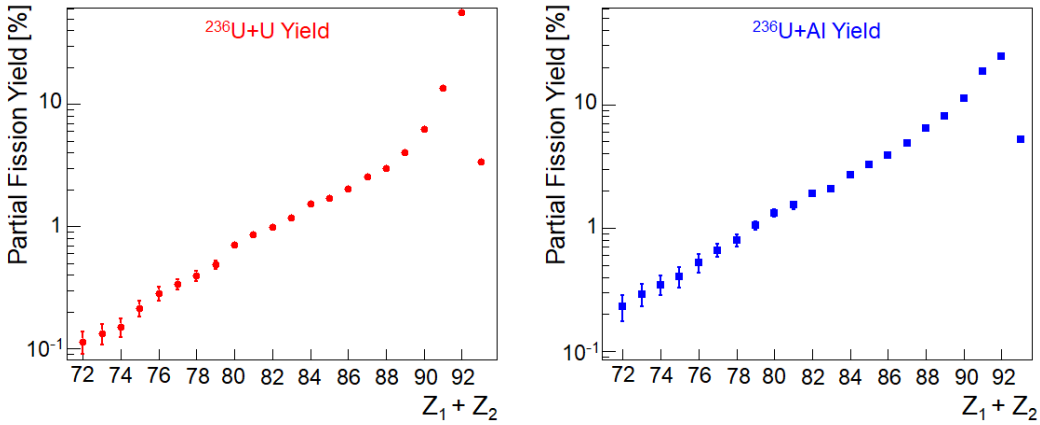

Figure 3.1: *Partial fission yields for ^{236}U+U (left) and for ^{236}U+Al (right) as a function of $Z_1 + Z_2$. Error bars are displayed if they exceed the size of the marker.*

For fission induced in the uranium target, the yield obtained for $Z_1+Z_2 =$

92 is dominant meaning a high contribution of coulex-induced fission. In this kind of reactions, the interaction between the projectile and target nuclei is mostly produced through Coulomb interaction. As there is no contact between both nuclei, protons are not knocked out from the projectile and the excitation energy is too low to evaporate them. For fissions in the aluminum target, we also see that the highest yield corresponds to fissioning system $Z_1 + Z_2 = 92$ but is significantly lower than the obtained for the uranium target, as in fissions in the aluminum target the Coulombian field is less intense. As expected, the partial yields decrease for lighter fissioning systems, due to the fact that fission barriers become higher when more protons are removed and more excitation energy is needed to induce fission. Events with $Z_1 + Z_2 = 93$ correspond to projectiles that underwent fission after charge-exchange reactions [117]. This kind of reactions are produced by the exchange of a virtual pion between colliding nucleons or by the excitation of a nucleon resonance decaying by pion emission.

In order to compare the yields for both reactions, the dominant coulex contribution should be subtracted for fissions in the uranium target. In section 2.5.6, we found that coulex-induced fission represents a 78 % to the $Z_1 + Z_2 = 92$ yield (see figure 2.40). There is also a small contribution of coulex-induced fission for fissioning system $Z_1 + Z_2 = 91$, that can be measured as well, being of 19 %. Thus, fission yields measured with the uranium target can be corrected obtaining the fragmentation-induced fission yields for ^{236}U+U reaction. In figure 3.2, partial fission yields for both reactions are compared. It should be noticed that there is a small coulex contribution for $Z_1 + Z_2 = 92$ fissions induced in the aluminum target, that in this case can not be subtracted. However, it is observed a very good agreement between partial fission yields, including for $Z_1 + Z_2 = 92$, overlapping the values obtained within the error bars. This can suggest that the partial fission yields do not depend on the target material where the reaction is induced.

Finally, the partial fission yields obtained in this work are compared to other published data for different reactions induced by uranium projectiles. In the work done by Jurado and collaborators [30], total and partial fission cross sections have been measured for the reaction ^{238}U+CH_2 at 1A GeV. Dividing each partial cross section by the total fission cross section, partial yields for each fissioning system are obtained and compared with the present data in figure 3.3. It is observed that ^{238}U and ^{236}U data are in very good agreement for fissioning systems $Z_1 + Z_2 < 83$. These fissioning systems are most likely produced in the interaction with the carbon nuclei of the CH_2 target. These nuclei have a larger nuclear radius than the hydrogen.

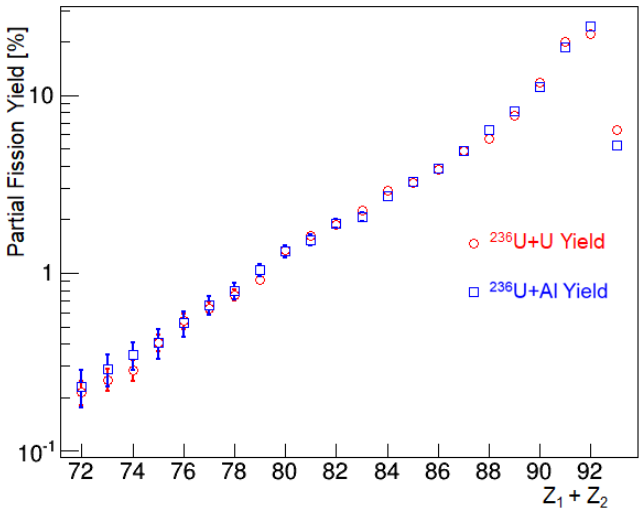

Figure 3.2: *Partial fission yields for ^{236}U+U (red circles) and for ^{236}U+Al (blue squares) as a function of $Z_1 + Z_2$. Error bars are displayed if they exceed the size of the marker.*

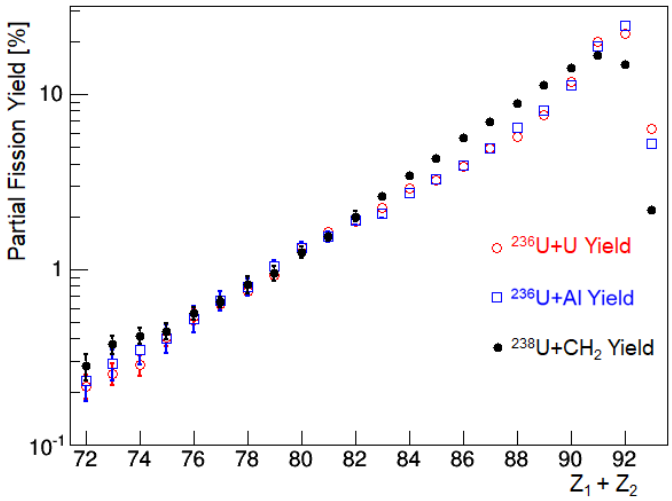

Figure 3.3: *Partial fission yields as a function of $Z_1 + Z_2$ obtained in this work for ^{236}U +U (red circles) and for ^{236}U +Al (blue squares) at 720A MeV compared with those obtained for ^{238}U+CH_2 fission reactions at 1A GeV (black dots).*

The excitation energy acquired in the collision with carbon nuclei allows to evaporate more protons from the projectile, reaching these lighter systems. For heavier fissioning systems, a systematic discrepancy is found that can be

mainly explained as a contribution of the hydrogen in the CH_2 target used to induce fission, varying the production of these fissioning systems. Thus, for heavier fissioning systems, both contributions are present. Anyhow, the tendency observed on both data are similar, and the values of the partial yields are in good agreement for light $Z_1 + Z_2$ systems.

3.1.2 Width of the fission fragments Z distribution

The second observable under study is the standard deviation of the fission fragments atomic number distributions (σ_Z) determined as a function of the sum of the atomic numbers of the final fragments. As explained in section 1.3.2, this observable is strongly correlated with the excitation energy of the system at saddle point. From equation 1.17 one can observe the dependence of the width of the atomic number distribution of the fission fragments with the saddle point temperature, making it suitable to study presaddle effects [31, 63, 64].

The width of the fission fragments atomic number distribution is obtained fitting the correspondent distribution for each fissioning system after the efficiency correction. In figure 3.4, the atomic number distributions for fissioning systems $Z_1+Z_2 = 89$ and $Z_1+Z_2 = 81$ for ^{236}U+U fission reactions are displayed as example. Both spectra are normalized to the same number of events. It can be observed that the mean value of the distribution decreases for lighter fissioning systems. On the contrary, the width of the distribution increases with decreasing $Z_1 + Z_2$.

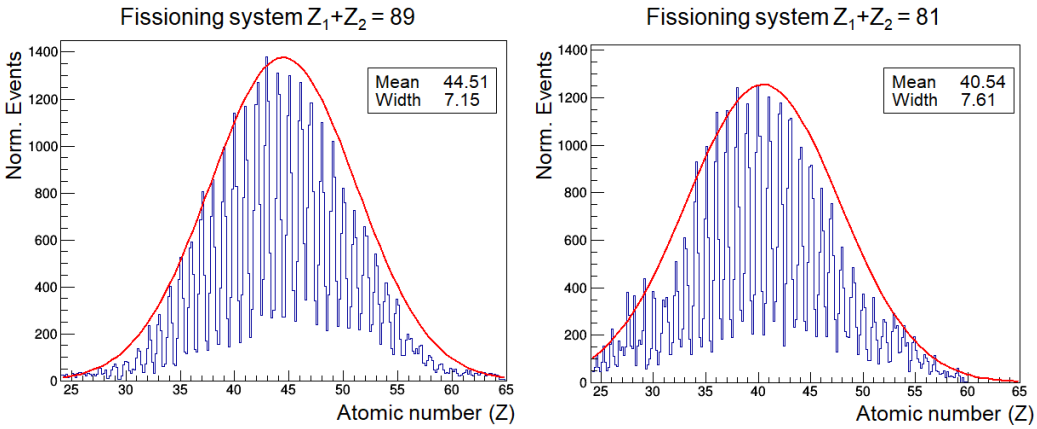

Figure 3.4: *Normalized charge distribution of the fission fragments produced for systems $Z_1+Z_2 = 89$ and $Z_1+Z_2 = 81$ in reactions induced in the uranium target.*

The width of the fission fragments Z distribution obtained in this work are represented in figure 3.5, for fission reactions induced in the uranium and aluminum targets. The fissioning systems taken into account are those that differ at least by two units of charge with respect to the projectile, in order to avoid asymmetric charge distributions due to coulex-induced fission. As stated, these values increase for lighter fissioning systems. This behaviour is expected since lighter fissioning systems present higher temperatures (excitation energy) at saddle point. Moreover, other interesting conclusion is that the width of the atomic number distributions for both reactions under study are very similar for all fissioning systems. This result indicates that the acquired excitation energy is similar in fission induced in both targets, something that was also observed in the partial fission yields. The explanation can be found in terms of the limiting fragmentation concept [118]. This hypothesis states that at high enough energies of the projectile, above 400A MeV [119], the fragmentation reaction products are independent of the target where the reaction is induced, for nuclei heavier than hydrogen [120].

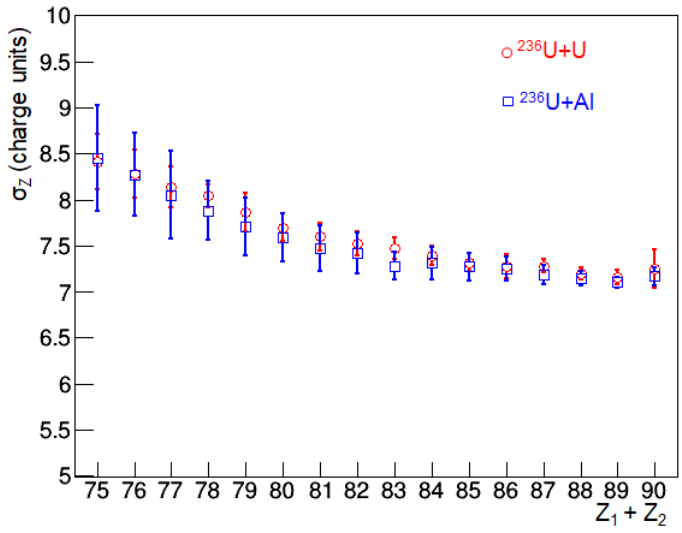

Figure 3.5: *Standard deviation of the fission fragments atomic number distribution for ^{236}U+U (red circles) and for ^{236}U+Al (blue squares) fission reactions as a function of the sum of the atomic numbers of the fission fragments. Error bars are shown if they exceed the size of the marker.*

The results obtained in this work can be benchmarked again comparing them with other existing data for different fission reactions induced with uranium projectiles. In the work done by Schmitt and collaborators [31], the

width of the Z distributions of the fission fragments for several nuclei has been studied. They found that for projectiles with the same atomic number, the width of the atomic number distribution as a function of the fissioning system, $Z_1 + Z_2$, has not a strong dependence with the neutron number of the projectile, specially for heavier $Z_1 + Z_2$ systems. For lighter fissioning systems, the excitation energy increases, finding small differences of around 0.2-0.5 units of charge depending on the number of neutrons of the projectile.

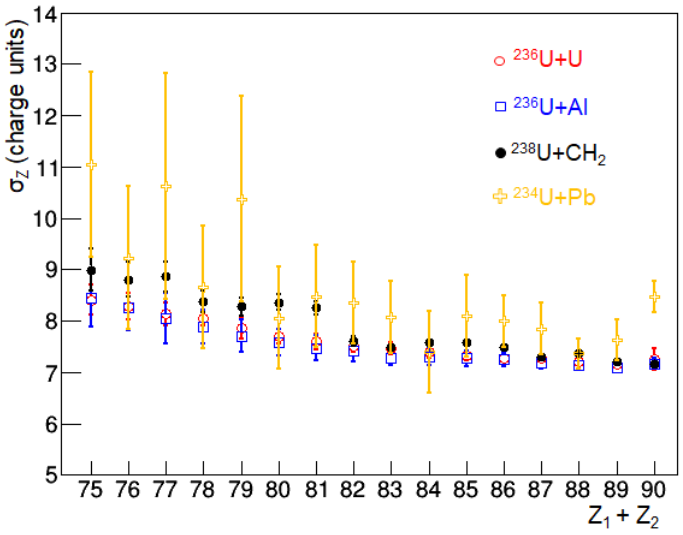

Figure 3.6: *Standard deviation of the fission fragments atomic number distribution obtained in this work for ^{236}U +U (red circles) and for ^{236}U +Al (blue squares) compared with existing data such as ^{238}U+CH_2 (black dots) and ^{234}U +Pb (yellow crosses), as a function of $Z_1 + Z_2$.*

In figure 3.6 we depict the width of the atomic number distribution of the fragments for fission induced by ^{238}U in a CH_2 target at 1A GeV [30] and for ^{234}U in a Pb target at 420A MeV [31] compared with our data, where experimental uncertainties are also included. Even though fission is induced in different targets, no relevant differences with the target is found in this work neither in others [69, 115]. For systems between $Z_1 + Z_2$=90 and $Z_1 + Z_2$=82, it is observed a very good agreement between different data within the error bars. We found more discrepancies for lighter systems. Measurements with ^{238}U present higher values than the obtained in this work, but they stay in the range of variations of 0.2-0.5 units of charge found in [31]. Bigger discrepancies are observed for ^{234}U nucleus. We found a systematic increase of the width of the fission fragments Z distributions for this nucleus,

but these results show larger uncertainties, probably due to smaller statistics. In fact, we can find a reasonably good agreement between ^{234}U and the rest of the data within the error bars. Thus, only light differences are observed between the different uranium projectiles, that could be explained in terms of small variations in the excitation energies achieved by each $Z_1 + Z_2$ fissioning system for the different reactions or due to statistical or systematic errors in the measurements. This lead us to conclude that there is not a sizeable dependence of this observable with the neutron number of the uranium isotope.

3.1.3 Description of the reaction models

The sensitivity to fission dynamics of the previously analyzed observables has been matter of discussion in section 1.3. In fission induced by nuclear fragmentation, the average range of excitation energy acquired by the fissioning system is found to be above 100 MeV. In this range, the behaviour of the fission process can not be explained just in terms of statistical approaches [5]. The model calculations used to interpret the measured observables have to take into account dynamical features through the introduction of dissipative and transient effects.

The collision between the projectile and target nuclei can be described as a fragmentation reaction through a two step process [121]: the collision itself, where part of the nucleons are removed from the projectile and target, leading to the formation of a compound nucleus with some excitation energy and angular momentum, and the subsequent deexcitation processes by evaporation of nucleons or fission. The collision stage can be described using macroscopic approaches like the Glauber model [122] or dynamical models that combine macroscopic and microscopic ingredients. Therefore, we will use the abrasion model developed by J. Gaimard and K.H. Schmidt [80] as well as the dynamical intra-nuclear cascade model developed by D. Mancusi and collaborators [78, 79]. Both models are coupled to the deexcitation model ABLA07 [123].

In previous works, these models have been employed to reproduce experimental data of spallation- and fragmentation-induced fission reactions. Rodriguez et al [70] made use of the intra-nuclear cascade model coupled to ABLA07 to describe the fission observables from the reaction ^{208}Pb+p at 500A MeV, showing great accuracy. Other works employed the abrasion model coupled to ABLA07, the so-called ABRABLA model, to study the fission dynamics in nuclear fragmentation-induced fission reactions [30, 31]. In this work, we aim to use both models in order to find which is the most

suitable to describe our experimental data. In the following, we will briefly describe these models.

Abrasion model

The abrasion model [80] is widely used to describe the collision between nuclei in fragmentation reactions in terms of the Glauber picture [124], at energies well above the Fermi energy. Under this assumption, the total interaction cross sections are calculated using the Karol approximation [125]. The number of removed nucleons after the collision is determined by geometrical integration over the volume of the overlapping zone between the projectile and the target nuclei (participants), while the nucleons in the non-overlapping region (spectators) are barely disturbed by the abrasion. For a specific mass loss, the N/Z distribution of the prefragment is calculated according to the hypergeometrical model [126], where every removed nucleon has a statistical chance to be a neutron or a proton. Thus, the average N/Z ratio of the remaining nucleus corresponds to the one of the initial nucleus, although with large statistical fluctuations, which lead to large variations in the N/Z ratio of the reaction products. Assuming the Fermi-gas model, the nucleons occupying the overlap volume of the colliding nuclei are randomly distributed in momentum space inside the Fermi spheres of the projectile and target nuclei. These nucleons, when removed during the collision, leave holes in the Fermi sea. Each hole is associated with a certain energy obtained according to the single particle-hole picture. Using the Fermi-gas distribution of the single-particle levels, the gained excitation energy is described by a linear distribution between 0 and 40 MeV, providing an average excitation energy of 13.5 MeV per removed nucleon. In this approximation, shell effects are neglected and the nucleon-separation energies are isospin independent, assuming a constant value for all nuclei. The internal energy of the single holes is then redistributed among all the degrees of freedom of the remaining nucleus, which thermalizes and forms a compound nucleus. The total excitation energy gained by the remnant is given by the sum of the single particle-hole excitations, being proportional to the number of removed nucleons and the depth of the hole created inside the nucleus potential. Similarly, the angular momentum distribution is defined by the angular momenta of the nucleons removed [127], given in analogy to Goldhaber statistical approach [106]. The abrasion process produces a gaussian momentum distribution calculated in terms of the mass number of the prefragment and the initial projectile, which reflects the Fermi motion of the nucleons inside the nucleus.

Intra-nuclear cascade model INCL

The dynamical intra-nuclear cascade model INCL is extensively used for the description of spallation-induced reactions at high energies [78, 79]. The model consists of a Monte-Carlo method to solve the transport equations governing the time evolution of a system of nucleons inside a nucleus after the collision, taking into account all the possible interactions with each other. In this context it is assumed that the first stage of the reaction can be described as an avalanche of independent binary collisions well separated in space and time. Particles travel along straightline trajectories until two of them reach their minimum distance of approach or until they hit the border of the potential well describing the nuclear target mean field. The INCL model is essentially classical, with the addition of a few suitable ingredients that mimic genuine quantum-mechanical features of the initial conditions and of the dynamics. Here, one must note that projectile and target nuclei are treated in different ways. Assuming reactions in inverse kinematics, the projectile nucleus is represented by a potential well according to Woods-Saxon distribution. The potential well depth for nucleons is calculated according to optical models, including isospin dependences [128], while radii and diffuseness parameters of the proton and neutron density profiles are taken from Hartree-Fock-Bogoliubov calculations [129]. Regarding the target nuclei, limited up to A=18, the nucleon momenta are described with a Gaussian distribution considering the same rms momentum (3/5 p_F) for protons and neutrons, with p_F = 270 MeV/c. For the dynamical description of the collision between the projectile and target nuclei, each event is fired at a given impact parameter b, ranging from 0 to a distance b_{max} given by the sum of the maximum radius of projectile and target nuclei. If two hadrons approach each other at a distance lower than a minimum distance, they interact. During the cascade process, the particles inside the projectile volume are divided into participants and spectators. Participants are defined as particles that have collided with at least one other participant, while spectators are the rest of particles. Collisions between spectators are forbidden. For the subsequent collisions, INCL applies the Pauli principle according to the usual procedures by means of statistical blocking factors. In addition, a consistent dynamical Pauli blocking is applied to all particles at the end of the cascade process to reject unphysical results, see Ref. [78] for more details. Thus, at the end of the cascade process, the angular momentum and the excitation energy induced in the system is determined by particle-hole excitation and holes produced in the initial Fermi distribution of the target.

Deexcitation model ABLA07

After the collision, the characteristics of the prefragment, namely its angular momentum, charge, mass and excitation energy, are defined. The subsequent deexcitation undergone by this nucleus, that is at thermal equilibrium, is described using the ABLA07 code [123]. ABLA07 is a statistical code that describes the deexcitation of the compound system by particle emission and fission. Before the deexcitation stage, a simultaneous break-up describing the cracking of the hot nucleus into several fragments due to thermal instabilities can also occur depending on the temperature of the compound system [130, 131]. The emission of neutrons, light charged particles (Z=1,2), γ rays and intermediate-mass fragments (IMFs) is described according to Weisskopf formalism [132]. In order to obtain the particle decay widths in a more realistic way, the separation energies and the emission barriers for charged particles are included according to the atomic mass evaluation from [133] and the Bass potential [134], respectively. The change of the angular momentum due to particle emission is also considered.

In addition, deexcitation by fission is also included according to the dynamical picture provided in section 1.2.3. The fission decay width is described from the analytical time-dependent approach given by Jurado [50], represented in equation 1.7. The influence of the initial deformation on the fission decay width is also taken into account. The emission of particles on different stages of the fission process, from ground to saddle and from saddle to scission, is calculated separately.

A consistent treatment of fission barriers and level densities is of utmost importance to correctly describe the decay width of the fission channel. In section 1.2.1, the level density at saddle point is calculated on the basis of the Fermi gas model (equation 1.3). The physical considerations behind this treatment involved only the intrinsic nuclear degrees of freedom. However, for a most precise determination of this parameter, one need to account not just single particle considerations, but also the interaction between nucleons because of their motion inside the excited nuclei. This translates to the existence of collective excitations such as rotations and/or vibrations, in analogy with molecular physics [135, 136]. Thus, the level density can be rewritten taking into account both intrinsic and collective degrees of freedom, as:

$$\rho(E) = \rho_{int}(E) \cdot K_{coll}(E) \tag{3.1}$$

being ρ_{int} the level density of the internal excitations (obtained in equation

1.3) and K_{coll} is the enhancement factor due to contribution of collective effects. In deformed nuclei, the most important contribution to this term originates from the appearance of rotational bands, while in spherical nuclei the collective enhancement is caused by vibrational excitations. In the case of fission, rotations also affect to the deformation at saddle point and vibrations to the initial state of the system. This term can be calculated following the description in [135]. For quadrupole deformations $|\beta_2| > 0.15$, the rotational modes are dominant, thus the K_{coll} factor is calculated in terms of the spin-cutoff parameter ($\sigma_\perp$), which is dependent of the rigid-body perpendicular moment of inertia and the nuclear temperature:

$$K_{coll} = \begin{cases} (\sigma_\perp^2 - 1) \cdot f(E) + 1 & \text{for } \sigma_\perp^2 > 1, \\ 1 & \text{for } \sigma_\perp^2 < 1. \end{cases} \tag{3.2}$$

the parameter *f(E)* is a Fermi function used for describing the damping of the collective modes with increasing excitation energy. It can be expressed, in terms of a critical energy and a width parameter. In the case of lower quadrupole deformations ($|\beta_2| < 0.15$), the vibrational excitations should also be taken into account in order to simulate the vibrational motion. This can be simply done by modifying the spin-cutoff parameter.

Model features

In order to investigate the dynamical features of fission, one needs a code providing the most accurate possible description of the remnants produced in the nucleus-nucleus interaction. ABRABLA allows to calculate all kind of reactions for heavy ions at relativistic energies in inverse kinematics. In INCL, the reactions are calculated using targets with a mass number up to A=18. As seen in previous sections, no relevant discrepancies were found with the mass number of the target for the analyzed observables. Thus, the calculations will be done using the reaction ^{236}U+^{27}Al in ABRABLA and ^{236}U+^{16}O in INCL.

The angular momentum, excitation energy and mass number of the emitted prefragments calculated by both codes will be discussed and compared. In figure 3.7, the angular momentum calculated by both codes is displayed as a function of the atomic number of the prefragment. One can observe a big discrepancy between both values. While the angular momentum acquired by the prefragment from ABRABLA is around 5 to 15 $\hbar$, INCL provides a value 6 to 7 times larger, reaching almost 100 $\hbar$ for lighter systems. The value of the angular momentum will affect to the height of the fission barrier [44, 137], changing the probability of fission.

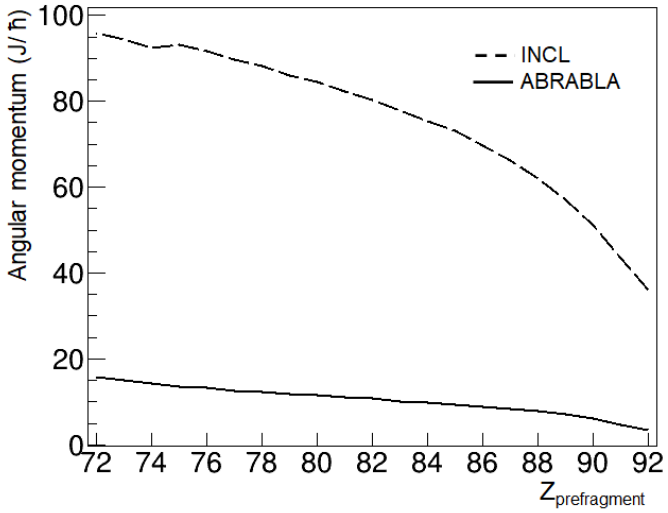

Figure 3.7: *Angular momentum of the prefragment calculated with ABRABLA (full line) and INCL (dashed line).*

Regarding the excitation energy of the prefragment, figure 3.8 shows a very similar value of this quantity calculated by both codes. Only small differences are found for lighter systems, where the excitation energy given by INCL is 10% higher with respect to ABRABLA. Finally, the mass number of the emitted prefragment after the collision is shown as a function of its atomic number in figure 3.9. For lighter atomic numbers, the mass of the prefragments calculated by INCL is, on average, 3 to 6 units smaller. These light differences can be explained in terms of the collision products. INCL is able to calculate excitations of baryonic resonances that decay emitting one pion and one nucleon. These pions can interact with the prefragment removing more neutrons and/or protons, resulting in the formation of prefragments with higher excitation energies [138].

Other important feature is the excitation energy of the compound system at saddle point. After the prefragment is formed, it evolves up to the saddle point evaporating particles, mainly protons and neutrons, losing part of its initial excitation energy during this process. Thus, the excitation energy at saddle point is calculated with the deexcitation code ABLA07. The width of the atomic number distribution is directly related to this parameter, as has been previously discussed in section 1.3.2 (see equation 1.17), so a correct description of the excitation energy at saddle point will allow to compare our data with model calculations. In figure 3.10, the excitation energy at saddle point is represented as a function of the atomic number of the prefragment for different calculations.

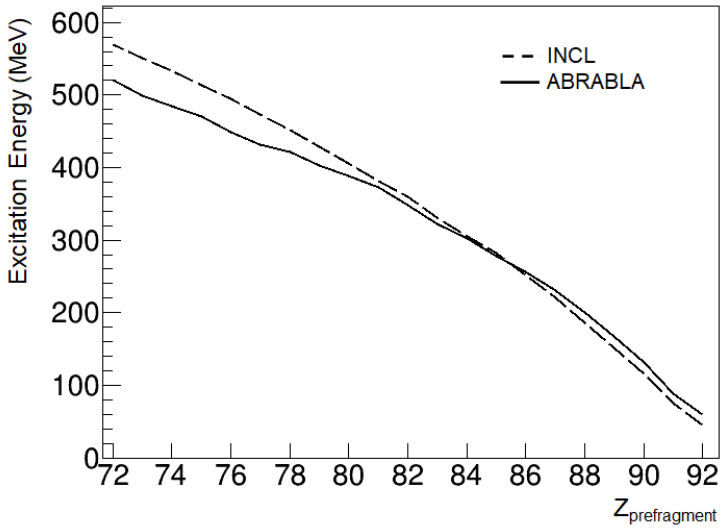

Figure 3.8: *Excitation energy gained by the prefragment calculated with ABRABLA (full line) and INCL (dashed line).*

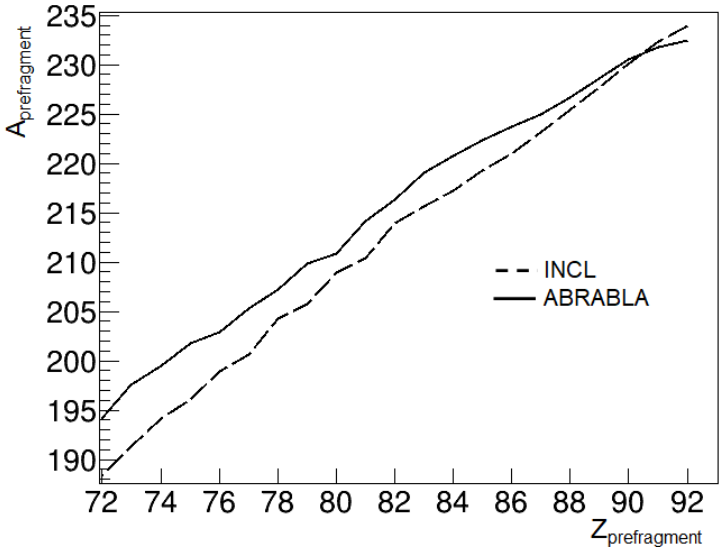

Figure 3.9: *Mass number of the prefragment calculated with ABRABLA (full line) and INCL (dashed line).*

The full black line corresponds to the standard ABRABLA calculation, while the dashed black line shows a calculation performed without taking into account the collective effects in the level densities calculation (equations

3.1 and 3.2). The full red line is obtained multiplying the angular momentum given by ABRABLA by a factor of 6, similar to the value given by INCL. In principle, one should expect that the excitation energy at saddle increases with decreasing $Z_1 + Z_2$, similar to the excitation energy of the prefragments displayed in figure 3.8, something that is only reproduced without collective effects or multiplying the angular momentum of the system by a factor of 6. In the standard ABRABLA calculation a reduction of the excitation energy at saddle for lighter fissioning systems is observed. Furthermore, much lower values of the excitation energies at saddle are obtained. This can be expected as collective effects increase the probability of low energy fission, so the mean value of the excitation energy at saddle can decrease, but this effect should not be that relevant. In fact, for lighter fissioning systems, the contribution of low energy fission should be negligible. Thus, the behaviour of this parameter in the standard ABRABLA calculations suggests that it could exist a problem in the description of collective effects to calculate the level densities of the deformed nuclei in the deexcitation code or that the angular momentum of the prefragment is not correctly calculated.

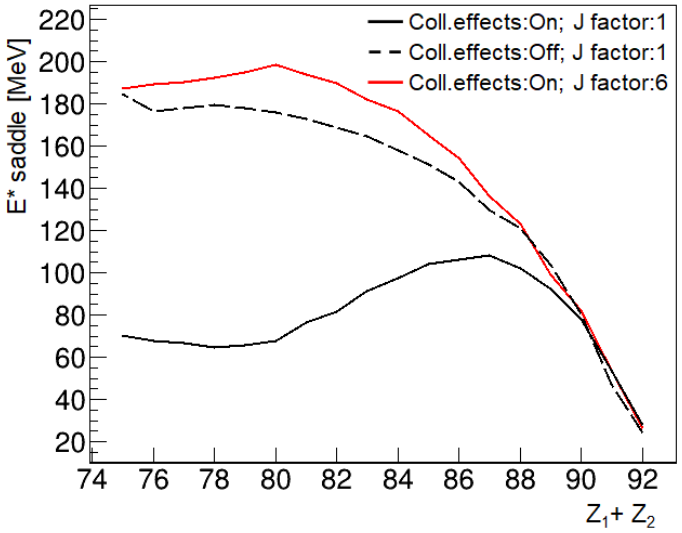

Figure 3.10: *Excitation energy at saddle point for different calculations with the ABRABLA code. Full black line represents the standard calculation, dashed black line has been obtained without collective effects and full red line has been obtained multiplying the angular momentum by a factor of 6.*

3.1.4 Model description of the data

In this section, the experimental data obtained for the partial fission yields and the width of the fission fragments Z distribution as a function of $Z_1 + Z_2$ will be compared with model calculations to study the presaddle fission dynamics. We aim to investigate the sensitivity of these observables to the dissipation parameter β, in order to constrain its value, as well as to the angular momentum and level densities.

In figure 3.11, the partial fission yields as a function of the sum of both fission fragments atomic number for ^{236}U +Al fission induced reactions (blue squares) are compared with INCL and ABRABLA calculations using a presaddle dissipation parameter of $\beta_{gs} = 4.5 \cdot 10^{21} s^{-1}$. Dashed and full red lines represent the results obtained with INCL with and without collective effects, respectively. ABRABLA calculations were also run with (dashed black line) and without collective effects (full black line). As explained in the previous section, the collective effects are included in the calculation of the level densities of the deformed nuclei, taking into account rotations and vibrations of the nuclear constituents (see equations 3.1 and 3.2).

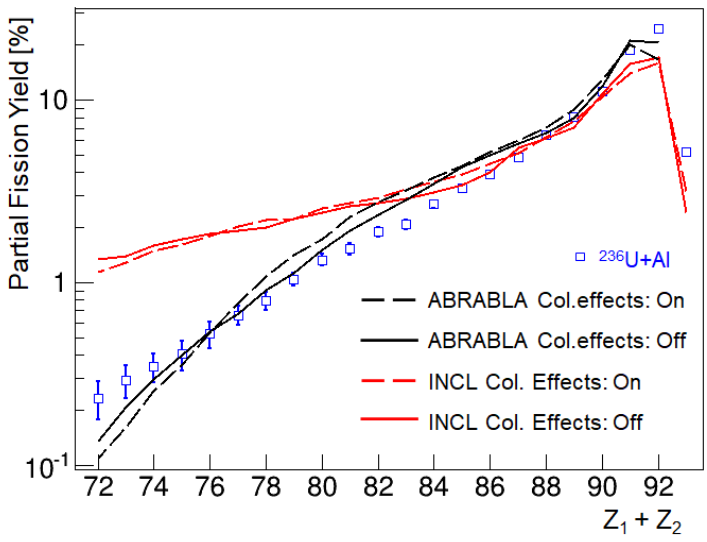

Figure 3.11: *The partial fission yields as a function of the sum of both fission fragments atomic number for the fission reaction ^{236}U +Al (blue squares) are compared with INCL calculations (dashed red line with collective effects and full red line without them) and ABRABLA calculations (dashed black line with collective effects and full black line without them). All the calculations have been run with a presaddle dissipation parameter $\beta_{gs} = 4.5 \cdot 10^{21} s^{-1}$.*

We can observe that INCL calculations clearly overestimate the partial fission yields for lighter fissioning systems. The discrepancies can be explained in terms of the large difference in the angular momentum of the prefragment calculated by both codes, as depicted in figure 3.7, affecting to the fission probability. In ABRABLA, the angular momentum is obtained from the mass number of the projectile and the prefragment using the Goldhaber statistical approach [106]. INCL calculates this quantity as the difference between the initial and final angular momentum of the system. However, the angular momentum in this model is not conserved, because of transmission through the surface and also because the scattering plane is not preserved in binary collisions. Thus, to calculate this quantity more accurately, an elaborate prescription is given in [139]. In this case, the large angular momentum calculated with INCL cause the lighter systems to be able to overcome the fission barrier with much more probability than the data shows, suggesting that is too high. It is worth to mention that other works were able to reproduce the experimental observables with accuracy using INCL on its nucleon-nucleus version, such as the work of Rodriguez and collaborators [70], using ^{208}Pb+p reactions. This lead us to think that the INCL calculations fail in the description of the angular momentum in nucleus-nucleus collisions.

ABRABLA calculations provide a more accurate picture to describe the partial yields for each fissioning system. We can also observe how calculations are hardly affected by the collective effects in the description of the partial fission yields. However, the total fission cross sections are in fact sensitive to the collective effects, obtaining a fission cross section of 0.95 barns without them in opposition to the 1.61 barns obtained when they are considered. The conclusion is that the collective effects increase the probability of fission, as expected, but do not affect to the partial production of each fissioning system.

To further investigate the role of the level densities in the description of the fission process, in figure 3.12, the widths of the fission fragments atomic number distributions as a function of $Z_1 + Z_2$ are compared with two different ABRABLA calculations, with and without collective effects (dashed and full black lines, respectively) using a dissipation parameter of $\beta_{gs} = 4.5 \cdot 10^{21} s^{-1}$. The width of the fission fragments Z distributions are only reproduced when the collective effects are not considered. Taking them into account, the behaviour of the excitation energy at saddle point (see figure 3.10) produces not just an underestimation of the values of this observable, but also a systematic reduction for lighter fissioning systems, which is not reasonable. As the dependence of this observable with the excitation energy

at saddle is $\sigma_Z \propto \sqrt{E_{saddle}}$, a decrease of the excitation energy at saddle would lead to a reduction of the width of the fission fragment Z distribution, something that is not observed in our data neither in other publications (see figure 3.6). In this sense, taking also into account the conclusions extracted for the partial fission yields, the most accurate description is given by ABRABLA without collective effects, suggesting there may be a problem in how the collective effects are parametrized in the calculation of the level densities, in particular on their dependence on the atomic and mass number of the fissioning nucleus.

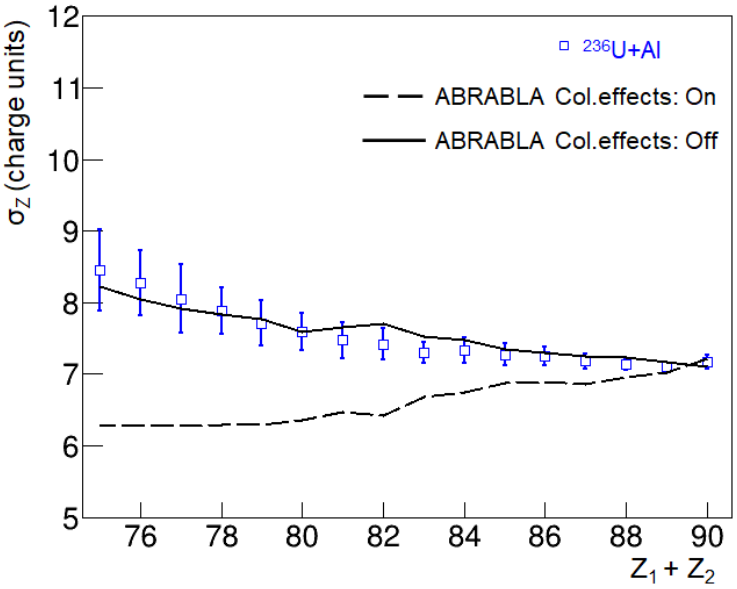

Figure 3.12: *The width of the fission fragments atomic number distribution obtained in this work (blue squares) is compared with two ABRABLA calculations, with (dashed black line) and without collective effects (full black line). Both calculations have been performed with* $\beta_{gs} = 4.5 \cdot 10^{21} s^{-1}$.

Using ABRABLA without collective effects, the sensitivity of the calculations to dissipative effects is now investigated. Figure 3.13 shows the results of these calculations for the partial fission yields as a function of $Z_1 + Z_2$. The first conclusion is that the statistical approach given by Bohr-Wheeler (dashed red line) clearly overestimates the partial yields for lighter fissioning systems. Kramers approach (full red line), that includes dissipation but not transient effects (see section 1.2.2), neither describe the data.

Calculations including time-dependent approaches to describe fission using a dissipation parameter between $\beta_{gs} = 3 \cdot 10^{21} s^{-1}$ (dashed black line) and $\beta_{gs} = 4.5 \cdot 10^{21} s^{-1}$ (full black line) describe more accurately the partial fission yields. This proves that time-dependent approaches are needed in the description of the partial fission yields as a function of the sum of both fission fragments atomic number. Other time-dependent approaches with higher values of the dissipation parameter, such as $\beta_{gs} = 20 \cdot 10^{21} s^{-1}$ (dotted-dashed black line), describe poorly the data for lighter systems, being underestimated. The reason behind this is found in terms of the transient time. A higher value of the dissipation parameter increases the transient time, delaying the probability of fission specially for these lighter systems.

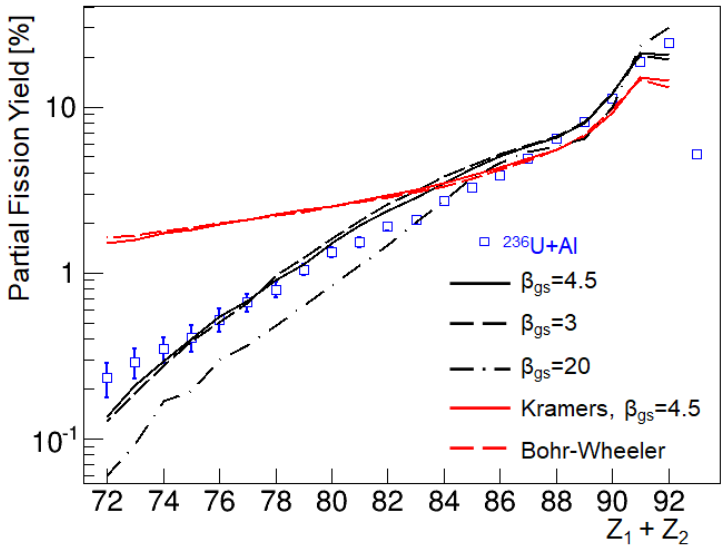

Figure 3.13: *The partial fission yields as a function of the sum of the atomic number of both fission fragments for the fission reaction ^{236}U +Al (blue squares) are compared with different model calculations with ABRABLA. Kramers and Bohr-Wheeler approaches are shown in full and dashed red lines, respectively. Dynamical calculations for different presaddle dissipation parameters are displayed in full black line ($\beta_{gs} = 4.5 \cdot 10^{21} s^{-1}$), dashed black line ($\beta_{gs} = 3 \cdot 10^{21} s^{-1}$) and dashed-dotted black line ($\beta_{gs} = 20 \cdot 10^{21} s^{-1}$).*

In figure 3.14 we show the same calculations for the width of the fission fragments Z distribution as a function of $Z_1 + Z_2$. Red lines describe the time independent approaches, namely Bohr-Wheeler (dashed red line) and Kramers (full red line). These approaches overestimate the experimental data, specially for lighter fissioning systems, by 25-35 %. Calculations

including transient effects are again needed to describe this observable. In particular, the calculations performed with a dissipation parameter of around $\beta_{gs} = 4.5 \cdot 10^{21} s^{-1}$ (full black line) reproduce with accuracy the width of the fission fragments atomic number distribution as a function of $Z_1 + Z_2$, similar to previous works [69, 115, 31]. For a higher value of the dissipation parameter $\beta_{gs} = 20 \cdot 10^{21} s^{-1}$ (dashed-dotted black line) the calculations underestimate the data obtained for this observable.

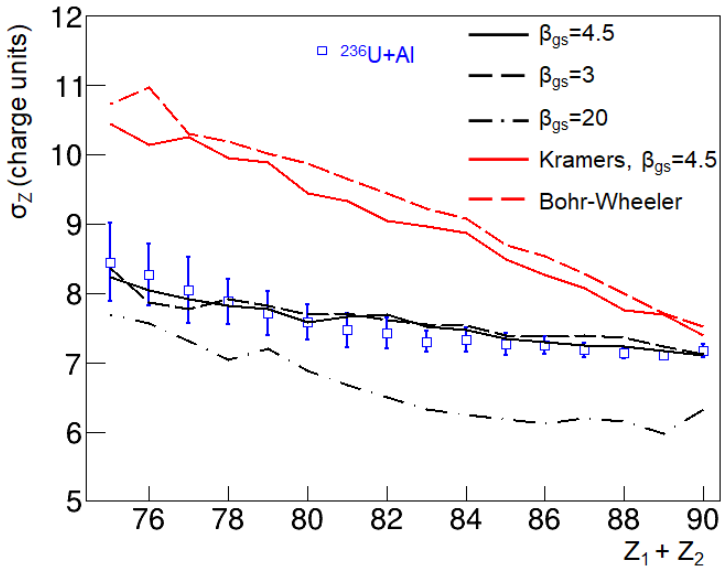

Figure 3.14: *The width of the fission fragments atomic number distribution obtained in this work (blue squares) is compared with different model calculations with ABRABLA. Kramers and Bohr-Wheeler approaches are shown in full and dashed red lines, respectively. Dynamical calculations for different presaddle dissipation parameter are displayed in full black line ($\beta_{gs} = 4.5 \cdot 10^{21} s^{-1}$), dashed black line ($\beta_{gs} = 3 \cdot 10^{21} s^{-1}$) and dashed-dotted black line ($\beta_{gs} = 20 \cdot 10^{21} s^{-1}$).*

In conclusion, in this section we have studied the partial fission yields and the width of the fission fragments Z distribution as a function of $Z_1 + Z_2$ to investigate fission dynamics at the presaddle stage. These observables have shown sensitivity to the angular momentum, the collective effects and the dissipation parameter. Due to the high angular momentum gained by the prefragment after the collision, the calculations performed with INCL are not able to reproduce the partial fission yields. The inclusion of collective effects in the level density calculation affects to the excitation energy at saddle point. To reproduce the standard deviation of the fission fragments Z distributions,

we need a correct behaviour of this excitation energy at saddle, something that is only obtained when collective effects are not considered.

Thus, both observables are only reproduced using ABRABLA without collective effects. In this case, the value of the presaddle dissipation parameter that better describes the data is found to be around $\beta_{gs} = (4.5 \pm 1.0) \cdot 10^{21} s^{-1}$. The uncertainty associated to this value is given since the calculations are not that sensitive to small variations of this parameter. This is in good agreement with the results of different works, namely the work by Rodriguez et al [70] and Ayyad and collaborators [115] using spallation-induced fission reactions and the work performed by Schmitt et al [31] using fragmentation-induced fission reactions. In these works, the calculations and observables analyzed were similar to the ones used in the present work. Ye and collaborators [77] also obtained the same value using fusion-fission reactions. In this case the analyzed observable to study the fission dynamics was the fission cross sections as a function of the excitation energy, while the calculations were performed solving numerically the Langevin equations coupled to the statistical decay model. Thus, the value of this presaddle coefficient is rather well established, obtaining a similar value regarding the observables analyzed or the calculations performed.

3.2 Postsaddle dynamics

To study the fission dynamics from the saddle to the scission point, it is important to find observables sensitive to the dynamical evolution of the system at this stage. Our efforts will be focus in the analysis of the average neutron excess of the fission fragments, proposed as a suitable observable in [69]. This observable is sensitive to neutron evaporation from the ground state configuration to the scission point and also to the excitation energy acquired in the reaction. Constraining the value of the presaddle dissipation parameter, we aim to study the value of the postsaddle coefficient in order to investigate the saddle-to-scission dynamics.

3.2.1 Average neutron excess

Thanks to the complete isotopic identification of both fission fragments, information about mass number can be used to study postsaddle dynamics. The observable we mean to use is the average neutron excess, defined as the average neutron number over the atomic number of the final fission fragments, $<N/Z>$. This observable is again analyzed as a function of the sum of the atomic number of the final fission fragments $Z_1 + Z_2$ for fission reactions

induced in the uranium and aluminum targets. As example, in figure 3.15, the $<N/Z>$ ratio obtained from fission events in the uranium target is plotted for two different systems, $Z_1 + Z_2$=89 (left) and $Z_1 + Z_2$=80 (right). We can observe how the value of this observable decreases with decreasing $Z_1 + Z_2$, as lighter systems are produced in more violent collisions, acquiring higher excitation energies and being able to evaporate more neutrons.

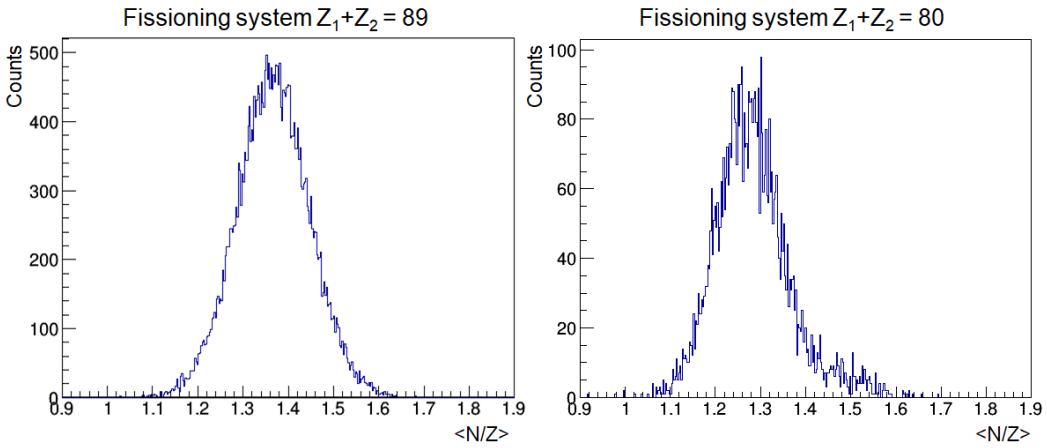

Figure 3.15: *Average $<N/Z>$ ratio obtained from ^{236}U +U fission reactions for two different systems, $Z_1 + Z_2$=89 (left) and $Z_1 + Z_2$=80 (right).*

Therefore, the average $<N/Z>$ ratio for each $Z_1 + Z_2$ can be obtained fitting the correspondent distribution to a gaussian function. However, a correction needs to be applied in order to achieve a more accurate value. From the previous figure, it is observed how the distribution for the lighter system is not completely symmetric, as lower values, correspondent to lighter masses, are cut. This suggests that these events are lost due to the geometrical efficiency of the experimental setup and should be taken into account to correct the distribution and hence the $<N/Z>$ ratio. The correction has been performed simulating the experimental setup in R3BRoot. The $<N/Z>$ of the fission fragments traversing the setup were obtained from simulation and then compared with their initial value. It was found a systematic overestimation of this reconstructed value with respect to the real one of around $(1 \pm 0.05)\%$ for the lightest systems to $(3 \pm 0.2)\%$ for the heaviest ones.

After the above-mentioned correction, the experimental values of the average $<N/Z>$ ratio as a function of $Z_1 + Z_2$ are plotted in figure 3.16 for fissions induced in the uranium (red circles) and the aluminum target (blue

squares). The evolution of this observable behaves as expected, reducing its mean value due to the increasing evaporation of neutrons for lighter systems. The $Z_1 + Z_2$ systems analyzed are those where fragmentation-induced fission is dominant, *ie*, $Z_1 + Z_2 < 92$. A very good agreement between both fission reactions is observed within the error bars. The biggest discrepancy between both reactions is found for the system $Z_1 + Z_2$=91. This is explained in terms of the small coulex-induced fission contribution for fissions in the uranium target. Thus, some of these reactions are more peripheral, gaining less excitation energy, which results in a smaller number of evaporated neutrons. Uncertainties are calculated combining the uncertainty obtained from the gaussian fit and the uncertainty associated to the correction applied.

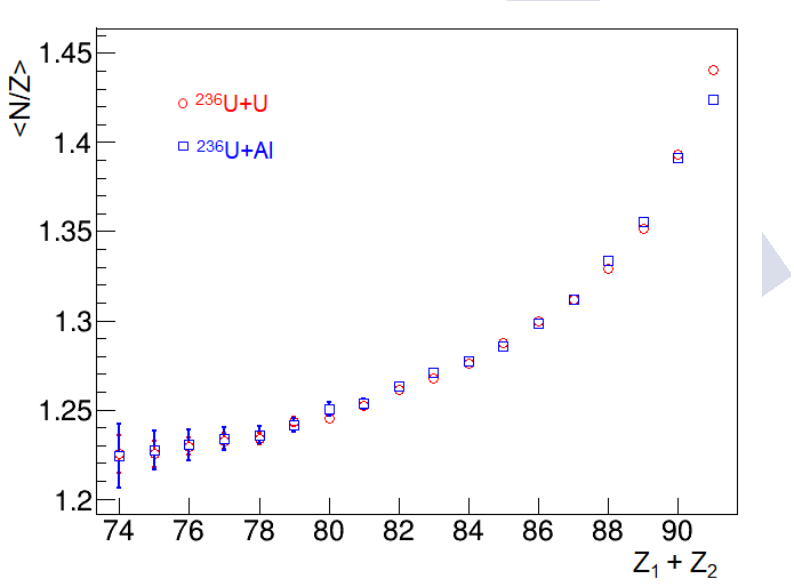

Figure 3.16: *Average neutron excess of the fission fragments as a function of* $Z_1 + Z_2$ *for* $^{236}U + U$ *(red circles) and for* $^{236}U + Al$ *(blue squares) fission induced reactions. Error bars are shown if they exceed the size of the marker.*

3.2.2 Model calculations

We will use as starting point the conclusions extracted from the presaddle dynamics study to run new model calculations. Thus, a presaddle dissipation parameter of $\beta_{gs} = 4.5 \cdot 10^{21} s^{-1}$ will be used in all the calculations, varying the postsaddle dissipation parameter, β_{ss}. In order to be consistent, these calculations have been run using ABRABLA without collective effects, as it

was the configuration that showed the best agreement to describe presaddle observables. It is worth to say that no significant differences between INCL and ABRABLA, with and without collective effects, were found in the description of this observable, as depicted in figure 3.17, where the same value for the dissipation parameter pre- and postsaddle, $\beta_{gs} = \beta_{ss} = 4.5 \cdot 10^{21} s^{-1}$ has been used. This suggests that the critical parameter affecting the evaporation of neutrons is the excitation energy gained after the collision, which is similar in both codes, and it is not affected by the collective effects in the level densities description neither by the initial angular momentum of the prefragment.

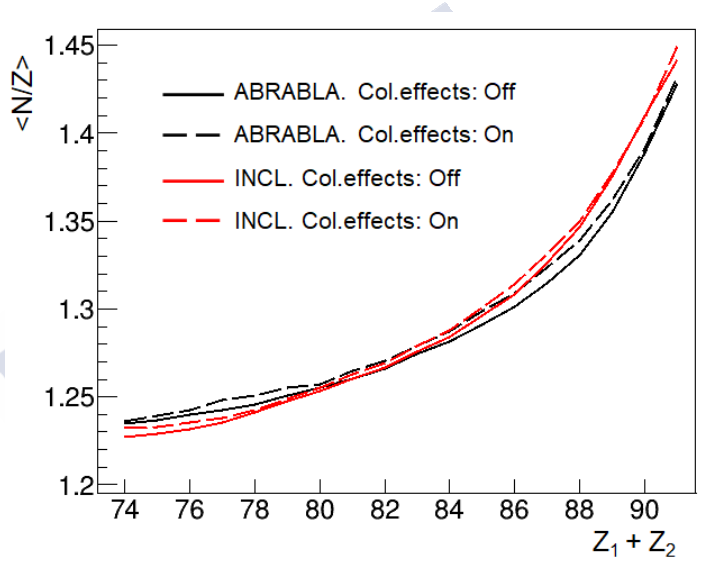

Figure 3.17: *Average neutron excess of the fission fragments as a function of the sum of their atomic numbers obtained for different model calculations using* $\beta_{gs} = \beta_{ss} = 4.5 \cdot 10^{21} s^{-1}$ *. Full and dashed black line correspond to ABRABLA calculations without and with collective effects, respectively. In red, INCL calculations with collective effects (dashed line) and without them (full line).*

In figure 3.18, calculations varying the postsaddle dissipation parameter are displayed as a function of the sum of the atomic number of the fission fragments and compared with the data obtained in this work. The full red line corresponds to a calculation performed assuming the saddle-to-scission statistical time according to the equation 1.10. This calculation clearly overestimates the neutron excess for each $Z_1 + Z_2$ system, specially for the lighter ones, which is another evidence of the need to include a dynamical treatment in the calculations to correctly describe fission. In this sense, the

data are compared with time-dependent calculations based on the equation 1.6, with different dissipation parameters from saddle to scission, namely $\beta_{ss} = 7.5 \cdot 10^{21} s^{-1}$ (full black line), $\beta_{ss} = 4.5 \cdot 10^{21} s^{-1}$ (dashed black line) and $\beta_{ss} = 20 \cdot 10^{21} s^{-1}$ (dashed-dotted black line). According to these calculations, for systems with $Z_1 + Z_2 > 84$, the calculations with $\beta_{ss} = 7.5 \cdot 10^{21} s^{-1}$ and $\beta_{ss} = 4.5 \cdot 10^{21} s^{-1}$ are very similar and can describe the data obtained. However, the difference between these two calculations is found for the lighter ones, where the dynamical effects are more noticeable due to the higher excitation energies acquired. Here, $\beta_{ss} = 4.5 \cdot 10^{21} s^{-1}$ overestimates the data, while $\beta_{ss} = 7.5 \cdot 10^{21} s^{-1}$ reproduces it very accurately. The calculation with a postsaddle dissipation parameter of $\beta_{ss} = 20 \cdot 10^{21} s^{-1}$ clearly under predicts the average neutron excess of the fission fragments as a function of $Z_1 + Z_2$. The sensitivity of this observable to the postsaddle dissipation parameter lies in the fact that higher values of β_{ss} are associated to longer saddle-to-scission times. During this stage, the evaporation of neutrons is more favored than after the scission due to the fact that the energetic cost to evaporate neutrons is smaller from saddle to scission. Beyond this point, the excitation energy available is shared between both fission fragments.

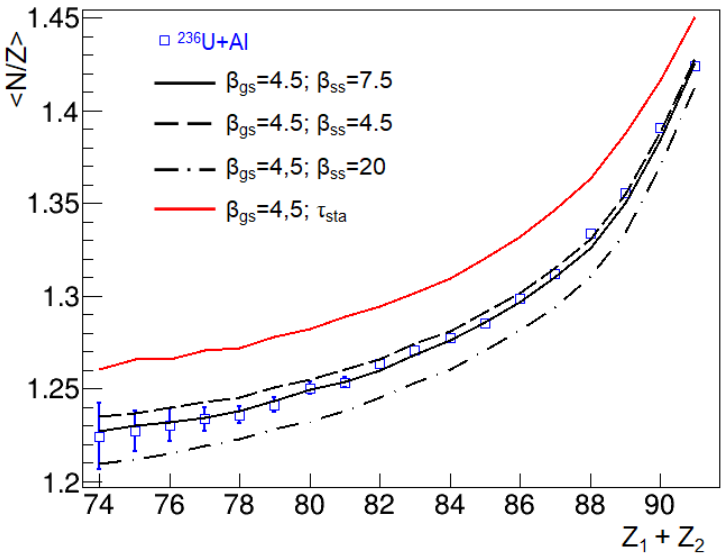

Figure 3.18: *Average neutron excess of the fission fragments as a function of $Z_1 + Z_2$ compared with different model calculations using ABRABLA. Full red line is obtained considering the saddle-to-scission statistical time. Full, dashed and dashed-dotted black lines, correspond to postsaddle dissipation parameters $\beta_{ss} = 7.5$, $\beta_{ss} = 4.5$ and $\beta_{ss} = 20$ in units of $10^{21} s^{-1}$, respectively.*

Therefore, the most suitable value of the postsaddle dissipation parameter results to be $\beta_{ss} = (7.5 \pm 2.0) \cdot 10^{21} s^{-1}$. Assuming a presaddle dissipation parameter of $\beta_{gs} = (4.5 \pm 1.0) \cdot 10^{21} s^{-1}$, both values are quite similar, which lead us to conclude that there is not a significant dependence with large deformations, in good agreement with the $\beta_{ss} = 6.5 \cdot 10^{21} s^{-1}$ obtained by Rodriguez and collaborators [70]. The accurate determination of the dissipation parameter describing the process from the initial configuration to saddle and from saddle to scission is of enormous importance to constraint the fission times on both stages. This is the second time that a measurement of these characteristics is performed, constraining the pre- and postsaddle dissipation parameters using fragmentation- or spallation-induced fission reactions. The main difference and improvement with respect to the work of Rodriguez is that the range of deformations covered in this work are larger than in this previous investigation, so the conclusion that there is no sizeable dependence of the dissipation parameter with deformation is well supported.

3.3 Conclusions

In this chapter, we have investigated the dynamical effects of the fission process using projectiles of ^{236}U at 720A MeV impinging on uranium and aluminum targets. The complete identification of both fission fragments in atomic and mass number allows for the study of different observables sensitive to pre- and postsaddle fission dynamics. The large range of excitation energies and deformations reached by this nucleus made it suitable for this kind of investigation

Regarding the presaddle dynamics, the observables analyzed were the partial fission yields and the standard deviation of the fission fragments atomic number distribution as a function of the sum of both fission fragments atomic number, $Z_1 + Z_2$. The measurements obtained in both reactions showed very similar results, suggesting that there is no dependence with the target utilized to induce fission. This is explained in terms of the limiting fragmentation hypothesis. These results were also compared with other published data for different uranium isotopes, namely ^{238}U from [30] and ^{234}U from [31], showing good agreement.

To study the postsaddle dynamics, the average $<N/Z>$ ratio was analyzed. Again, the values obtained for both fission reactions are in concordance. Studying the behaviour of this parameter as a function of $Z_1 + Z_2$, we observe a decrease for lighter $Z_1 + Z_2$, as the excitation energies these systems are higher, being able to evaporate more neutrons.

Finally, with the aim of benchmarking the different model calculations performed with the data obtained, the intra-nuclear cascade and the abrasion model were coupled to ABLA07. In order to obtain the most suitable description for our observables, the most relevant features of these models were compared. In this sense, we found a significant difference between both codes regarding the angular momentum gained by the prefragment. The excitation energies and the mass of the prefragment were in better agreement. The discrepancy in the value of the angular momentum could be explained in the terms of the different approaches used by both codes to calculate this parameter, as explained in section 3.1.4. The angular momentum play an important role in the description of the partial fission yields as a function of $Z_1 + Z_2$. In this sense, the calculations performed with INCL overestimate the partial fission yields for lighter fissioning systems, leading us to conclude that this angular momentum is too high.

The effect of the level densities in the description of fission was also investigated. In other works [77, 70] this effect was studied in terms of the level density parameter described in equation 1.3. In this work, we investigated the role that the collective effects play in their description. The collective effects take into account vibrational and rotational motions of the nucleons inside the excited nuclei. In particular, we have found that these collective effects have a clear influence in the total fission cross sections but not in the partial fission yields as a function of $Z_1 + Z_2$. Their impact became more evident in the description of the width of the fission fragments Z distributions. We found that the collective effects changed the value of the excitation energy at saddle point, which is proportional to this observable. When collective effects are considered, this observable can not be reproduced, suggesting that there could be a problem with their description that is still under study. Thus, when we remove the collective effects of the calculations, all the observables can be reproduced.

Under these conditions, different calculations have been run to constrain of the pre- and postsaddle dissipation parameters, β_{gs} and β_{ss}. We have concluded that the most suitable values result to be $\beta_{gs} = (4.5 \pm 1.0) \cdot 10^{21} s^{-1}$ and $\beta_{ss} = (7.5 \pm 2.0) \cdot 10^{21} s^{-1}$. This is in good agreement with other works and demonstrates that no significant dependence is found with deformation to describe the dissipative process from the initial state to saddle and from saddle to scission. We have also confirmed that a dynamical treatment of the fission process is required, as pure statistical approaches, like Bohr-Wheeler's, or the stationary Kramers approach overestimate the data.

USC
UNIVERSIDADE
DE SANTIAGO
DE COMPOSTELA

Chapter 4

New approaches to study fission in inverse kinematics

4.1 Introduction

As discussed in the previous sections, the study of the fission process has extraordinarily evolved in the last two decades, thanks to the development of the experimental technique. The complete kinematic measurements permit to detect both fission fragments in coincidence and the study of different observables deliver very promising results that help for a better microscopical description of the process.

However, our knowledge about fission is far from being complete. Within the framework of the R^3B (Reactions with Relativistic Radioactive Beams) international collaboration, we pretend to go a step further in the experiments done to the date to keep improving our understanding of fission. One of the clearest limitations presented in the previous experiments is the unknown excitation energy of the nucleus undergoing fission. For nuclear-induced fission, this excitation energy was estimated using model calculations. In the coulex-induced fission experiments, the excitation energy gained by the nucleus undergoing fission corresponds to the energy range covered by the giant-dipole resonance (GDR) excitation, that typically is between 5 and 20 MeV [140].

A new approach to study fission in inverse kinematics and overcome this limitation would be the use of quasi-free *(p,2p)* scattering reactions to induce fission. This reaction mechanism will allow to determine the excitation energy gained by the *(A-1, Z-1)* remnant undergoing fission from the kinematics of the two protons emitted. Measuring their kinetic energies, as well as their trajectories, one is able to reconstruct their four-momentum and

extract the excitation energy of the process with good resolution using the missing mass spectroscopy. This new information will permit to investigate the evolution of shell effects in the potential governing the fission process, studying the dependence of fission yields with the temperature, due to the fact that these reactions allow to cover a large range of level densities and excitation energies, going from fission barrier energies ($\approx$ 5 MeV) up to 100 MeV, for a given fissioning system. Also, it will be possible to study the energy sharing between the nascent fragments or the dynamics of the process up to and beyond the saddle point.

This last chapter is focused on the possible implementation of a *(p,2p)*-induced fission experiment using realistic simulations. We start carefully describing the *(p,2p)* reactions and how we could use the innovative R^3B setup to measure the emitted protons and fission fragments. Then, the simulations of the experiment are described. The first part of the simulations is focused on the study of the expected resolution in the reconstruction of the excitation energy of the fissioning system. Then, the effect of the δ-electrons produced in the reaction is studied and compared with experimental data obtained at GSI.

This study will allow to have a first picture on how the experiment will look like and how precise our measurements require to be. Also, with the δ-electron study, the setup can be improved and optimized in order to have a better quality data.

4.2 Quasi-free scattering *(p,2p)* reactions

4.2.1 Overview

This reaction mechanism consists of the direct knockout of a proton bound in the ^{A}Z nucleus by a fast incident proton [32], with energies between 100 and 1000 MeV [141, 142]. In this range of energies, the de Broglie wavelength of the projectile is smaller than the distance between nucleons, making the interaction strongly localized. The influence of the spectators nucleons can be then neglected and the interaction can be approached as quasi-free [143]. Therefore, the reaction mechanism becomes rather simple to describe. Studying the kinematic properties of the scattered proton pair, the missing energy in the residual nucleus can be determined and information on the energy gained by the remnant can be deduced. As a result, interesting physical information can be extracted, such as inner shell nuclear structure [144].

4.2.2 Proposed investigation: inverse kinematics *(p,2p)*-induced fission reactions

Thanks to the efforts done in the last years, *(p,2p)* reactions have become a rather well known reactions in the field of nuclear physics. The investigation proposed consists in the combination of this reaction mechanism to induce fission and to better control the first stage of the reaction. This idea was first proposed by W. Henning [145], to measure fission barriers of exotic beams.

Using the inverse kinematics technique, the proposed idea is to accelerate a primary beam of ^{238}U up to around 500A MeV and produce the desired reaction in a liquid hydrogen (LH_2) target. A sketch of the process is depicted in figure 4.1 One of the internal protons of the projectile interacts with the target, creating as consequence a proton pair and an excited recoil nucleus one atomic number unit fewer than the projectile, which in this specific case corresponds to ^{237}Pa. Then, this A-1 remnant undergoes fission, producing two fission fragments.

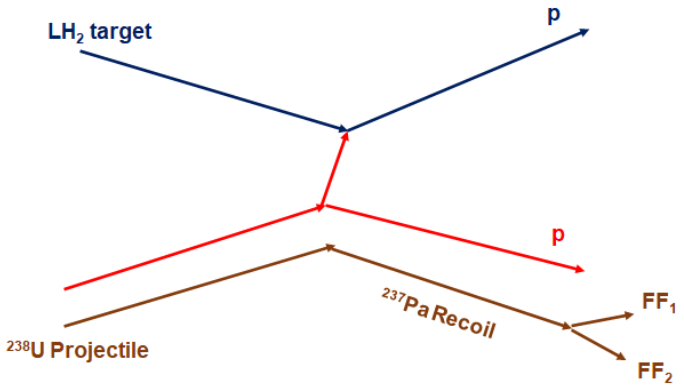

Figure 4.1: *Sketch of the reaction under study:* $^{238}U(p,2p)^{237}Pa$.

In general, this kind of reaction mechanism can be also used to induce fission with exotic secondary beams produced from primary beam fragmentation. The behaviour of the reaction products will be the same, as this process does not depend on the projectile nuclei, forming equally a proton pair, a A-1 remnant and two fission fragments.

Quasi-Free Scattering *(p,2p)* reactions in inverse kinematics

The two protons produced in this reaction are always emitted in forward direction, laying their momentum vector in a plane as the sum of their

azimuthal angles is $\phi_1 + \phi_2$=180°. In a non-relativistic frame, the relative polar angle of two equal mass interacting particles is always θ_{op}=90°. However, when the scattering process requires relativistic kinematics, the Lorentz-boost closes the opening angle by a few degrees. The total momentum of the collision is distributed between both protons and is proportional to the respective proton polar angle. Therefore, measuring the angular distribution of the protons and their kinetic energy, the momentum of the proton pair can be extracted.

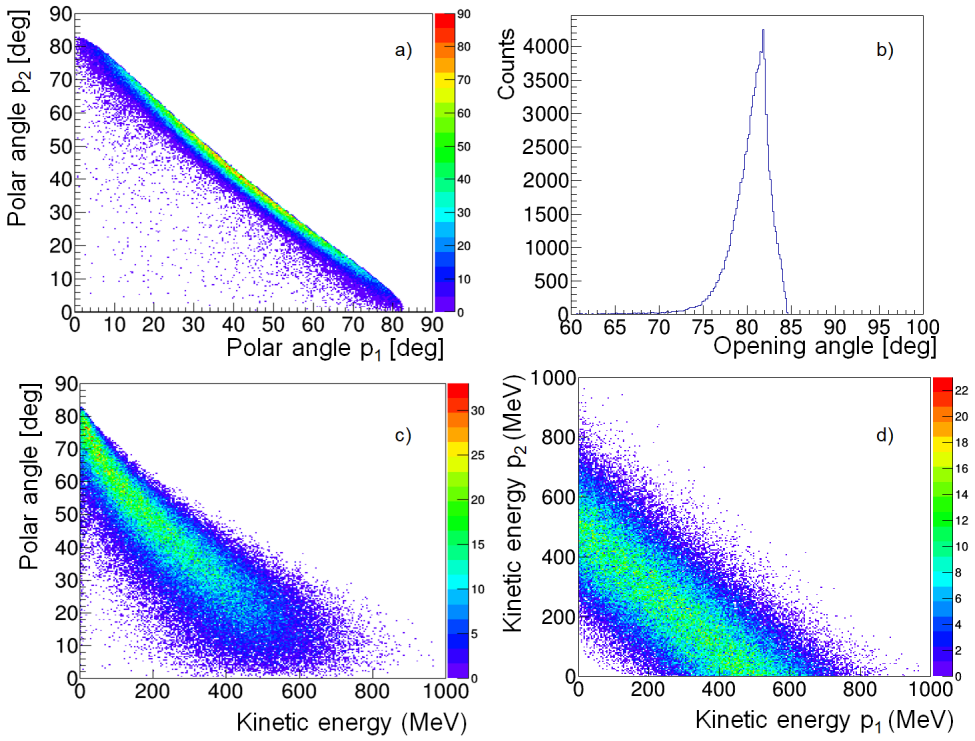

Figure 4.2: *(p,2p) kinematic features for a QFS reaction ^{238}U+p at 500A MeV simulated with R3BRoot. Upper panel: Correlation between both protons polar angles (a) and opening angle (b) are displayed. Lower panel: Correlation between the proton kinetic energy and proton polar angle (c) and both protons kinetic energies correlation (d) are shown.*

The above-explained kinematic features for *(p,2p)* reactions can be simulated using the R3BRoot Panin-Chulkov event generator [146] in particular for a *(p,2p)* reaction produced from a ^{238}U nucleus with a kinetic energy of 500A MeV. It is worth to mention that the interacting internal

proton of the projectile is not at rest in the frame of the projectile velocity, finding itself moving inside the nucleus, so an internal momentum spread has to be taken into account. This momentum spread is described by a gaussian distribution with a σ_p=105 MeV/c [106] for light nuclei. For heavier nuclei, as uranium, its momentum spread is around σ_p=121 MeV/c [143].

In figure 4.2 we depict the kinematics of the reaction ^{238}U+p at 500A MeV. The correlation between the polar angles of the two protons is clearly shown in figure 4.2a), having an opening angle around 81°in the laboratory frame (4.2 b).

The correlation between kinetic energies (4.2 c) is not that narrow as the correlation between polar angles (4.2 a), due to the momentum spread of the proton. Also, the kinetic energy correlation with the polar angle shows that the higher is the energy of the proton, the more forward is emitted (4.2 d). This behaves as expected due to the fact that when the energy of the proton is similar to the energy of the projectile, it is scattered at low polar angles.

Missing Mass spectroscopy

The excitation energy acquired by the recoil nucleus in a *(p,2p)* reaction can be obtained from the four-momentum conservation, that can be written as:

$$\overrightarrow{P}_0 + \overrightarrow{P}_{target} = \overrightarrow{P}_1 + \overrightarrow{P}_2 + \overrightarrow{P}_3 \tag{4.1}$$

Where the index 0 refers to the projectile, 1 and 2 to both emitted protons and 3 to the A-1 recoil nucleus. Expressing each four-vector on their respective components, the four-momentum conservation can be rewritten as follows:

$$\begin{pmatrix} E_0 \\ 0 \\ 0 \\ p_{z_0}c \end{pmatrix} + \begin{pmatrix} m_{target}c^2 \\ 0 \\ 0 \\ 0 \end{pmatrix} = \begin{pmatrix} E_1 \\ p_{x_1}c \\ p_{y_1}c \\ p_{z_1}c \end{pmatrix} + \begin{pmatrix} E_2 \\ p_{x_2}c \\ p_{y_2}c \\ p_{z_2}c \end{pmatrix} + \begin{pmatrix} E_3 \\ p_{x_3}c \\ p_{y_3}c \\ p_{z_3}c \end{pmatrix} \tag{4.2}$$

Until now, it has been considered that the projectile moves just in z-direction with a well defined energy, E_0, and the proton target is at rest. Experimentally, the four-momentum of the two outgoing protons can be reconstructed, by measuring their kinetic energies and tracking their trajectories, to eventually compute their polar and azimuthal angle.

The only piece of information that remains missing belongs to the recoil nucleus, that will be the fissioning system. Measuring the four-momentum of the two outgoing protons and knowing in advance the four-momentum of the projectile and the target, one can obtain information of the four-momentum of the remnant nuclei from the conservation. Specifically, the quantity that can be inferred represents the modulus of its four-momentum. In the Lorentz relativistic formalism, it is well known that the modulus of a four-vector is an invariant quantity. In the case of the four-momentum, this quantity is called invariant mass, I_M and can be expressed as:

$$I_M = \sqrt{(E_0 + m_{target}c^2 - (E_1 + E_2))^2 - ((p_{x_1}c + p_{x_2}c)^2 + (p_{y_1}c + p_{y_2}c)^2} \\ +(\sqrt{E_0^2 - m_{target}^2c^4} - (p_{z_1}c + p_{z_2}c))^2) \quad (4.3)$$

The invariant mass permits to determine how much energy has been transferred to the remnant and infer the excitation energy at which fission happens. Knowing the rest mass of the remnant, the difference between the invariant mass and the rest mass is known as missing mass. This missing mass is exactly the excitation energy transferred to the recoil nucleus that can be obtained as:

$$E^* = I_M - m_{A-1}c^2 \quad (4.4)$$

This reveals the missing mass spectroscopy [147, 148] as an extremely powerful and reliable tool to compute the excitation energy transferred to the recoil nucleus.

4.3 Proposed experimental setup

The setup proposed by the R^3B collaboration to take advantage of *(p,2p)*-induced fission reactions will make use of the SOFIA detectors employed in the first part of this thesis to identify the fission fragments, combined with the R^3B silicon tracker and the CALIFA proton calorimeter. In figure 4.3 a sketch of this setup is depicted, where it can be observed how these two detectors are placed surrounding the liquid hydrogen target. They will be used to measure the momentum of the outgoing protons to eventually obtain the excitation energy. The focus of this section will be centered on the presentation of this novel setup, discussing with more detail the detectors used to measure the two outgoing *(p,2p)* protons.

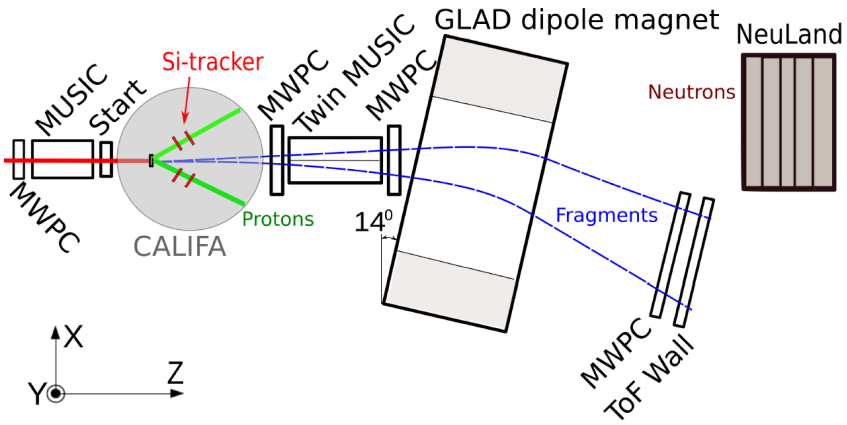

Figure 4.3: *Proposed setup for the upcoming experiments.*

In these experiments, the reaction is induced making use of a cylindrical **liquid hydrogen (LH_2)** target of 1.5 cm length and 3 cm diameter [149]. This target is inside a cell made of two parts, a 125 μm thick Mylar entrance window and a 150 μm thick Mylar exit window, surrounded by a stainless steel body. The target assembling has also a cryostat equipped with a cryocooler to liquify the hydrogen at a temperature close to 20 K.

In order to take advantage of the missing mass spectroscopy, a very precise tracking of the two outgoing protons is performed using a **silicon tracker** [150, 151]. The tracker proposed for this experiment will make use of the Alpha Magnetic Spectrometer (AMS) silicon detectors to track proton positions [152, 153]. These detectors have a size of 72 mm x 40 mm, a 0.3 mm thickness and have been used before in several experiments at GSI [154]. In order to have an optimal momentum resolution in the measurement of the reaction products, a very high position resolution is required. Thus, each sensor has an implantation pitch on the junction side (called S-side or p-side) of the sensor of 27.5 μm. The corresponding read-out pitch is 110 μm, i.e. every fourth strip is connected to a read-out channel. On the ohmic (K- or n-) side of the sensor, the implantation pitch is 104 μm with every strip being read out. This adds up to 640 strips to be read out on the S-side and 384 on the K-side, yielding a total of 1024 channels per sensor, with a position resolution equal to the width of the pitch.

The proposal consists of the use of 6 AMS detectors acting as a tracker, with a frontal plane formed by two AMS detectors and a back plane with 4 detectors, as shown in figure 4.4, divided in two symmetrical arms. The

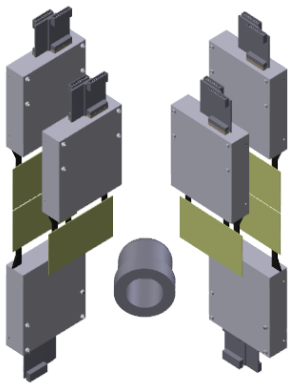

Figure 4.4: *Proposed silicon tracker using 6 AMS detectors. Each detector electronics is shown, as well as the LH_2 target.*

detectors have an inclination angle of 45 degrees with respect to the beam direction in order to increase the detection efficiency. The separation between both planes is 5 cm, being the first plane 5.6 cm away from the center of the target. The polar angle range covered goes form 24.1° to 60.9°. This angular range has been selected taking into account the most likely polar angle emission for *(p,2p)* protons, that is between 20° and 60°, as can be observed in figure 4.5 (left). In figure 4.5 (right), the total angular range covered by the system can be seen. The geometrical efficiency of the tracker will be around 15 % over all *(p,2p)* events. The main loss in the efficiency comes from the fact that the azimuthal range covered is low, even though the polar range covered is quite optimal.

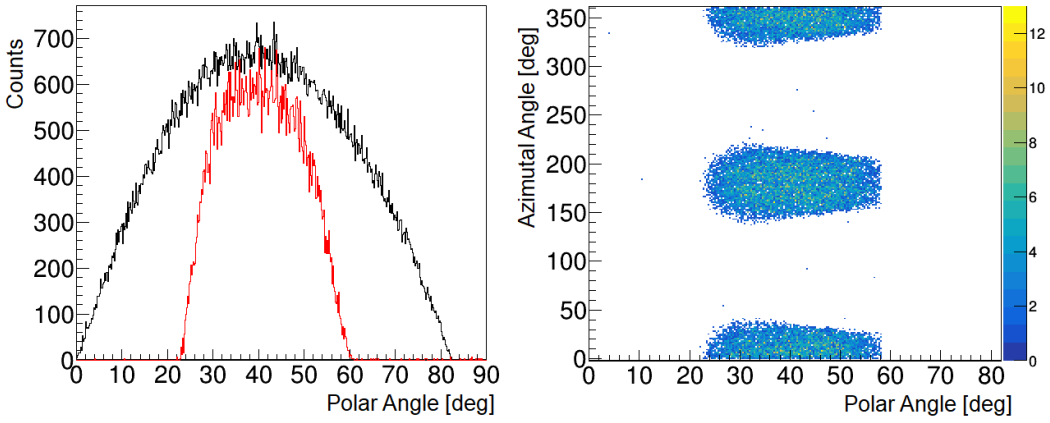

Figure 4.5: *Left: Comparison of the (p,2p) emission polar angle (black) vs the measured polar angle (red). Right: Total angular range covered by the tracker.*

CALIFA (CALorimeter for In-Flight detection of gamma-rays and high energy charged pArticles), is a complex detector that surrounds the target, acting as a total absorption gamma-calorimeter and spectrometer [33, 155]. The detector presents a huge dynamic range, to cover from low energy gamma-rays up to 330 MeV protons, with 2432 detection units of long CsI Tl-dopped scintillator crystals [156] with large area avalanche photo-diode based readout [157]. The shape of the crystals is pyramidal, to reduce the empty space between them, having different dimensions in order to achieve an homogeneous detector acceptance. The detector is divided in two autonomous (azimuthal) symmetric halves. Defined by the beam direction, one is placed at its the left and the other at its right. One of these halves is depicted in figure 4.6 (right).

Each half of the detector is arranged in two different sections (figure 4.6 (left)). The most external section, called barrel, comprises 1952 crystal detection units covering a large polar angular range, from 43° to 140°, orientated within a very compact geometry (internal radius 30 cm) that maximizes the calorimetric properties. The most forward part is an endcap ring containing 480 detection units, with an angular coverage from 20° to 43°, called IPHOS (Intrinsic PHOSwich detector) [158]. Also, in the original conceptual design, this forward endcap has a section for small polar angular range (from 20 ° to 7 °), named CEPA (Califa Endcap Phoswich Array) [159].

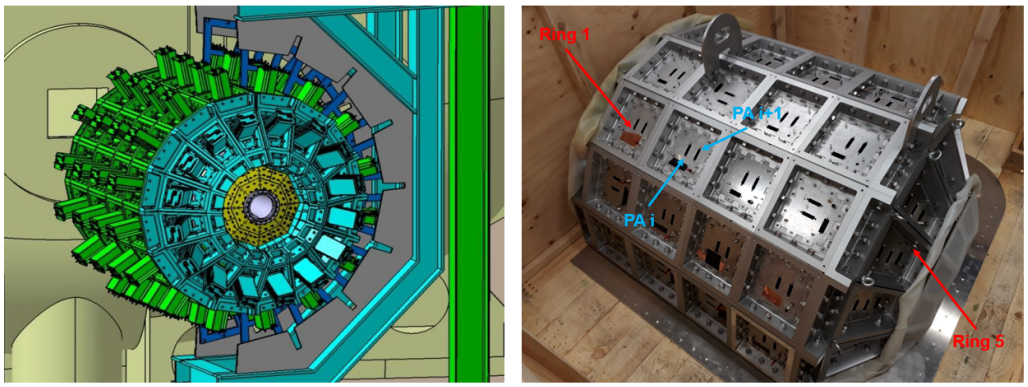

Figure 4.6: *Left: Technical draw of the CALIFA full structure. The green structure corresponds to barrel, blue to IPHOS and yellow to CEPA. Right: One of the CALIFA halves, with five rings to the barrel and IPHOS crystals.*

Depending on the aim of the experiment, CALIFA can work in two different detection modes: high-gain gamma range and low-gain proton range. IPHOS have the capability of working in dual range, but the working range of the barrel needs to be previously assigned. The resolution obtained in the measurement of gamma rays is around 5-6 % for 1 MeV gammas and below 1% for light particles like protons up to 330 MeV. If protons are more energetic, they will punch through the detector, not being able to deposit all their energy. In this case, the energy can be computed using reconstruction algorithms, but with a important resolution degradation. This is one of the reasons of using a projectile beam with a kinetic energy of 500A MeV to induce the reaction. Higher beam energies will lead to a better mass resolution of the fission fragments, but the outgoing *(p,2p)* protons will receive too much energy to be fully stopped in CALIFA. The energy chosen is in good compromise between the capacity of detecting high energy protons with CALIFA and the mass resolution obtained in the measurement of the fission fragments.

A picture of the setup close to the target is showed in figure 4.7. A vacuum chamber with 5 mm aluminum walls has been built to support the vacuum conditions required by the LH_2 target. The shape and dimensions of the chamber are such that CALIFA can be completely closed around it and the silicon tracker can be placed inside.

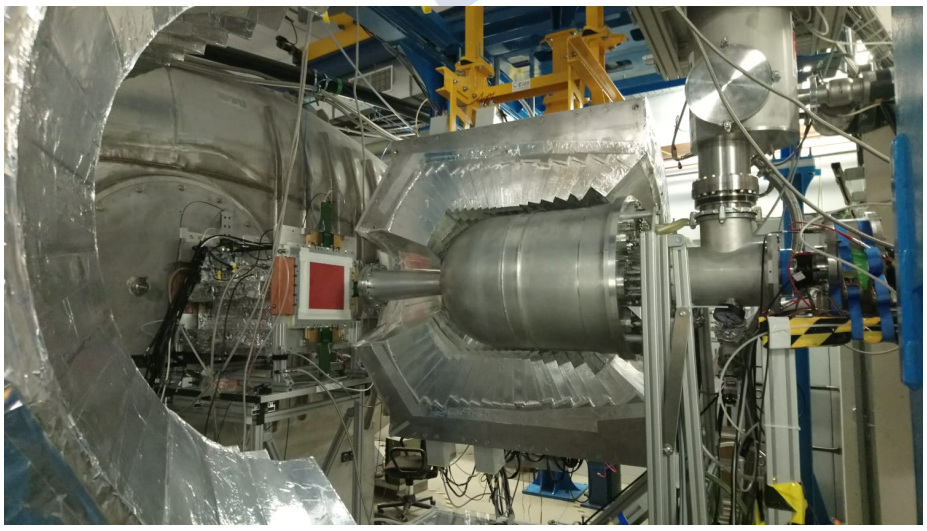

Figure 4.7: *Display of the vacumm chamber where the LH_2 target and the silicon tracker are placed inside, sourrounded by CALIFA.*

For the identification of the fragments produced in the fission of the residual nuclei after the *(p,2p)* reaction the **SOFIA setup** is employed. These detectors have been widely explained in chapter 2. The only change lies in the use of one extra MWPC right after the Twin MUSIC (see figure 4.3), in order to measure not just the polar angle, but also the azimuthal angle. This will help to perform a better tracking of the fission fragments produced in the reaction.

To finish, it is worth to mention some other upgrades carried out in the setup with respect to the experiment analyzed in this thesis. The **GSI Large Acceptance Dipole (GLAD)** [160] is a zero-degree superconducting magnet, filled with Helium. Its specific features, such as a high integral field of about 5 Tm or a maximum bending angle of 40°, allow to achieve a momentum resolution $\Delta p/p$ of around 10^{-3}, providing a better isotopic separation for the fission fragments in comparison with the dipole used in the present work, ALADIN. **NeuLAND** (new Large-Area Neutron Detector) [161] is the next-generation neutron detector designed for the R^3B experiments. It is made of a highly granular plastic scintillators that feature a high detection efficiency, a high resolution, and a large multi-neutron-hit resolving power, specially up to 5 neutrons [162]. These characteristics should help us to investigate the sharing of excitation energy between the two fission fragments.

4.4 Simulations of the missing mass reconstruction

4.4.1 Simulation goal

The aim of these simulations is to investigate the expected resolution in the reconstruction of the missing mass for *(p,2p)* reactions. It is crucial to obtain the best possible resolution in the determination of the excitation energy in order to better constrain our model calculations. The simulations performed include a realistic description of the detectors surrounding the target, namely CALIFA and the 6 AMS detectors acting as silicon tracker, together with the LH_2 target. In figure 4.8, an example of the simulation is shown. The red volume is the CALIFA detector and each grey rectangular plane represents an AMS detector. The discontinuous black lines show the tracks of the two outgoing protons for a given *(p,2p)* simulated event.

Therefore, these simulations will help to obtain the final expected resolution in the missing mass reconstruction as well as to identify the

different contributions to this resolution with the intention to propose further improvements of the setup.

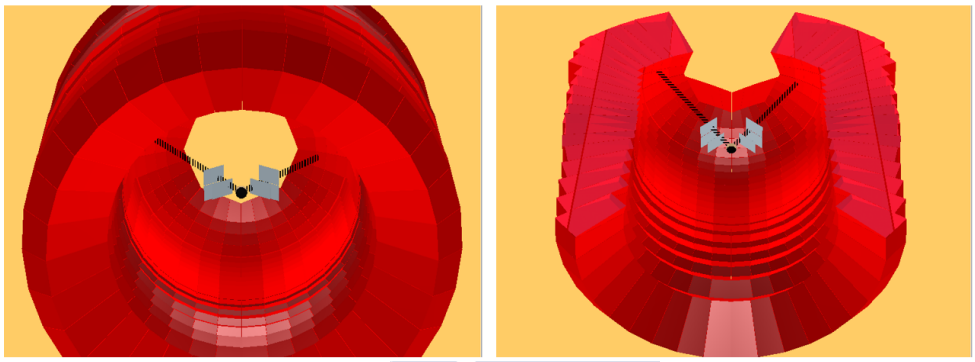

Figure 4.8: *Front and top view of the R3BRoot simulation performed for a (p,2p) event. Liquid hydrogen target, silicon tracker and CALIFA are displayed.*

4.4.2 R3BRoot

The simulations presented in this chapter are performed using the simulation tool called R3BRoot [163, 164]. R3BRoot is a software framework developed at GSI, used not just for simulations but also for data analysis. It inherits basic framework functionality from FairRoot, based on the commonly used software for high energy physics Root, and extending it with R^3B specific detectors and algorithms implementation. R3BRoot has a modular design with shared libraries, which are loaded on demand. The program allows the users to modify the detectors or create new ones. For the description of detector geometry and input for the simulation, multiple formats are supported. It also contains some other general functionality as track visualization, parameter handling or event display, among others. The simulation part is based on the Virtual Monte Carlo (VMC) concept, allowing to simulate realistic *(p,2p)* reactions. Geant3 and Geant4 [165] transport engines are supported by R3BRoot.

4.4.3 Factors contributing to the missing mass accuracy

We used the Panin-Chulkov *(p,2p)* generator [146] to produce QFS events in collisions induced by ^{238}U projectiles with a kinetic energy of 500A MeV impinging on a proton target. In these simulations the momentum spread

of the projectile is set to 121 MeV/c. The excitation energy gained by the remnant nucleus is set to a fixed value, 0 MeV in this case. The reaction position at the target is randomized along its length and the beam spot size is included (see figure 4.9), taking into account the position spread of the primary beam measured in previous experiments by the SOFIA MWPC before the target (σ=1.25 mm) [28].

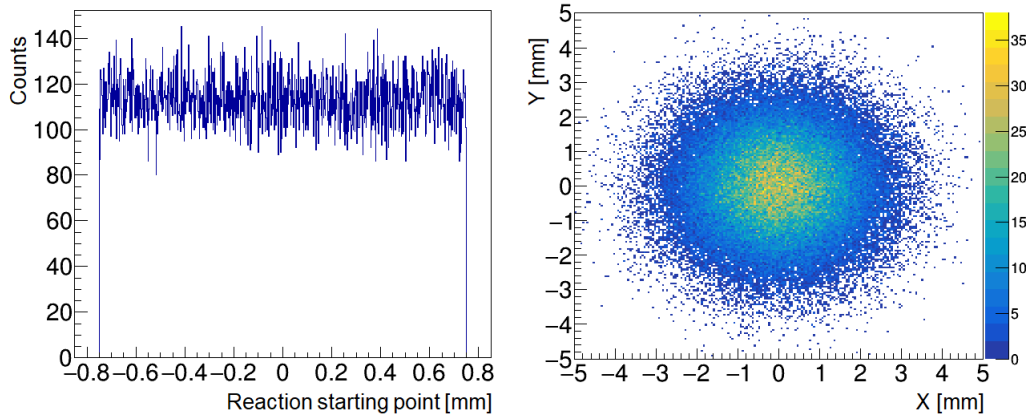

Figure 4.9: *Left: Reaction starting point along the target length. Right: Simulated beam spot.*

A brief comment should be done previously. Energy resolution is defined as $R = \frac{u(E)}{E}$, where the u(E) is the uncertainty of the measurement, corresponding to the FWHM of the gaussian distribution and E the excitation energy of the remnant. As the excitation energy is fixed here, we will talk in this section of accuracy in the missing mass reconstruction instead of resolution.

In order to reconstruct the four-momentum of each proton, the polar and azimuthal angle are obtained from the X and Y position measurements in the AMS detectors, where the experimental position resolution is included (110 μm for the X and Y coordinates). The kinetic energy of each proton is measured taking into account the CALIFA experimental resolution, which is 1% for protons with a kinetic energy below 330 MeV [166]. From equation 4.2, the four-momentum of the protons can be determined, making use of the TLorentz Vector Root class. Then, the beam four-momentum needs to be computed to obtain the remnant invariant mass and thus its excitation energy.

The four-momentum conservation described in equation 4.2 was done under the assumption that the four-momentum of the beam is constant, meaning that its kinetic energy is always the same and all its momentum goes into the longitudinal coordinate, in order to simplify the calculations. In reality, there are several factors affecting on the determination of the beam four-momentum, like the energy and angular straggling induced by the materials placed along the beam line or the location straggling, among other that will be later explained. Thus, in the simulation we have included the initial energy and momentum spread of the beam projectiles to provide a more accurate picture, taking this into account to obtain the missing mass.

Once the four-momentum of the two outgoing protons and the beam are computed, including the detector resolution and the straggling induced by the setup on their determination, the accuracy in the missing mass reconstruction is obtained. This value results to be around 4.6 MeV for a pure QFS *(p,2p)* reaction, *ie*, when the interaction is produced between the proton target and only one of the protons inside the projectile, remaining the rest of them as spectators.

Now, the different contributions to this accuracy are broken down. The sources that affect to the excitation energy accuracy come from the straggling induced by the target and the silicon tracker, the experimental resolution of the detectors and the accuracy in the determination of the beam four-momentum. Running several simulations "switching off" different of these components, one can study how each source impact on the accuracy obtained. These contributions are described in table 4.1.

Source	**Accuracy (MeV)**
Beam four-momentum	0.79
Target total straggling	2.06
Tracker total straggling	3.12
Tracker Position resolution	1.40
CALIFA Energy resolution	1.98
Final missing mass accuracy	4.60

Table 4.1: *Different contributions to the final accuracy achieved in the determination of the excitation energy.*

The impact of the beam four-momentum is the less critical parameter, as its contribution to the final accuracy is just 0.79 MeV. This value is affected by different factors. The first one is the angular and energy straggling

induced by all the matter placed along the beam line, among which are the plastic scintillator or the accelerator window, leading to an uncertainty on its energy and momentum. This straggling presented has been calculated using ATIMA, obtaining an energy straggling of 48.3 MeV and an angular straggling of 0.636 mrad. Also, the beam energy can be determined from its momentum after the beam passes the SIS18, with a resolution of $\Delta p/p=10^{-3}$ [88, 90]. This source has the least impact on the beam four-momentum accuracy. To finish, it is important to determine where the reaction takes place inside the target. From the measurement of both protons trajectories, it is expected to reconstruct the reaction vertex with an accuracy of around 1 mm, inducing an uncertainty in the calculation of the primary beam energy, which for a 500A MeV ^{238}U beam is 1.44A MeV. This is called location straggling and its effect is also computed and taken into account, resulting to be the most relevant contribution to the beam four-momentum accuracy.

The main contribution to the final accuracy comes from the total straggling (both energy and angular) induced by the target and, specially, by the silicon tracker having more impact than the intrinsic resolution of the detectors. From these results, one can think about potential improvements for the future in order to improve the accuracy in the determination of the excitation energy. These upgrades should go in the direction of reducing the thickness of the tracker and the length of the target, as they are the dominant contribution to the accuracy obtained in the excitation energy reconstruction. Reducing the diameter of the target hardly affects the accuracy, as the protons are emitted in forward direction with an average angle of 40° so they will traverse almost the same length regardless of the diameter. New simulations were run to study how these changes affect to the excitation energy accuracy. Even though the straggling is the dominant contribution, it also has been studied how an improvement in the tracker resolution can help to improve this value. Finally, a possible reduction in the energy resolution in CALIFA down to 2%. The results of this study are summarized in table 4.2.

The first conclusion is that the use of thinner layers for the tracker clearly reduces the impact of the tracker straggling in the reconstruction of the excitation energy. If we were able to design a 50 μm silicon tracker, its relative impact can be reduced from 3.12 to 1.36 MeV. The straggling induced by the target can be moderated reducing its length. Using a target thickness of 0.5 cm instead of 1.5 cm, the impact of this source in the measurement of the excitation energy is reduced nearly a 30%. Combining the two most favorable results for the tracker thickness and the target length (50 μm and 0.5 cm

Target length	**Accuracy (MeV)**
1.5 cm	2.06
1.0 cm	1.72
0.5 cm	1.47
Si tracker thickness	**Accuracy (MeV)**
300 μm	3.12
100 μm	1.67
50 μm	1.36
Si tracker position resolution	**Accuracy (MeV)**
110 μm	1.40
50 μm	0.98
CALIFA Energy	**Accuracy (MeV)**
2%	2.87
1%	1.98
Beam location straggling	**Accuracy (MeV)**
1 mm	0.79
0.5 mm	0.46

Table 4.2: *Study of the potential improvements in the excitation energy accuracy.*

length, respectively), the contribution of the total straggling contribution to the excitation energy can be reduced down to around 2 MeV, comparable with the contribution induced by the CALIFA energy resolution when this value is 1%. In this sense, it is important that CALIFA could guarantee a resolution of 1%, as some measurements shows that the energy resolution could be around 2% [167]. In this case, the impact to the final missing mass accuracy will increase up to 2.87 MeV and a reduction in the target and tracker thickness would not be very effective. Thus, if a significative improvement is desired in the future, CALIFA resolution should be better than 1%.

Regarding the tracker position resolution, this parameter is not that critical as the above mentioned, but it still has some margin of improvement. By being able to determine the X and Y positions with a resolution two times better than the presently obtained by the AMS detectors (50 μm instead of 110 μm), the relative contribution of this parameter is reduced to 0.98 MeV. To finish, the excitation energy accuracy can also be slightly improved reducing the contribution of the beam location straggling. For example, determining the reaction vertex with a position accuracy of 0.5 mm, the contribution of the location straggling in the beam four-momentum

is reduced to 0.46 MeV.

All these proposed improvements for the different parts of the setup can be combined in order to determine how they affect in the missing mass accuracy. In table 4.3, the final accuracy is calculated, combining the best case for the potential upgrades that have been investigated. After this study, the experimental accuracy is improved to 3.08 MeV, which represents an improvement of 33% with respect of the 4.6 MeV expected for the present experiment. In this scenario, CALIFA is the most limiting source to the final accuracy.

Source	Accuracy (MeV)
Beam four-momentum	0.46
Target straggling	1.47
Tracker straggling	1.36
Tracker Position resolution	0.98
CALIFA Energy resolution	1.97
Final missing mass accuracy	3.08

Table 4.3: *Accuracy obtained in the missing mass reconstruction combining the improvements proposed for the setup.*

4.4.4 Realistic simulation of *(p,2p)*-induced fission reactions

Finally, we have simulated a realistic *(p,2p)*-induced fission reaction using the intra-nuclear cascade for a p+^{238}U reaction at 500A MeV. From all the events created in this calculation, we will select those corresponding to *(p,2p)*-induced fission. The main difference here lies on the fact that most of these events are not generated by QFS scattering, allowing us to study how this can affect to the experimental accuracy. The reaction is produced in direct kinematics, so a Lorentz boost is applied to obtain the correspondent ^{238}U+p reaction with the proper kinematical description, whose products are the two outgoing protons and two fission fragments. Therefore, this simulation is a more realistic approximation of what will be found in the experiment. In an event-by-event basis, the calculation produces an excitation energy value for the reaction, whose range goes from a few MeVs to more than 150 MeV, peaking around 40 MeV. This is displayed in figure 4.10, for events with two protons and two fission fragments in the exit channel.

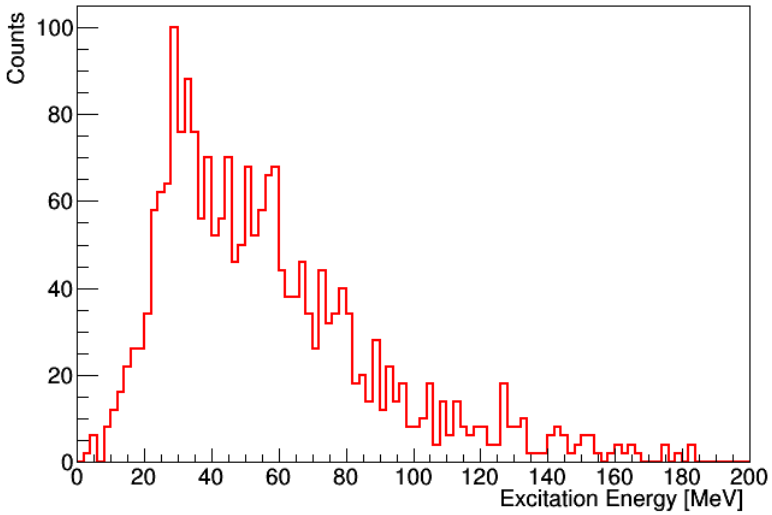

Figure 4.10: *Simulated excitation energy distribution in a $^{238}U(p,2p)$fission reaction generated from INCL.*

With the use of the missing mass spectroscopy, we can evaluate the accuracy in the missing mass reconstruction for different energy ranges to see how it changes with the excitation energy. In figure 4.11, the obtained accuracy is presented as a function of the excitation energy. The main conclusion is that the accuracy is degraded as the excitation energy moves to higher values. It is known that the events produced in QFS reactions will induce less excitation energy, due to the fact that the collision occurs only between two particles, with the rest as spectators. Therefore, when more nucleons take part in the collision, the excitation energy increases and the collision does not behave as a QFS. The missing mass spectroscopy assumes the QFS behaviour of the collision, so when more nucleons are involved, the description is not that precise, due to the multiple collisions taking place and the angular correlation between the outgoing protons changes and the accuracy degrades. Below 35 MeV, the accuracy obtained matches with the experimental accuracy calculated in previous section, staying around 4.6 MeV. When the excitation energy increases, the accuracy degrades from the initial 4.6 MeV up to 9 MeV for excitation energies close to 90 MeV. In figure 4.11, we have separated the experimental contribution and the so-called physical contribution, which takes into account the loss of accuracy when the collision does not behave as QFS. Of course, the accuracy obtained for the setup just depends on the sources mentioned in the previous section, so the degradation in the excitation energy accuracy comes from this physical effect.

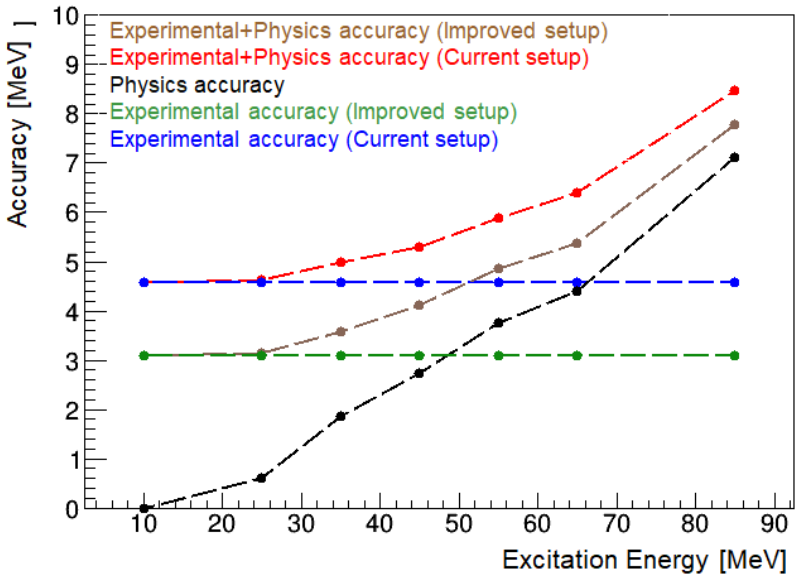

Figure 4.11: *Variation of the total accuracy (red) with the excitation energy value for a $^{238}U(p,2p)$fission reaction, separating the experimental (blue) and Physics (black) contributions, for the current setup. The experimental (green) and total (brown) contributions for an upgraded setup are also displayed.*

In previous figure, the accuracy of the excitation energy using the proposed improvements is also depicted. The main difference with the current setup stays in the region below 40 MeV, as for higher energies, the physical contribution is dominant and the accuracy is similar. In figure 4.12, the energy resolution is displayed as a function of the excitation energy both for the current and the improved setup. This value is obtained dividing the accuracy by the excitation energy. We can observe how the resolution is better for higher excitation energy values, staying around 8-10%, while for values below 40 MeV, where the excitation energy distribution presents more statistics, is degraded up to 25% on average for the present setup. Thus, it is of utmost importance to upgrade the setup in order to improve the resolution. With the proposed improvements, the resolution in the low energy region stays close to 15% on average, representing a significant improvement. For higher excitation energies, both resolutions are similar due to forementioned physical effect.

In conclusion, for the present experiment, the resolution obtained for high excitation energy is reasonably good. For low excitation energy values, this resolution has room for improvement. Due to the fact that in this region the

QFS scattering condition is a good approximation, the resolution can only be improved upgrading the setup. With the proposed upgrades, resolution can be clearly improved, leading to a better determination of the excitation energy that can help to constrain model calculations.

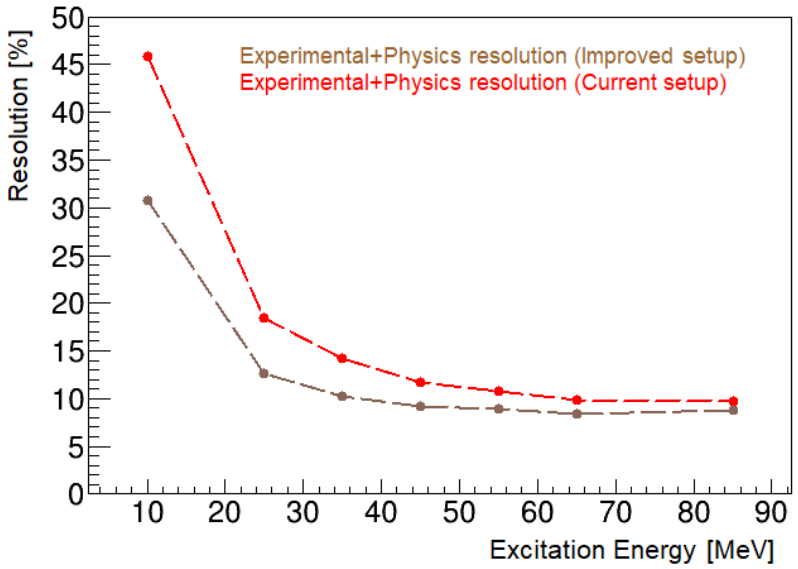

Figure 4.12: *Resolution obtained for the current setup (red) and for the upgraded setup (brown) as a function of the excitation energy.*

4.5 Investigation of the impact of the δ-electrons produced at the target

4.5.1 Simulation goal

The simulations carried out in this section are focused on the investigation of the δ-electron production in ^{238}U*(p,2p)*+fission reactions. This study is important due to the fact that some δ-electrons produced in the target will be able to reach the silicon tracker. This is specially problematic if the number of δ-electrons reaching the tracker is high and if the energy deposited by them is similar to the energy deposited by protons. In the later case, the identification of the *(p,2p)* outgoing protons becomes rather complicated.

The aim of the study is to give answer to these and some other issues, basing our simulations in the above explained setup close to the target. The

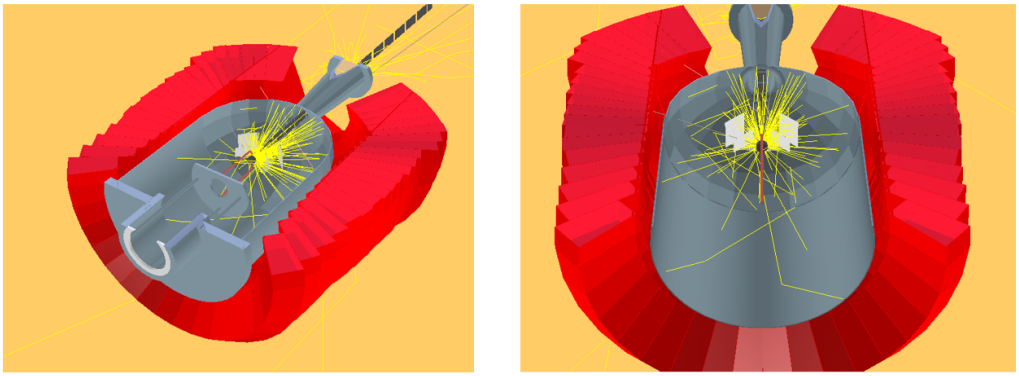

Figure 4.13: *Side and top view of the simulation performed. Yellow tracks correspond to δ-electrons produced inside the target resulting of the ionization produced by the fission fragments.*

input reaction is the same as used in section 4.4.4, where two fission fragments and two protons are generated from a INCL calculation. We will focus on the electron multiplicity presented on each AMS detector and on how this multiplicity can be reduced to separate protons and electrons in order to have clearer measurements. A display of the simulation performed is depicted in figure 4.13. Yellow tracks correspond to the δ-electrons produced inside the target, where the reaction occurs.

4.5.2 Physical background

Charged particles traversing a specific material lose part of its initial energy on their way through. Their interaction with matter is primarily produced through coulomb forces between their positive charge and the negative charge of the electrons within the atoms of the material. Depending on the energy transferred to the electron, the impulse received may be enough either to move it to a higher-lying atomic shell (excitation) or to completely remove it from the atom (ionization). The term knock-on electron or δ-electron is used for secondary electrons ejected from their orbit with sufficient kinetic energy to travel a significant distance from its point of interaction. The number of δ-electrons produced from charged particle interactions is given by [168, 104]:

$$N_\delta = \Sigma_{in} \Delta x \tag{4.5}$$

where Δx is the step length of the charged particle and Σ_{in} is the collision ionization probability per unit of distance traveled. For an incident particle of

velocity v and charge z, this parameter can be obtained from the Bethe-Bloch formula, having the following explicit dependencies:

$$\Sigma_{in} \propto \frac{z^2}{\beta^2} \tag{4.6}$$

where $\beta = v/c$. This shows that the probability of generating δ-electrons is strongly dependent on the charge of the incident particle. Assuming fully stripped ions, the heavier the ion, the more δ-electrons are produced. In comparison with other *(p,2p)* experiments with light ions, such as carbon or oxygen, the production of δ-electrons by heavy ions such as uranium will be significantly higher. Also, there is an inverse dependence with the square of the ion velocity, meaning that more energetic ions are expected to produce a smaller number of δ-electrons. Following the momentum conservation, the kinetic energy transferred to the electrons, K, by a particle of velocity v, satisfies the equation 4.7 :

$$K_e = 2m_e v^2 cos^2\theta \tag{4.7}$$

being θ the deflection angle, relative to the incident particle direction. This means that the most energetic δ-electrons will be mainly emitted in forward direction.

4.5.3 Simulation results

Figure 4.13 shows that the number of electrons produced in this kind of reactions is not negligible. The depicted tracks do not correspond to all the δ-electrons generated, as an important part of them are reabsorbed inside the target. However, the most energetic electrons are able to leave the target, as well as those produced closer to its end.

Firstly, we will investigate the multiplicity of energetic electrons impinging on the front and rear detectors of the silicon tracker. This multiplicity is determined in the simulation as the number of strips hit by electrons. Therefore, this multiplicity is not exactly the number of electrons reaching the tracker, as one electron can lose part of its energy on consecutive strips. As shown in figure 4.14, the multiplicity obtained in this way is above 13 in the front planes and close to 4 in the rear detectors, equally distributed in the right and left arm.

This multiplicity is relatively high and can generate a conflict to identify the protons signals. This issue can be investigated computing the energy lost by the electrons and protons on each AMS strip. The result is shown in

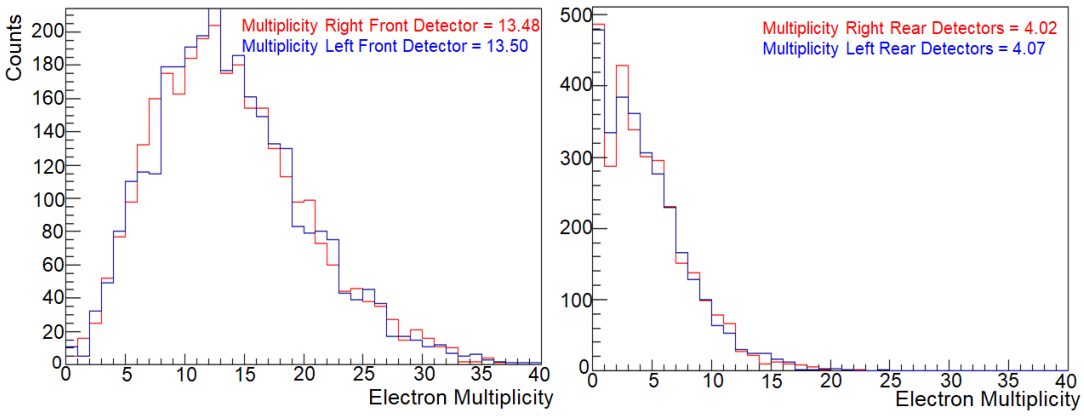

Figure 4.14: *Electron multiplicities on the AMS detectors. Left: Front detectors. Right: Rear detectors.*

figure 4.15, where the distribution of the energy lost by protons is multiplied by a factor of 5. The average energy lost by electrons is around 60 KeV and 120 KeV for protons. However, an important overlap in the electron and proton energy lost spectra is observed. From these results, it is clear that the δ-electron production can difficult the tracking of the two outgoing *(p,2p)* protons. In consequence, it is important to reduce the number of δ-electrons reaching the tracker.

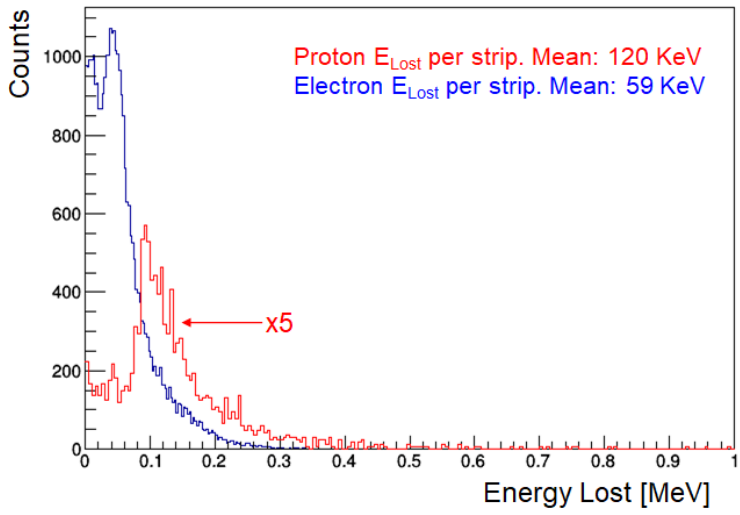

Figure 4.15: *Energy lost per strip in the AMS detectors for protons (red curve) and electrons (blue curve). Proton spectrum is multiplied by a factor of 5.*

For this purpose, the effect of placing a layer in front of the silicon tracker acting as shielding was investigated. Several simulations were run to study the potential reduction in the δ-electron multiplicity using materials with different atomic numbers. The choice of the layer's width is a compromise between being able to shield the detector efficiently and to induce the minimum straggling possible in the passage of protons. In this sense, all the simulations were done with a shielding layer of 10 μm thickness.

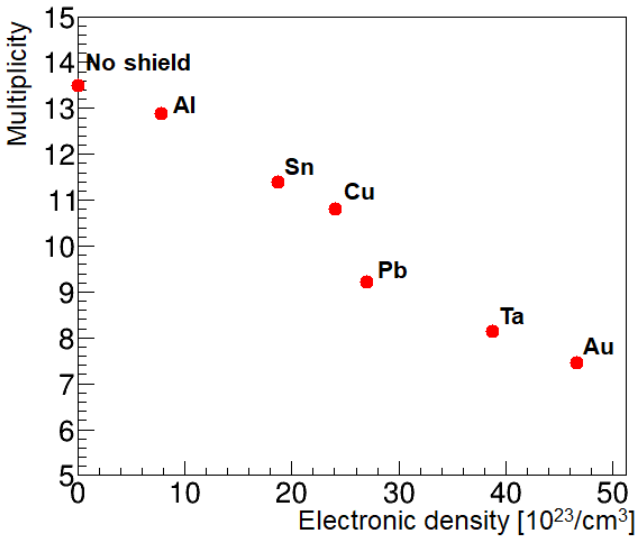

Figure 4.16: *Electron multiplicity in the front detectors as a function of the electronic density of the shielding materials.*

The results of the simulations are depicted in figure 4.16. From these results, we can conclude that a 10 μm gold layer is the best choice, since the reduction in the δ-electron multiplicity is close to 50 %. The reason of this reduction can be explained in terms of the electronic density of each material. In figure 4.17, the energy lost spectra in the front silicon detectors are shown when using and not the shielding layer. The energy lost is practically the same, just a 3-4 KeV displacement is produced. So, the reduction in the multiplicity comes from the fact that δ-electrons that initially reached the tracker, are now scattered in different directions or bounced back, with more probability when the electronic density of the material increases. Only very low energetic δ-electrons are stopped in the layer. We can observe how other materials used in the past to shield detectors, like aluminum in [169], have a smaller effect in the reduction of the δ-electron multiplicity.

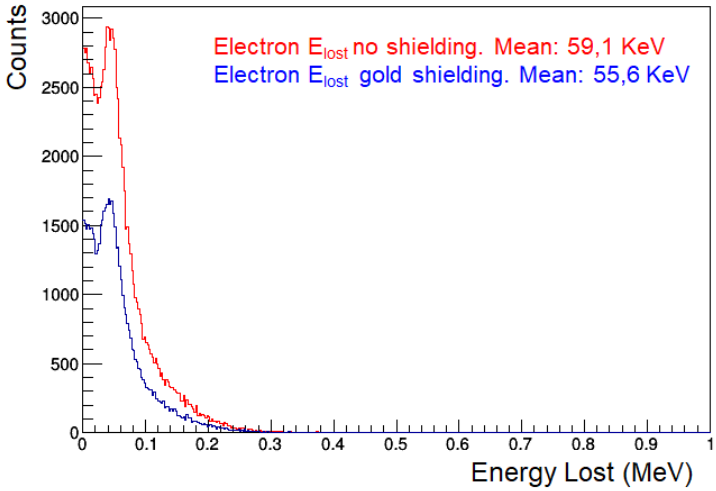

Figure 4.17: *Comparison of the electron energy lost on AMS front detectors, without shielding (red curve) and with gold shielding (blue curve).*

To complete the study, an energy threshold can be added to the analysis to further reduce the δ-electron multiplicity. The choice of this threshold has to be efficient enough to minimize the δ-electron signals in the detectors without losing too many proton events. From the energy lost spectra depicted in 4.15, a threshold of around $\sim$ 70 KeV could be the most efficient. Under this condition, the percentage of *(p,2p)*+fission events without any δ-electron signal in the detectors is investigated. The results are displayed in table 4.4. The same study was done with a higher and lower energy threshold.

Energy Threshold	**Zero electrons events (%)**
100 keV	57.2
70 KeV	37.6
50 KeV	13.3

Table 4.4: *Percentage of events without electron signal in the silicon tracker using different energy thresholds and shielding the detector with a 10 μm gold foil.*

The percentage of events with no electron signal combining this energy threshold with a 10 μm gold shielding layer is $\sim$ 37.6%. Thus, the combination of an effective shielding material with a reasonable energy threshold clearly reduces the events with any electron signal in the silicon tracker. However, more information is needed to correctly identify the protons in the experiment. Using the signals from CALIFA and the silicon

tracker, we will be able to reconstruct all the possible particle trajectories and only one of them should coincide with two proton trajectories coming from the target. In this sense, a reduction of the δ-electron background will help to identify the *(p,2p)* with higher accuracy.

4.5.4 Benchmark of simulations with measured data

In April 2020, a beam test was performed at GSI facilities, employing CALIFA and the silicon tracker detectors. Using a primary beam of ^{208}Pb at 500A MeV and a 2.3 mm width CH_2 target, the effect of the δ-electron production was one of its principal goals. A 10 μm gold shielding layer was placed 1 cm in front of one of the tracker arms in order to explore the potential multiplicity reduction shown by the simulation. Thus, a new simulation has been performed under these conditions to validate the results with experimental data. An image of the simulation display is shown in figure 4.18 (left), together with the position and numeration of the AMS detectors (right). The gold shielding foil was mounted in front of the right arm.

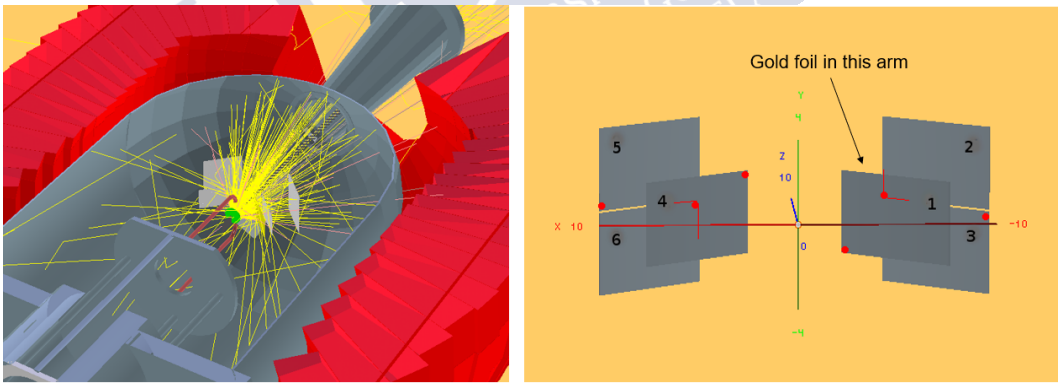

Figure 4.18: *Left: Top side view of the simulated setup for the test. Yellow tracks corresponds to the δ-electrons produced by the ^{208}Pb beam. Right: Schematic view of the disposal of the AMS detector. Red spot indicates the first strip in both K (X) and S(Y) sides.*

Fission fragments were employed as input for the simulations in the last section due to the fact that during the experiment we will trigger *(p,2p)*+fission events, so other events producing δ-electrons will be not considered. In the simulations performed here, the target has changed and the δ-electrons are produced from the ionization of the ^{208}Pb beam, so different values of the δ-electron multiplicities are expected. However, in spite

of the possible differences, the percentage of agreement of the experimental results with the simulation can be extrapolated to the previous calculations.

The analysis of the measured data to obtain the δ-electron multiplicity in the silicon tracker has to be done with the help of the CALIFA detector. Electrons should not be able to reach CALIFA, as they will be deflected or stopped in the walls of the vacuum chamber. Therefore, any coincident signal in CALIFA and in the silicon tracker was not taken into account. Also, each strip of the AMS detectors presents a gaussian noise signal called pedestal. To remove it out of the analysis, one should select a energy region where the likehood of having a noise signal is low. For the present analysis, we have used two different energy thresholds to reject noise contributions, pedestal + 3σ and pedestal + 5σ.

In figure 4.19 the experimental results of the δ-electron multiplicity obtained for the detectors are depicted, considering two different pedestal subtractions. Unfortunately, the detector 1, placed right behind the gold layer, did not work properly, so no valid information could be extracted from it. The multiplicities displayed for an energy threshold of pedestal + 3σ (left) are approximately twice higher than those obtained with a pedestal + 5σ (right). In the first case, it is possible that some noise signals are included, while in the second, noise is completely removed but they also may be some low energy electron signals. In any case, the multiplicity of the rear detectors with gold shielding (2 and 3) is clearly reduced in comparison with the non-shielded detectors (5 and 6).

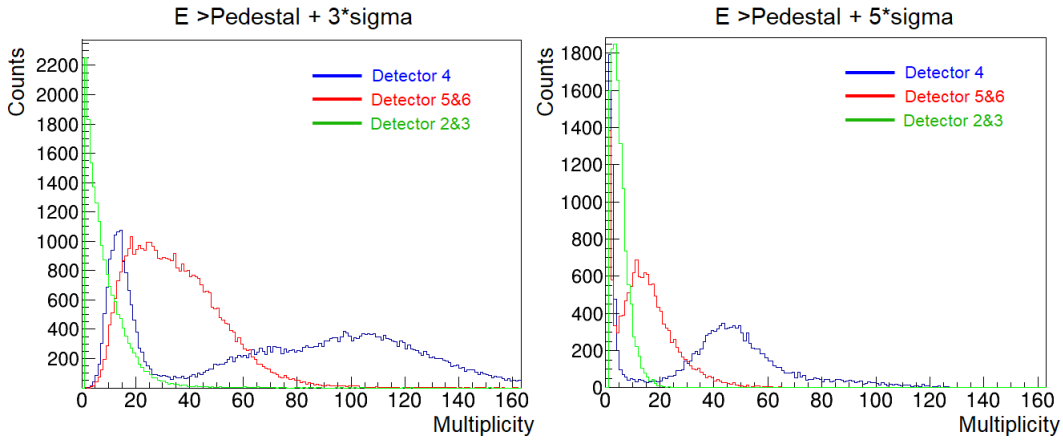

Figure 4.19: *Experimental electron multiplicity for different energy thresholds, pedestal+3σ and pedestal+5σ, respectively.*

These results can be compared with the simulation. One significant limitation of the measurement was the absence of good primary beam tracking, so it was difficult to determine how centered the beam was. Also, the beam spot could not be measured, but it is expected to be around 10 mm diameter. Thus, a 12 mm diameter beam spot size was considered for the simulations. Results are depicted in figure 4.20 considering two different beam positions.

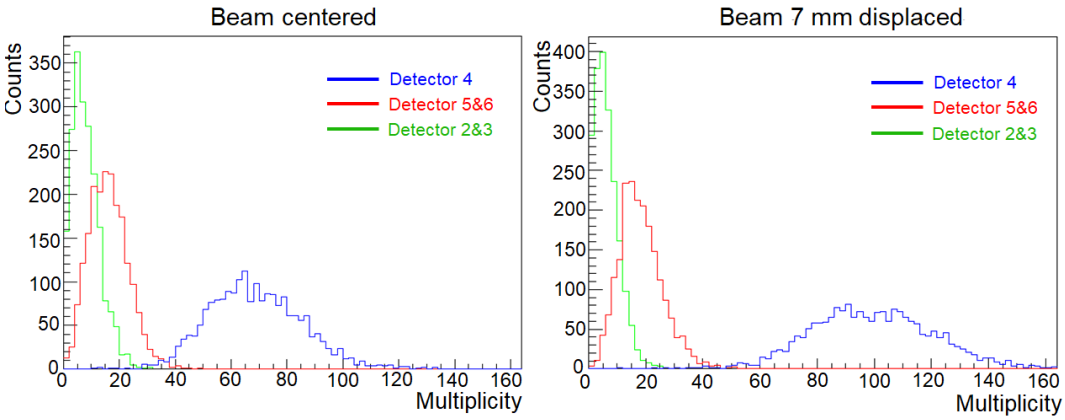

Figure 4.20: *Simulations results for electron multiplicity for different beam positions, centered and 7 mm displaced, respectively.*

Despite one of the detectors did not work, two interesting conclusions can be extracted. First one is that the effect of the gold layer is clearly observed, as the multiplicity of the shielded rear detectors is lower. Measured data show a reduction of around 60 % of electron signals thanks to the shielding, while simulations show a reduction of 48% for a centered beam and 70 % for a 7 mm displaced beam. So even though a displaced beam can vary the multiplicities, the use of a 10 μm gold shielding layer clearly helps to reduce the electron multiplicity in the silicon tracker detector.

The second conclusion is related with the total multiplicity values. On one hand, for an energy threshold of pedestal + 3σ, the multiplicities are higher than those obtained for a centered beam, having a better agreement with those obtained for a 7 mm displaced beam. On the other hand, with an energy threshold of Pedestal + 5σ, the multiplicity spectrum agrees more with a centered beam, but is likely to cut some electron signals in this region. To know exactly which energy the pedestal signal corresponds to, the AMS detector needs to be previously calibrated. Other difference with the simulation is the low multiplicity peak observed in detector 4 in the data spectrum, not observed in simulation. It can be due to fragmentation

reactions produced before the target, arriving fewer electrons in these cases to the detector. Regardless of these differences, from these results, the electron multiplicity obtained in the simulations matches reasonably well with the experimental results with an error margin of 25-30 % in the majority of the cases.

Another piece of information that can be extracted is the angular distribution of the electrons. From equation 4.7, it is expected that the most energetic electrons are emitted in forward directions. The simulation images displayed in figures 4.13 and 4.18 suggest the same, being the electron trajectories forward focused. Thus, the strips covering low polar angles should collect more electron signals. The comparison between data and simulation is shown in figure 4.21, where the number of hits for AMS detector number 5 is displayed. The strips represented correspond to the horizontal side. Both are in very good agreement, leading us to conclude that the δ-electron propagation is kinematically well described by the simulation.

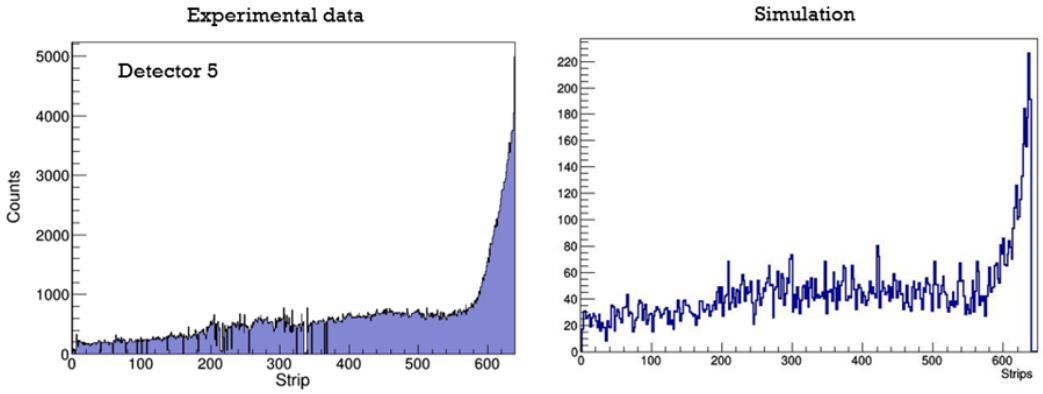

Figure 4.21: *Left: Electron polar angular distribution in detector 5 extracted from experimental data. Right: Electron polar angular distribution given by simulation.*

To finalize, the cluster size was investigated in order to check how the electrons deposit part of their energies on the AMS detectors. The cluster size is defined as the number of consecutive strips presenting an electron signal. Again, simulation and data are in good agreement, as depicted in figure 4.22. This means that electrons deposit partially their energy on one or two strips, on average, and also that the partial energy lost deposition per strip is correctly described by the simulation.

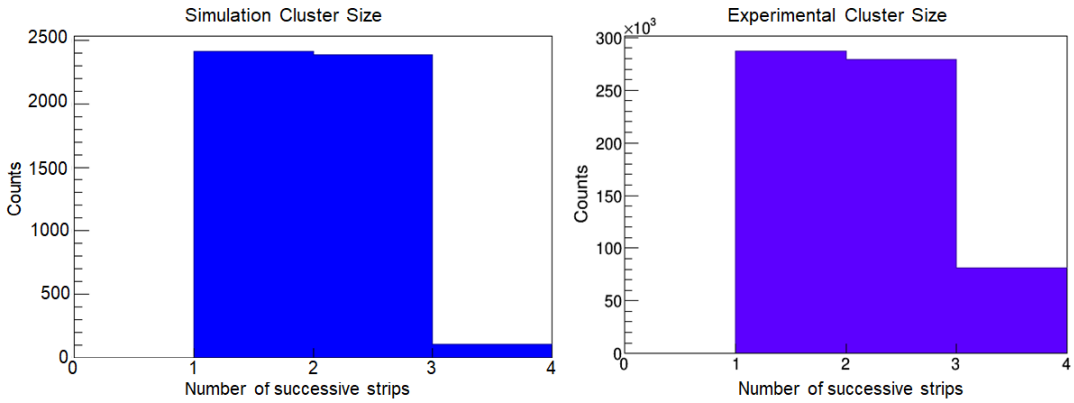

Figure 4.22: *Simulation (left) and experimental cluster size (right).*

4.6 Conclusions

This chapter was dedicated to investigate the potential use of *(p,2p)* quasi-free scattering reactions to induce fission. With the main objective of going a step further in the study of fission reactions, we proposed to use the missing mass spectroscopy to obtain a direct measurement of the excitation energy presented in the fission process. To successfully carry out this task, a new experimental apparatus was proposed, integrating the SOFIA setup with new detectors surrounding the target area, namely a silicon tracker formed by 6 AMS detectors and CALIFA. To study the angular acceptance of the proposed tracker and, most important, the expected resolution in the excitation energy calculation, advanced R3BRoot simulations were realized. This resolution depends both on the experimental setup and the accuracy of the quasi-free scattering approximation in the range of excitation energies under study. In this sense, an experimental accuracy of around 4.6 MeV was obtained. This value dominates at low excitation energies. As the excitation energy increases, the accuracy is degraded, as the QFS approximation used to compute the excitation energy is relaxed due to the multiple collisions occurring inside the nuclei, increasing up to around 9 MeV at excitation energies closer to 100 MeV. However, in spite of the accuracy is degraded, the resolution is better at higher values, being around 9-10%, coming the main limitation from the experimental setup. In this sense, some potential improvements were proposed in order to minimize the impact of the setup in the accuracy of this measurement. The most limiting source to the experimental accuracy was the straggling induced by the target and the silicon tracker. Combining some of the different improvements studied, an experimental accuracy of around 3 MeV could be obtained.

The impact of the δ-electrons production in ^{238}U*(p,2p)*+fission reactions was also matter of study. For light nuclei such as carbon or boron, the number of δ-electrons produced in *(p,2p)* reactions is negligible. However, for heavier nuclei like uranium or lead, the energy lost in the target will be high enough to produce a huge number of electrons, making our analysis really complicated. New R3BRoot simulations were performed to investigate this effect, confirming the high multiplicity of δ-electrons reaching the tracking detector. In order to reduce this multiplicity and separate proton from electron signals, the effect of shielding the detectors with 10 μm thickness layers of different materials was investigated. This study showed that the best material to shield the detectors is gold, reducing the δ-electrons signals measured by the tracker by a factor of 2. These conclusions were supported comparing our simulation with experimental measurements carried out at GSI, confirming also that simulation reproduces correctly some other features in the generation and propagation of δ-electrons.

Thus, the proposed experiment using *(p,2p)*-induced fission reactions is expected to produce novel results in order to increase the understanding of the fission process as well as to define new observables to constrain model calculations. As it has been widely explained, the most interesting one will be the direct measurement of the excitation energy. In particular, this observable will allow to study more in detail how the excitation energy affects to the symmetry of the fission fragments distribution. In figure 4.23, the effect of the excitation energy in the transition from asymmetric to symmetric fission is simulated. This can be one of the interesting results that will be extracted from *(p,2p)*-induced fission reactions measurements.

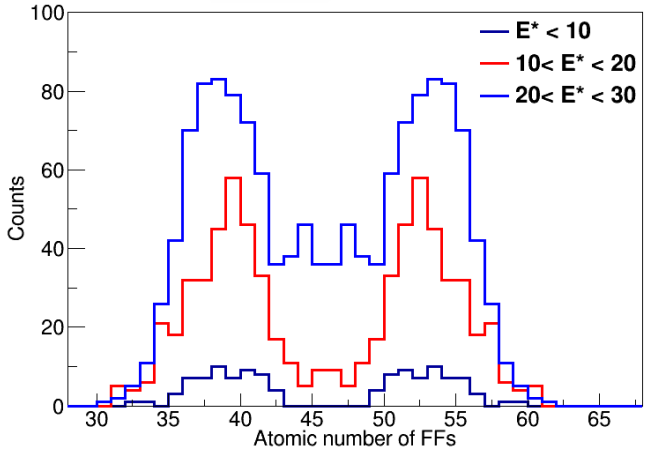

Figure 4.23: *Simulation of the evolution of the atomic number with the excitation energy for fission fragments produced in a reaction ^{238}U (p,2p)+fission.*

USC
UNIVERSIDADE
DE SANTIAGO
DE COMPOSTELA

Conclusions

In the present work, the fission reactions ^{236}U+U and ^{236}U+Al at 720A MeV in inverse kinematics were studied. The use of the highly efficient SOFIA setup allowed for the complete identification, in atomic and mass number, of both fission fragments simultaneously [27]. The atomic number of the fission fragments was reconstructed from the energy loss measurements performed in a double multisampling ionization chamber (Twin MUSIC), while the mass number was obtained from the magnetic rigidity of the fission fragments, reconstructed using multiwire proportional counters (MWPC) to track the positions upstream and downstream the ALADIN magnet and time-of-flight measurements.

This complete identification allowed for the study of observables sensitive to pre- and postsaddle fission dynamics. Moreover, the large range of excitation energies and deformations covered by ^{236}U made it suitable to perform these studies. For the presaddle stage, we analyzed the partial fission yields and the standard deviation of the fission fragments atomic number distribution for both fission reactions as a function of the sum of the final fission fragments atomic number. The results showed very similar values regarding the target, leading us to conclude that there is no dependence with the target used to induce the fission process. In addition, the comparison with other published data for different uranium isotopes, namely ^{238}U from [30] and ^{234}U from [31] showed good agreement with our data, suggesting also that these observables does not present significant dependence with different uranium nuclei. Furthermore, the average neutron number over the atomic number of the final fission fragments, sensitive to pre- and postsaddle dynamics, was analyzed. Studying the behaviour of this parameter as a function of $Z_1 + Z_2$, we observed a decrease for lighter Z_1+Z_2 since the excitation energies for lighter systems are higher, being able to evaporate more neutrons. Again, similar results for reactions induced in different targets are obtained, which can be explained in terms of the limiting fragmentation hypothesis [118, 119].

In order to access to typical fission timescales, model calculations are needed to constrain the value of the dissipation parameter coupling intrinsic and collective degrees of freedom. Our results were compared to calculations making use of the intra-nuclear cascade [128] and the abrasion models [80] coupled to the deexcitation code ABLA07 [123]. We found that the intrinsic properties of the prefragment after the collision, calculated by both reaction models, differed specifically on the angular momentum gained by the prefragment, being around 10 $\hbar$ in ABRABLA and 6 to 7 times higher in INCL. In this sense, the INCL calculations did not reproduce the partial fission yields, overestimating them and suggesting that this angular momentum gained by the prefragment could be too high. The explanation can be found in terms of the different approaches that both codes use to calculate the angular momentum. Even though INCL produced very accurate results in the past to describe nucleon-nucleus collisions, these calculations show worst results for the nucleus-nucleus collisions performed in this work.

To reproduce the width of the atomic number distribution, the level densities also play a significant role. Specifically, collective effects, taking into account rotations and vibrations of the nuclear constituents, are included in their description. We also studied the behaviour of the excitation energy at saddle point with and without considering them in the level density calculations. We observe a non-expected behaviour of the excitation energy at saddle when collective effects are considered, leading to a incorrect description of the data obtained for the width of the fission fragments atomic number distribution. The conclusion is that the collective effects could be not correctly described in the deexcitation code, that is still under investigation.

Regarding the average neutron excess of the fission fragments as a function of $Z_1 + Z_2$, no significant differences were found with different calculations, suggesting that the neutron evaporation from the initial state to the scission point is mainly governed by the excitation energy acquired by the prefragment after the collision, that was very similar in both codes. The sensitivity of the calculations to the angular momentum and the collective effects in the description of the analyzed observables could open a window for future investigations.

Considering that the better description of the data is obtained using ABRABLA without collective effects, we ran different calculations to constrain the value of the dissipation parameter at presaddle and postsaddle stages. We also compared time-dependent calculations to Bohr-Wheeler

statistical approach or the stationary Kramers approach, confirming that these two models used for describing the fission process without dynamical considerations are not suitable. Regarding the values of the dissipation coefficient, we have concluded that the most suitable ones result to be $\beta_{gs} = (4.5 \pm 1.0) \cdot 10^{21} s^{-1}$ and $\beta_{ss} = (7.5 \pm 2.0) \cdot 10^{21} s^{-1}$. For the presaddle dissipation parameter, this value was found to be in very good agreement with other published data using different fission induced reactions. The postsaddle dissipation parameter found in this work is rather similar to the presaddle one and agree the conclusions pictured by Rodriguez and collaborators [70] that there is no significant dependence on this parameter with the deformations. This conclusion is even better supported in this work as the range of deformations covered by ^{236}U is larger. Some other works, using fusion-induced reactions [72, 74, 75], showed more discrepancies between both values, but the high angular momentum acquired by the fissioning systems could mislead the conclusions, so the fragmentation-induced fission reactions studied in this work are more suitable to study postsaddle dynamical effects.

Finally, we tried to go a step further in the understanding of the fission process searching for new approaches to study fission in inverse kinematics. One of the main limitations in the study of fission in inverse kinematics is the unknown excitation energy gained in the process. To overcome this limitation, we suggest to use of *(p,2p)* reactions to induce fission. We proposed to improve the experimental setup used in the present work with the aim of measuring the excitation energy of the fissioning system and introduce more constraints in the dynamical description of the process. This new experimental setup would combine the SOFIA setup with the R^{3}B (Reactions with Relativistic Radioactive Beams) detectors, consisting of the CALIFA proton calorimeter and a silicon tracker that will surround the liquid hydrogen target region. Using this experimental configuration, the kinematics of the two outgoing *(p,2p)* protons can be measured with reasonable accuracy and the excitation energy gained by the remnant nucleus undergoing fission can be obtained using the missing mass spectroscopy technique.

We studied the expected resolution in the excitation energy reconstruction with our new experimental setup for the reaction ^{238}U*(p,2p)*+fission. We found a experimental accuracy value of around 4.6 MeV in the determination of this value. The different sources affecting to the accuracy of the measurement were studied in order to improve the experimental apparatus, finding that the most limiting source is the straggling induced by the silicon tracker and the target. Different improvements were proposed, allowing to

achieve an accuracy of around 3 MeV combining them. After that, we found that the CALIFA energy resolution needs to be improved if we aim to go to a much more accurate measurement. This is of special importance if we want to measure fission barriers. Also, the accuracy over a large range of excitation energies was investigated, finding that for higher excitation energies, the resolution improves, so any future upgrade will have more impact in excitation energies between 5 and 40 MeV, which are the typical ranges of excitation energy presented in *(p,2p)*-induced fission reactions.

Additionally, the impact of the δ-electrons production in ^{238}U*(p,2p)*-induced fission reactions was matter of study. Due to the large atomic number of the projectile, the production of δ-electrons inside the target is not negligible. These electrons produce energy signals in the tracker that can not be distinguished from the proton ones, complicating further analysis. We proposed to shield the tracker in order to reduce these signals. Simulations with different materials were carried out, finding that shielding with a 10 μm gold layer was the most suitable material for this task, reducing the detector multiplicity by a factor of 2. Our simulations were benchmarked with experimental data obtained from a beam test carried out at GSI using the reaction ^{208}Pb+CH_2 at 500A MeV. We have compared the particle multiplicities of the silicon tracker measured in this experiment to our simulations, as well as other features such as the angular distribution of the δ-electrons or their energy deposition, finding very good agreement between the simulation results and the experimental data. The simulations performed in this part of the work shed valuable information for the experiments performed during the GSI 2021 experimental campaign.

USC
UNIVERSIDADE
DE SANTIAGO
DE COMPOSTELA

Resumo en galego

Introdución

Dende o seu descubrimento en 1939 por O. Hahn, F. Strassman, L. Meitner e O.R. Frisch, a fisión nuclear representou o proceso de decaemento máis fascinante e complexo do núcleo atómico. O decaemento dun núcleo excitado por fisión pode describirse como un proceso en dúas etapas. Na primeira, o núcleo excitado evoluciona dende o seu estado inicial ata un estado intermedio chamado punto de cadeira, definido pola altura da barreira de fisión. Cando o sistema é capaz de superar este estado intermedio, a fisión producirase de xeito irrevogable, ata o punto de escisión, a partir do cal prodúcese a separación en dous fragmentos máis lixeiros, coñecidos coma fragmentos de fisión. Non obstante, a pesar da súa aparente sinxeleza, o gran número de graos de liberdade presentes neste proceso fai que a súa descrición microscópica sexa moi complexa.

A primeira interpretación teórica foi proposta por Bohr e Wheeler, baseada no modelo de gota líquida, en 1939. Esta explicación, en termos puramente estatísticos, tivo bastante éxito ata principios dos anos oitenta, onde non foi capaz de describir os observables experimentais obtidos no experimento de Grangé, 1981, o cal demostrou que o proceso de fisión precisa unha descrición dinámica que teña en conta o acoplamento entre graos de liberdade intrínsecos e colectivos. Os graos intrínsecos de liberdade corresponden aos estados individuais dos nucleóns e os colectivos están asociados a movementos entre nucleóns, como rotacións ou deformacións. Para isto, as aproximacións de campo medio dependentes do tempo, como Hartree-Fock, permiten unha descrición cuasi-microscópica do proceso. Outros, como os que empregaremos neste traballo, están baseados en teorías do transporte mediante ecuacións de Langevin ou Fokker-Planck. Neste caso, introducimos un coeficiente de disipación para acoplar os graos de liberdade intrínsecos e colectivos, describindo a transformación da enerxía de excitación interna en deformación do estado inicial ao punto de cadeira e a posterior disipación ao punto de escisión. Nestas aproximacións, é importante

introducir o tempo de tránsito que precisa o sistema para evolucionar ata o punto de cadeira e o tempo que pasa ata chegar ao punto de escisión.

O obxectivo deste traballo estará centrado no estudo da dinámica de fisión utilizando reaccións de fisión inducidas en núcleos de ^{236}U. A nivel experimental, este estudo require determinar os tempos típicos de fisión, o cal é unha tarefa complexa. Algunhas técnicas experimentais, coma a denominada "crystal blocking" son capaces de darnos unha medida directa destes tempos. Non obstante, a sensibilidade destes métodos só nos permitirán acceder aos límites superiores dentro do proceso de fisión. Outros métodos permiten acceder a estes tempos medindo a multiplicidade de partículas lixeiras, principalmente neutróns, ou de raios γ emitidas antes do punto de escisión, funcionando por tanto coma reloxos do tempo de fisión. Porén, isto daríanos o tempo total de fisión, xa que non podemos distinguir experimentalmente se estas partículas se emitiron antes ou despois do punto de cadeira.

As condicións máis axeitadas para estudar a dinámica de fisión obtéñense cando o sistema fisionante presenta alta enerxía de excitación e baixo momento angular e deformación. Neste traballo, buscaremos observables sensibles á dinámica de fisión para estudar os tempos típicos dende o estado inicial ata o punto de cadeira, e dende este punto ao punto de escisión. En concreto, analizaremos as seccións eficaces parciais e as anchuras da distribución de número atómico dos fragmentos de fisión, sensibles ao que ocorre antes do punto de cadeira e o exceso de neutróns promedio, sensible a ambas etapas. Estes observables serán estudados en función da suma do número atómico dos fragmentos de fisión.

Para realizar este estudo, utilizaremos proxectís de ^{236}U para inducir a fisión en cinemática inversa. Este núcleo permitiranos cubrir un amplo rango de deformación comparado cos núcleos que se utilizaron noutras investigacións, coma o ^{208}Pb, por exemplo. Deste xeito, estudaremos a sensibilidade que presentan os nosos observables ao parámetro de disipación na primeira e na segunda etapa da fisión. Ademais, poderemos restrinxir o seu valor e ver a súa posible dependencia coa deformación. A relevancia deste estudo atópase nos diferentes resultados obtidos para este parámetro o longo dos anos. Aínda que o valor para a etapa que vai dende o estado inicial ata o punto de cadeira está bastante establecido arredor de $\beta_{gs} = 4.5 \cdot 10^{21} s^{-1}$, atopamos máis discrepancia no coeficiente de disipación dende o punto de cadeira ata o punto de escisión. Para realizar este estudo, utilizaremos distintos modelos de cálculo, coma son INCL e ABRABLA.

A maiores, queremos ampliar o noso estudo avaliando a influencia do

momento angular na descrición dos nosos observables experimentais. Tamén queremos ver como afectan as densidades de niveis na súa descrición, centrándonos no rol dos efectos colectivos.

Metodoloxía experimental

Para levar a cabo o noso estudo, realizouse un experimento nas instalacións do laboratorio internacional GSI, en Alemaña, no ano 2014. As reaccións de fisión que se pretenden estudar son ^{236}U+Al e ^{236}U+U. Para identificar tanto o núcleo fisionante de ^{236}U coma os fragmentos de fisión, utilizouse o dispositivo experimental SOFIA (correspondente as siglas en inglés de estudos de fisión usando ALADIN). O núcleo de ^{236}U foi producido nunha reacción de fragmentación dun feixe primario de ^{238}U sobre un branco de berilio, acelerado ata unha enerxía de 1A GeV tras pasar por un acelerador lineal (UNILAC) e un sincrotrón (SIS18). Nesta reacción prodúcense un cóctel de núcleos exóticos que atravesan o separador de fragmentos FRS e chegan á sala onde está o noso dispositivo experimental (Cave C).

O feixe secundario de ^{236}U identifícase usando a técnica experimental ΔE-Bρ-ToF. Nunha cámara de ionización triple (TriMUSIC) medimos as perdas de enerxía dos ións que chegan tras pasar polo FRS, o que nos permitirá obter o número atómico. Utilizando dous centelleadores, somos capaces de medir o tempo de voo (ToF) dos feixes secundarios. Combinando esta última medida coas posicións dos núcleos, medidas con detectores multifíos (MWPC) podemos reconstruír a rixidez magnética ($B\rho$) utilizando a ecuación seguinte:

$$B\rho = \frac{p}{Q} = \frac{A}{q \times e} u\beta\gamma c$$

onde B é o campo magnético [T], ρ o raio de curvatura do ión [m], p o momento do ión [kg m/s], q é a carga atómica, A é o número másico, e a carga elemental [C], u a masa atómica, β é a velocidade do ión partida pola velocidade da luz, γ o factor de Lorentz e c a velocidade da luz [m/s]. Deste xeito, podemos identificar o núcleo de ^{236}U, diferenciandoo do resto de núcleos que chegan á nosa sala experimental e rexeitando estados de carga.

Posteriormente, este núcleo inducirá reacción de fisión nun branco activo formado por láminas de distintos materiais, en concreto uranio, aluminio e chumbo, permitíndonos identificar en cal delas tivo lugar a reacción.

Tras producirse a reacción de fisión, fórmanse dous fragmentos de fisión que se emiten formando un cono en dirección cara adiante e son detectados

polos detectores de SOFIA que se atopan tralo branco, utilizando o imán ALADIN para deflectalos e poder reconstruír a súa rixidez magnética. Realizando un procedemento análogo ao explicado para o feixe secundario, estes núcleos son detectados en número atómico a partir da súa perda de enerxía nunha cámara de ionización dobre (TwinMUSIC). A medida do seu tempo de voo lévase a cabo utilizando un centelleador á entrada do dispositivo experimental e un muro de tempo de voo (ToF Wall). Para poder reconstruír a rixidez magnética, utilizamos dúas cámaras multifíos, unha situada antes do imán e outra situada despois. O ángulo polar dos fragmentos de fisión mídese na TwinMUSIC.

Deste xeito, somos capaces de identificar os dous fragmentos de fisión en número atómico e másico de maneira simultánea. Isto permitiranos medir unha serie de observables grazas aos que poderemos estudar a dinámica de fisión, como se explicará no seguinte apartado.

Resultados da investigación da dinámica de fisión

Primeiramente, analizamos os observables que son sensibles á primeira etapa do proceso de fisión, ata o punto de cadeira. Comezamos por analizar as seccións eficaces parciais obtidas para as reacción ^{236}U+Al e ^{236}U+U, en función da suma dos números atómicos dos fragmentos de fisión, $Z_1 + Z_2$. Este observable é sensible á dinámica de fisión xa que as seccións eficaces están relacionadas coa enerxía de excitación e co tempo de transito que o sistema necesita para evolucionar ata o punto de cadeira. Como no experimento soamente se gardaron datos baixo a condición de fisión, e non baixo a condición de feixe, o que realmente analizaremos serán os rendementos parciais de cada sistema fisionante $Z_1 + Z_2$, dividindo o número de fisións para cada sistema fronte ao total. Aquí atopamos que na reacción ^{236}U+U, o sistema máis producido é o $Z_1 + Z_2 = 92$. Isto débese a que o branco de uranio, por presentar un alto número atómico, inducirá a fisión por interacción co campo electromagnético ou Coulombiano (Coulex). Como neste tipo de fisións os núcleos apenas se tocan, non arrincamos ningún protón e a enerxía de excitación adquirida é baixa para poder evaporalo. Para as reaccións, ^{236}U+Al, o sistema máis producido volve a ser o $Z_1 + Z_2 = 92$, pero moito menos que o anterior xa que o campo coulombiano é máis débil. Para poder comparar os rendementos parciais de cada reacción, podemos substraer a contribución coulombiana dominante nas reaccións producidas no branco de uranio. Así, tras esta substracción,

observamos un moi bo acordo entre os resultados para ambos brancos, suxerindo que non existe unha dependencia significativa entre ambos. Tamén comparamos os nosos resultados con outros datos publicados, en concreto para a reacción ^{238}U+CH_2 a enerxías de 1A GeV, atopando bo acordo para sistemas fisionantes lixeiros, onde tódalas fisións serían inducidas por carbono.

Agora analizamos as anchuras das distribucións de número atómico dos fragmentos de fisión, que teñen relación directa coa temperatura no punto de cadeira, é dicir, coa enerxía de excitación coa que o sistema chega a este punto. De novo analizaránse en función de $Z_1 + Z_2$. Os sistemas que se estudaron aquí foron os que presentaban $Z_1 + Z_2 < 91$, co fin de evitar contribucións asimétricas procedentes da fisión inducida por coulex. O valor destas anchuras aumenta segundo diminúe o $Z_1 + Z_2$, xa que a enerxía de excitación aumenta. De novo, atopamos un bo acordo entre os datos obtidos para as dúas reaccións de fisión que estamos a analizar, como pasara co anterior observable. Isto apoia a conclusión, á que xa se chegou en traballos anteriores, de que non hai dependencia co branco. A explicación podémola atopar no concepto coñecido coma límite de fragmentación, que nos di que a enerxías suficientemente altas, por riba de 400A MeV, os produtos de fragmentación non dependen do branco no que se induce a reación. Tamén buscamos apoiar os nosos datos con outros datos experimentais para fisión inducida con distintos núcleos de uranio. En concreto, utilizamos as reaccións de fisión ^{238}U+CH_2 a 1A GeV e ^{234}U+Pb a 420A MeV. Para os sistemas máis pesados, atopouse un moi bo acordo entre tódolos datos experimentais, independentemente do núcleo de uranio e da reacción utilizada. Para sistemas máis lixeiros, $Z_1+Z_2 < 84$, atopouse algunha pequena discrepancia. Estas discrepancias poden entenderse coma pequenas diferencias nas enerxías de excitación que gañan os núcleos trala reacción ou en diferencias debida a desviacións estatísticas. En calquera caso, a conclusión segue a ser que non hai unha dependencia relevante para este observable nin co branco utilizado nin co núcleo de uranio.

Coa fin de estudar a dinámica de fisión, apoiarémonos en distintos modelos de cálculo para describir os nosos observables. A colisión entre o proxectil e o branco descríbese xeralmente coma unha reacción de fragmentación en dúas etapas. A primeira sería a colisión por si mesma, que leva a formación dun núcleo composto trala perda de protóns e neutróns, e o subsecuente proceso de desexcitación por medio de evaporación de nucleóns ou fisión. A primeira parte modelarase utilizando o modelo xeométrico de abrasión ou o modelo dinámico da cascada intra-nuclear. Ambos modelos acoplaranse ao modelo de desexcitación ABLA07.

Investigáronse as principais características destes modelos coa fin de atopar o máis axeitado para a descrición da dinámica da fisión. Observouse que ambos diferían significativamente no momento angular gañado polo prefragmento trala colisión. Outros factores coma a enerxía de excitación e o número másico do prefragmento eran máis similares. Tamén se visualizou a enerxía de excitación coa que o sistema chegaba ao punto de cadeira, calculada polo modelo de desexcitación. Viuse unha diferenza significativa deste parámetro cando tiñamos en conta os efectos colectivos na descrición da densidade de niveles e cando non, suxerindo que pode haber un problema na descrición destes.

Comparando os resultados dos modelos cos datos experimentais dos nosos observables, vimos que INCL non é capaz de reproducir o comportamento dos rendementos parciais de fisión, sobreestimando moito os datos para os $Z_1 + Z_2$ máis lixeiros. Isto achacouse ao momento angular, xa que un maior momento angular reducirá a probabilidade de fisión. Polo tanto, concluímos que o momento dado por ABRABLA semella máis axeitado. Os efectos colectivos non afectan na descrición deste observable, aínda que si varían a sección eficaz total de fisión, suxerindo que teñen efecto na probabilidade de fisión pero non na produción parcial de cada $Z_1 + Z_2$.

Na descrición das anchuras da distribución da carga dos fragmentos de fisión, en función de $Z_1 + Z_2$, atopamos diferenzas importantes entre considerar ou non os efectos colectivos. Cando estes se teñen en conta, observamos non só unha subestimación dos datos experimentais, se non unha baixada das anchuras dadas polo cálculo, algo que non se observa nin nos nosos datos nin noutras publicacións. Por tanto, para reproducir ambos observables, usaremos ABRABLA sen efectos colectivos.

Utilizando esta configuración para os cálculos, estudamos o valor do parámetro de disipación que mellor os describe. Comparamos tamén estes cálculos con cálculos que non teñen en conta un tratamento dinámico do proceso de fisión, utilizando as aproximación de Bohr-Wheeler ou Kramers. Estes cálculos non son capaces de reproducir os datos, poñéndose unha vez máis de manifesto a necesidade de incluír un tratamento dinámico. Neste sentido, o parámetro de disipación que mellor describe os datos sería $\beta_{ss} = (4.5 \pm 1.0) \cdot 10^{21} s^{-1}$, en bo acordo co publicado noutros traballos.

Para analizar a dinámica do proceso de fisión tralo punto de cadeira, utilizamos o exceso de neutróns promedio, definido coma o número de neutróns entre o Z dun determinado fragmento de fisión. Este observable é sensible á evaporación de neutróns dende a configuración inicial ata o punto de escisión, polo que restrinxindo a dinámica antes do punto de

cadeira cos anteriores observables, accederemos a información do que ocorre entre o punto de cadeira e o punto de escisión. O valor promedio deste observable aumenta conforme diminúe $Z_1 + Z_2$, xa que os sistemas fisionantes máis lixeiros prodúcense en colisións máis violentas con maior enerxía de excitación, sendo capaces de evaporar maior número de neutróns. Atopamos de novo bo acordo entre os valores obtidos para as reaccións de fisión inducidas no branco de uranio e no branco de aluminio, para os $Z_1 + Z_2$ no que a fisión inducida por fragmentación é dominante.

Do mesmo xeito que para os anteriores observables, comparamos os resultados experimentais con modelos de cálculo, coa fin de estudar o valor do parámetro de disipación tralo punto de cadeira. Co fin de ser consistentes cas anteriores pesquisas, utilizamos ABRABLA sen efectos colectivos, aínda que aquí non se atoparon diferenzas relevantes entre os distintos cálculos, suxerindo que o parámetro clave é a enerxía de excitación. De novo, mostrouse que un tratamento puramente estatístico non describe os datos. Os cálculos dinámicos que atopan mellor acordo cos datos son aqueles que teñen un valor do parámetro de disipación nesta etapa de $\beta_{ss} = (7.5 \pm 2.0) \cdot 10^{21} s^{-1}$. Isto indica que non atopamos grandes diferenzas entre o parámetro de disipación para describir o proceso ata o punto de cadeira e ata o de escisión, suxerindo que non hai unha dependencia significativa coa deformación.

Novos enfoques para o estudo de fisión en cinemática inversa

Nesta última parte, propoñemos mellorar a técnica experimental coa fin de superar unha das maiores limitacións das investigacións actuais da fisión de núcleos exóticos a enerxías relativistas en cinemática inversa, que é a imposibilidade de medir ou restrinxir a enerxía de excitación inicial que acada o sistema fisionante. Nas reaccións de fisión inducidas por fragmentación ou espalación, esta enerxía pode ser avaliada por medio de modelos de cálculo. Na fisión inducida por coulex, a enerxía de excitación gañada polo sistema fisionante corresponde ao rango cuberto pola resonancia dipolar xigante (GDR), que tipicamente se atopa entre 5 e 20 MeV.

Unha nova técnica para realizar este tipo de estudos sería o uso de reaccións de dispersión cuasilibre *(p,2p)* coa fin de inducir o proceso de fisión. Este mecanismo de reacción vai permitir determinar a enerxía de excitación que se leva o remanente *(A-1, Z-1)* que vai fisionar. A idea consiste en utilizar a espectroscopía de masa perdida para determinar dita enerxía. A partir da medida da enerxía cinética dos protóns saíntes así como da

determinación das súas traxectorias, poderemos reconstruír o cuadrimomento do sistema e extraer a enerxía de excitación con boa resolución. A nivel técnico, esta proposta consiste en combinar o xa coñecido dispositivo SOFIA con detectores para medir os protóns ao redor da rexión na que se atopa o branco. Estes detectores serán un detector de silicio e o calorímetro CALIFA. A reacción inducirase nun branco de hidróxeno líquido usando proxectís de ^{238}U a 500A MeV.

Coa fin de estudar a viabilidade deste tipo de investigación, leváronse a cabo simulacións realistas utilizando o programa R3BRoot. Simulouse o dispositivo experimental arredor do branco para estudar a precisión coa que seríamos capaces de reconstruír a enerxía de excitación e propoñer futuras melloras ao dispositivo actual. Utilizando a técnica da espectroscopía de masa perdida, reconstruíuse por simulación a precisión experimental simulando unha reacción *(p,2p)* usando proxectís de uranio a 500A MeV, obtendo unha precisión na reconstrución da enerxía de excitación de arredor de 4.6 MeV. A partir deste resultado, debulláronse as distintas contribucións que afectaban a dita reconstrución, entre as que se atopaban a dispersión angular e enerxía do branco e do detector de silicio así coma a resolución experimental dos detectores. Atopouse que o maior efecto vén da dispersión introducida polo detector de silicio e o branco. Tendo isto en conta, propuxéronse melloras no dispositivo experimental co fin de incrementar a precisión da medida. Aplicando todas elas, concluíuse que poderíamos ser capaces de reconstruír a enerxía de excitación cunha precisión arredor de 3 MeV. Neste caso, o factor limitante sería a resolución en enerxía de CALIFA, polo que toda futura mellora ha de pasar por mellorar este parámetro.

Estudouse tamén como variaba a precisión desta reconstrución co valor da enerxía de excitación, xa que sabemos que canto maior é esta, o comportamento de dispersión cuasilibre da reacción pérdese debido ás múltiples colisións que se producen entre proxectil e branco. Observouse que a precisión diminúe conforme a enerxía de excitación aumenta, pero a resolución mellora en rangos maiores de enerxía de excitación. Entre 5 e 40 MeV de enerxía de excitación, que son os rangos típicos para estas reaccións, unha mellora no dispositivo experimental conlevaría a unha mellora substancial da resolución.

Por último, investigamos o impacto da produción de electróns δ no branco. Cando as partículas cargadas atravesan dito branco, xerarán este tipo de electróns froito da ionización producida. Isto é especialmente problemático cando estes electróns chegan ao detector de silicio, puidendo confundirse a enerxía depositada por eles cos sinais que deixan os protóns, de xeito que

se dificulte a súa identificación. Ao fío disto, investigouse a posibilidade de blindar os detectores con láminas de diferentes materiais e de 10 μm de espesor. O espesor da lámina elixiuse en bo compromiso entre realizar unha blindaxe eficiente e inducir a mínima dispersión angular e en enerxía sobre os protóns. Observouse que o ouro é capaz de blindar de xeito eficaz os detectores de silicio, reducindo a multiplicidade de electróns δ nun factor 2. Coa fin de validar as nosas simulacións, utilizamos datos experimentais adquiridos no GSI. Esta comparativa permitiunos concluír que o acordo entre simulación e datos experimentais en canto as multiplicidades do detector é bo, cunha marxe de confianza de aproximadamente un 25 %. Os datos tamén puxeron de manifesto a utilidade da blindaxe de ouro. Outras características da produción dos electróns δ, coma a súa distribución angular ou o depósito de enerxía, están perfectamente reproducidos pola simulación. Estes resultados aportaron valiosa información para os primeiros experimentos levados a cabo na campaña experimental de 2021 no GSI, utilizando esta nova técnica de medida.

USC UNIVERSIDADE DE SANTIAGO DE COMPOSTELA

USC
UNIVERSIDADE
DE SANTIAGO
DE COMPOSTELA

Bibliography

[1] C Amsler. "The discovery of the atomic nucleus". In: *Nuclear and Particle Physics*. IOP Publishing, 2015.

[2] JE Fergusson. "The history of the discovery of nuclear fission". In: *Foundations of Chemistry* 13.2 (2011), p. 145.

[3] L Meitner and O R Frisch. "Disintegration of uranium by neutrons: a new type of nuclear reaction". In: *Nature* 143.3615 (1939), pp. 239–240.

[4] O Hahn and F Strassmann. "Concerning the existence of alkaline earth metals resulting from neutron irradiation of uranium". In: *Naturwissenschaften* 27.11 (1939).

[5] N Bohr and J A Wheeler. "The mechanism of nuclear fission". In: *Physical Review* 56.5 (1939), p. 426.

[6] W Wlazło et al. "Cross sections of spallation residues produced in 1A GeV ^{208}Pb on proton reactions". In: *Physical review letters* 84.25 (2000), p. 5736.

[7] HJ Mang. "The self-consistent single-particle model in nuclear physics". In: *Physics Reports* 18.6 (1975), pp. 325–368.

[8] HA Kramers. "Brownian motion in a field of force and the diffusion model of chemical reactions". In: *Physica* 7.4 (1940), pp. 284–304.

[9] P Grangé, L Jun-Qing, and HA Weidenmüller. "Induced nuclear fission viewed as a diffusion process: Transients". In: *Physical Review C* 27.5 (1983), p. 2063.

[10] D Jacquet and M Morjean. "Fission times of excited nuclei: An experimental overview". In: *Progress in Particle and Nuclear Physics* 63.1 (2009), pp. 155–185.

[11] C Eccles et al. "Temperature dependence of nuclear fission time in heavy-ion fusion-fission reactions". In: *Physical Review C* 96.5 (2017), p. 054611.

[12] SA Giuliani et al. "Fission and the r-process nucleosynthesis of translead nuclei in neutron star mergers". In: *Physical Review C* 102.4 (2020), p. 045804.

[13] IV Panov et al. "Calculations of fission rates for r-process nucleosynthesis". In: *Nuclear Physics A* 747.2-4 (2005), pp. 633–654.

[14] S Goriely. "The fundamental role of fission during r-process nucleosynthesis in neutron star mergers". In: *The European Physical Journal A* 51.2 (2015), p. 22.

[15] M Eichler et al. "The role of fission in neutron star mergers and its impact on the r-process peaks". In: *The Astrophysical Journal* 808.1 (2015), p. 30.

[16] JJ Cowan et al. "Origin of the heaviest elements: The rapid neutron-capture process". In: *Reviews of Modern Physics* 93.1 (2021), p. 015002.

[17] GA Cowan. "A natural fission reactor". In: *Scientific American* 235.1 (1976), pp. 36–47.

[18] E B Podgoršak et al. "Radiation physics for medical physicists". In: (2006).

[19] H Nifenecker et al. "Basics of accelerator driven subcritical reactors". In: *Nuclear Instruments and Methods in Physics Research Section A: Accelerators, Spectrometers, Detectors and Associated Equipment* 463.3 (2001), pp. 428–467.

[20] P Armbruster et al. "The recoil separator Lohengrin: Performance and special features for experiments". In: *Nuclear Instruments and Methods* 139 (1976), pp. 213–222.

[21] G Siegert et al. "Nuclear charge distribution of fission products from U 235 (n th), f of the masses 79 to 100". In: *Physical Review C* 14.5 (1976), p. 1864.

[22] M Bernas et al. "Discovery and cross-section measurement of 58 new fission products in projectile-fission of 750· A MeV 238U". In: *Physics Letters B* 415.2 (1997), pp. 111–116.

[23] H Geissel et al. "The GSI projectile fragment separator (FRS): a versatile magnetic system for relativistic heavy ions". In: *Nuclear Instruments and Methods in Physics Research Section B: Beam Interactions with Materials and Atoms* 70.1-4 (1992), pp. 286–297.

[24] KH Schmidt et al. "Relativistic radioactive beams: A new access to nuclear-fission studies". In: *Nuclear Physics A* 665.3-4 (2000), pp. 221–267.

[25] F Farget et al. "Isotopic fission fragment distributions as a deep probe to fusion-fission dynamics". In: *Journal of Physics: Conference Series*. Vol. 420. 1. IOP Publishing. 2013, p. 012119.

[26] M Caamaño et al. "Characterization of the scission point from fission-fragment velocities". In: *Physical Review C* 92.3 (2015), p. 034606.

[27] G Boutoux et al. "The SOFIA experiment". In: *Physics Procedia* 47 (2013), pp. 166–171.

[28] E Pellereau et al. "SOFIA: An innovative setup to measure complete isotopic yield of fission fragments". In: *EPJ Web of Conferences*. Vol. 62. EDP Sciences. 2013, p. 06005.

[29] JL Rodriguez-Sanchez. "Pre- and postsaddle fission dynamics using lead on proton reactions in complete kinematic measurements". PhD dissertation. University of Santiago de Compostela, 2015.

[30] B Jurado et al. "Transient effects in fission from new experimental signatures". In: *Physical review letters* 93.7 (2004), p. 072501.

[31] C Schmitt et al. "Fragmentation of spherical radioactive heavy nuclei as a novel probe of transient effects in fission". In: *Physical Review C* 81.6 (2010), p. 064602.

[32] P Radvanyi. "Quasi-free scattering on nucleons and nuclear fragments". In: *Le Journal de Physique Colloques* 33.C5 (1972), pp. C5–141.

[33] D Cortina-Gil et al. "CALIFA, a Dedicated Calorimeter for the R3B/FAIR". In: *Nuclear Data Sheets* 120 (2014), pp. 99–101.

[34] KH Schmidt and B Jurado. "Entropy driven excitation energy sorting in superfluid fission dynamics". In: *Physical review letters* 104.21 (2010), p. 212501.

[35] T Ichikawa et al. "Contrasting fission potential-energy structure of actinides and mercury isotopes". In: *Physical Review C* 86.2 (2012), p. 024610.

[36] A Gavron. "Angular distribution of neutrons from fission fragments". In: *Physical Review C* 13.6 (1976), p. 2562.

[37] J Benlliure et al. "Signatures of fission dynamics in highly excited nuclei produced in 197Au (800 A MeV) on proton collisions". In: *Nuclear Physics A* 700.1-2 (2002), pp. 469–491.

[38] JF Berger, M Girod, and D Gogny. "Microscopic analysis of collective dynamics in low energy fission". In: *Nuclear Physics A* 428 (1984), pp. 23–36.

[39] P Möller et al. "Nuclear fission modes and fragment mass asymmetries in a five-dimensional deformation space". In: *Nature* 409.6822 (2001), pp. 785–790.

[40] V Weisskopf. "Statistics and nuclear reactions". In: *Physical Review* 52.4 (1937), p. 295.

[41] W Hauser and H Feshbach. "The inelastic scattering of neutrons". In: *Physical review* 87.2 (1952), p. 366.

[42] MG Evans and M Polanyi. "Further considerations on the thermodynamics of chemical equilibria and reaction rates". In: *Transactions of the Faraday Society* 32 (1936), pp. 1333–1360.

[43] KH Schmidt. "About the inconsistency between Bohr-Wheeler transition-state method and Kramers escape rate in nuclear fission". In: *International Journal of Modern Physics E* 18.04 (2009), pp. 850–860.

[44] AJ Sierk. "Macroscopic model of rotating nuclei". In: *Physical Review C* 33.6 (1986), p. 2039.

[45] DW Lang. "The angular momentum-dependence of the nuclear level density". In: *Nuclear Physics* 77.3 (1966), pp. 545–558.

[46] AV Ignatyuk et al. *Fission of pre-actinide nuclei. Excitation functions for the (alpha, f) reaction.* Tech. rep. Inst. of Nuclear Physics, Alma-Ata, USSR, 1975.

[47] A Gavron et al. "Time Scale of Fission at High Angular Momentum". In: *Physical Review Letters* 48.12 (1982), p. 835.

[48] HA Weidenmüller. "Transport theories of heavy-ion reactions". In: *Progress in particle and nuclear physics* 3 (1980), pp. 49–126.

[49] KH Bhatt, P Grangé, and B Hiller. "Nuclear friction and lifetime of induced fission". In: *Physical Review C* 33.3 (1986), p. 954.

[50] B Jurado et al. "A critical analysis of the modelling of dissipation in fission". In: *Nuclear Physics A* 747.1 (2005), pp. 14–43.

[51] B Jurado et al. "Conditions for the manifestation of transient effects in fission". In: *Nuclear Physics A* 757.3-4 (2005), pp. 329–348.

[52] W Ye, N Wang, and J Tian. "Probing nuclear dissipation with particle multiplicity in heavy-ion-induced light fissioning systems". In: *Physical Review C* 90.4 (2014), p. 041604.

[53] P Fröbrich. "On the dynamics of fission of hot nuclei". In: *Nuclear Physics A* 787.1-4 (2007), pp. 170–175.

[54] H Hofmann and JR Nix. "Fission dynamics simplified". In: *Physics Letters B* 122.2 (1983), pp. 117–120.

[55] JB Rosser. "Theory and Application of $\int_0^z e^{-x^2} dx$ and $\int_0^z e^{-p^2y^2} dy \int_0^y e^{-x^2} dx$. Part I. Methods of Computation". In: (1948).

[56] JP Lestone. "Fast method for obtaining finite range corrected potential energy surfaces". In: *Physical Review C* 51.2 (1995), p. 580.

[57] WD Myers and WJ Swiatecki. "The nuclear droplet model for arbitrary shapes". In: *Annals of Physics* 84.1-2 (1974), pp. 186–210.

[58] BD Wilkins, EP Steinberg, and RR Chasman. "Scission-point model of nuclear fission based on deformed-shell effects". In: *Physical Review C* 14.5 (1976), p. 1832.

[59] F Gönnenwein and B Börsig. "Tip model of cold fission". In: *Nuclear Physics A* 530.1 (1991), pp. 27–57.

[60] F Goldenbaum et al. "Fission time evolution with excitation energy from a crystal blocking experiment". In: *Physical review letters* 82.25 (1999), p. 5012.

[61] JD Molitoris et al. "Molecular-orbital study of late-fission times in deep-inelastic u 238+ 238 u collisions". In: *Physical review letters* 70.5 (1993), p. 537.

[62] Th Rubehn et al. "Total and nuclear fission cross sections of U 238 at relativistic energies". In: *Physical Review C* 53.6 (1996), p. 3143.

[63] P Fong. "Statistical theory of nuclear fission: α-particle emission". In: *Physics and chemistry of fission. Proceedings of the second IAEA symposium.* 1969.

[64] SI Mulgin et al. "Shell effects in the symmetric-modal fission of pre-actinide nuclei". In: *Nuclear Physics A* 640.3-4 (1998), pp. 375–388.

[65] JP Lestone. "Determination of the time evolution of fission from particle emission". In: *Physical review letters* 70.15 (1993), p. 2245.

[66] Y Ayyad et al. "Proton-induced fission of 181 Ta at high excitation energies". In: *Physical Review C* 89.5 (2014), p. 054610.

[67] C Schmitt et al. "First experiment on fission transients in highly fissile spherical nuclei produced by fragmentation of radioactive beams". In: *Physical review letters* 99.4 (2007), p. 042701.

[68] C Schmitt et al. "Fragmentation of radioactive beams for tailoring fission transients". In: *International Journal of Modern Physics E* 18.10 (2009), pp. 2150–2154.

[69] JL Rodríguez-Sánchez et al. "Complete characterization of the fission fragments produced in reactions induced by ^{208}Pb projectiles on proton at 500 A MeV". In: *Physical Review C* 91.6 (2015), p. 064616.

[70] JL Rodríguez-Sánchez et al. "Presaddle and postsaddle dissipative effects in fission using complete kinematics measurements". In: *Physical Review C* 94.6 (2016), p. 061601.

[71] P Fröbrich and II Gontchar. "Langevin description of fusion, deep-inelastic collisions and heavy-ion-induced fission". In: *Physics reports* 292.3-4 (1998), pp. 131–237.

[72] P Fröbrich, II Gontchar, and ND Mavlitov. "Langevin fluctuation-dissipation dynamics of hot nuclei: prescission neutron multiplicities and fission probabilities". In: *Nuclear Physics A* 556.2 (1993), pp. 281–306.

[73] PN Nadtochy, GD Adeev, and AV Karpov. "More detailed study of fission dynamics in fusion-fission reactions within a stochastic approach". In: *Physical Review C* 65.6 (2002), p. 064615.

[74] I Diószegi et al. "Fission hindrance in ^{200}Pb measured from giant dipole resonance γ-ray emission". In: *Physical Review C* 63.1 (2000), p. 014611.

[75] NP Shaw et al. "Nuclear viscosity of hot rotating ^{240}Cf". In: *Physical Review C* 61.4 (2000), p. 044612.

[76] JP Lestone and SG McCalla. "Statistical model of heavy-ion fusion-fission reactions". In: *Physical Review C* 79.4 (2009), p. 044611.

[77] W Ye and N Wang. "Significant role of level-density parameters in probing nuclear dissipation with light-ion-induced fission excitation functions". In: *Physical Review C* 87.1 (2013), p. 014610.

[78] A Boudard et al. "Intranuclear cascade model for a comprehensive description of spallation reaction data". In: *Physical Review C* 66.4 (2002), p. 044615.

[79] D Mancusi et al. "Improving the description of proton-induced one-nucleon removal in intranuclear-cascade models". In: *Physical Review C* 91.3 (2015), p. 034602.

[80] JJ Gaimard and KH Schmidt. "A reexamination of the abrasion-ablation model for the description of the nuclear fragmentation reaction". In: *Nuclear Physics A* 531.3-4 (1991), pp. 709–745.

[81] L Grente et al. "The SOFIA experiment: Measurement of 236U fission fragment yields in inverse kinematics". In: *EPJ Web of Conferences*. Vol. 122. EDP Sciences. 2016, p. 01006.

[82] JF Martin et al. "Studies on fission with ALADIN". In: *The European Physical Journal A* 51.12 (2015), pp. 1–8.

[83] P Roussel-Chomaz et al. "Active target as a tool for nuclear spectroscopy and reactions". In: *International Journal of Modern Physics E* 18.10 (2009), pp. 1997–2002.

[84] AN Andreyev et al. "Fission barrier heights for the ultra neutron-deficient nuclei 188Pb and 196Po". In: *Physics Letters B* 312.1-2 (1993), pp. 49–52.

[85] https://www.gsi.de.

[86] P Spädtke et al. "Ion source development at GSI". In: *Review of scientific instruments* 69.2 (1998), pp. 1079–1081.

[87] L Groening. "Concept for controlled transverse emittance transfer within a linac ion beam". In: *Physical Review Special Topics Accelerators and Beams* 14.6 (2011), p. 064201.

[88] P Spiller, L Bozyk, and P Puppel. *SIS18:Intensity Record with Intermediate Charge State Heavy Ions*. Universitatsbibliothek Johann Christian Senckenberg, 2011.

[89] http://www-aladin.gsi.de.

[90] A Magel et al. "First spatial isotopic separation of relativistic uranium projectile fragments". In: *Nuclear Instruments and Methods in Physics Research Section B: Beam Interactions with Materials and Atoms* 94.4 (1994), pp. 548–554.

[91] https://www-win.gsi.de/frs/index.htm.

[92] B Voss. "A low-mass Multi-Sampling Ionization chamber for fission studies". In: *2011 IEEE Nuclear Science Symposium Conference Record*. IEEE. 2011, pp. 1767–1770.

[93] G Charpak et al. "The use of multiwire proportional counters to select and localize charged particles". In: *Nuclear Instruments and Methods* 62.3 (1968), pp. 262–268.

[94] A Bail et al. "Time of flight measurement on the SOFIA experiment". In: *2011 2nd International Conference on Advancements in Nuclear Instrumentation, Measurement Methods and their Applications*. IEEE. 2011, pp. 1–4.

[95] A Ebran et al. "Picosecond resolution on relativistic heavy ions' time-of-flight measurement". In: *Nuclear Instruments and Methods in Physics Research Section A: Accelerators, Spectrometers, Detectors and Associated Equipment* 728 (2013), pp. 40–46.

[96] M Pfützner et al. "New isotopes and isomers produced by the fragmentation of 238U at 1000 MeV/nucleon". In: *Physics Letters B* 444.1-2 (1998), pp. 32–37.

[97] A Chatillon et al. "Experimental study of nuclear fission along the thorium isotopic chain: From asymmetric to symmetric fission". In: *Physical Review C* 99.5 (2019), p. 054628.

[98] JF Martin. "Coulex fission of 234U,235U, 237Np and 238Np studied within the SOFIA experimental program". PhD dissertation. University Paris-Sud, 2014.

[99] Y Yan. "Study of fission of exotic actinides by relativistic reactions". PhD dissertation. University Paris-Sud, 2016.

[100] JP Boutot, J Nussli, and D Vallat. "Recent trends in photomultipliers for nuclear physics". In: *Advances in Electronics and Electron Physics*. Vol. 60. Elsevier, 1983, pp. 223–305.

[101] OB Tarasov and D Bazin. "LISE++: Radioactive beam production with in-flight separators". In: *Nuclear Instruments and Methods in Physics Research Section B: Beam Interactions with Materials and Atoms* 266.19-20 (2008), pp. 4657–4664.

[102] R Janik et al. "Time Projection Chambers with C-pads for heavy ion tracking". In: *Nuclear Instruments and Methods in Physics Research Section A: Accelerators, Spectrometers, Detectors and Associated Equipment* 640.1 (2011), pp. 54–57.

[103] K Lau and J Pyrlik. "Optimization of centroid-finding algorithms for cathode strip chambers". In: *Nuclear Instruments and Methods in Physics Research Section A: Accelerators, Spectrometers, Detectors and Associated Equipment* 366.2-3 (1995), pp. 298–309.

[104] Particle Data Group et al. "Review of particle physics". In: *Progress of Theoretical and Experimental Physics* 2020.8 (2020), p. 083C01.

[105] H Weick et al. "Improved accuracy of the code ATIMA for energy loss of heavy ions in matter". In: *GSI Scientific Report* (2017).

[106] A S Goldhaber and L Island. "Statistical models of fragmentation processes". In: *Physics Letters B* 53.4 (1974), pp. 306–308.

[107] M Caamaño, F Rejmund, and KH Schmidt. "Influence of asymmetry and fissility on even-odd effect in fission-fragment yields". In: *EPJ Web of Conferences*. Vol. 8. EDP Sciences. 2010, p. 03001.

[108] H Newson. "Symmetric and Asymmetric Fission". In: *Physical Review* 122.4 (1961), p. 1224.

[109] A Kelić et al. "Isotopic and velocity distributions of Bi 83 produced in charge-pickup reactions of Pb 82 208 at 1 A GeV". In: *Physical Review C* 70.6 (2004), p. 064608.

[110] P Adrich. "Some notes about motion of the charged particle thorugh the field of a dipole magnet and the mass measurement with the magnetic spectrometer ALADIN". In: *Private Communication* (2002).

[111] JW Boldeman, AR de L Musgrove, and RL Walsh. "Prompt neutrons from 236U fission fragments". In: *Australian Journal of Physics* 24.4 (1971), pp. 821–834.

[112] K Nishio et al. "Multiplicity and energy of neutrons from 235U (nth, f) fission fragments". In: *Nuclear Physics A* 632.4 (1998), pp. 540–558.

[113] AS Vorobyev et al. "Investigation of the prompt neutron emission mechanism in low energy fission of 235,233 U (nth, f) and 252Cf (sf)". In: *EPJ Web of Conferences*. Vol. 8. EDP Sciences. 2010, p. 03004.

[114] EAC Crouch. "Fission-product yields from neutron-induced fission". In: *Atomic data and nuclear data tables* 19.5 (1977), pp. 417–532.

[115] Y Ayyad et al. "Dissipative effects in spallation-induced fission of Pb 208 at high excitation energies". In: *Physical Review C* 91.3 (2015), p. 034601.

[116] JL Rodríguez-Sánchez et al. "Proton-induced fission cross sections on Pb 208 at high kinetic energies". In: *Physical Review C* 90.6 (2014), p. 064606.

[117] WP Alford and BM Spicer. "Nucleon charge-exchange reactions at intermediate energy". In: *Advances in Nuclear Physics* (2002), pp. 1–82.

[118] DE Greiner et al. "Uranium nuclear reactions at 900 MeV/nucleon". In: *Physical Review C* 31.2 (1985), p. 416.

[119] C Paradela et al. "Isotopic production cross sections of residual nuclei in the spallation reaction Xe 136 (200 A MeV)+ p". In: *Physical Review C* 95.4 (2017), p. 044606.

[120] BS Nilsen et al. "Fragmentation cross sections of relativistic Kr 36 84 and Ag 47 109 nuclei in targets from hydrogen to lead". In: *Physical Review C* 52.6 (1995), p. 3277.

[121] R Serber. "Nuclear reactions at high energies". In: *Physical Review* 72.11 (1947), p. 1114.

[122] P Shukla. "Glauber model and the heavy ion reaction cross section". In: *Physical Review C* 67.5 (2003), p. 054607.

[123] A Kelic, M V Ricciardi, and K H Schmidt. "ABLA07 - towards a complete description of the decay channels of a nuclear system from spontaneous fission to multifragmentation". In: *Joint ICTP-IAEA Advanced Workshop on Model Codes for Spallation Reactions*. 2009, pp. 181–221.

[124] RJ Glauber and G Matthiae. "High-energy scattering of protons by nuclei". In: *Nuclear Physics B* 21.2 (1970), pp. 135–157.

[125] PJ Karol. "Nucleus-nucleus reaction cross sections at high energies: Soft-spheres model". In: *Physical Review C* 11.4 (1975), p. 1203.

[126] LF Oliveira, R Donangelo, and JO Rasmussen. "Abrasion-ablation calculations of large fragment yields from relativistic heavy ion reactions". In: *Physical Review C* 19.3 (1979), p. 826.

[127] M de Jong, AV Ignatyuk, and KH Schmidt. "Angular momentum in peripheral fragmentation reactions". In: *Nuclear Physics A* 613.4 (1997), pp. 435–444.

[128] A Boudard et al. "New potentialities of the Liège intranuclear cascade model for reactions induced by nucleons and light charged particles". In: *Physical Review C* 87.1 (2013), p. 014606.

[129] JL Rodríguez-Sánchez et al. "Improvement of one-nucleon removal and total reaction cross sections in the Liège intranuclear-cascade model using Hartree-Fock-Bogoliubov calculations". In: *Physical Review C* 96.5 (2017), p. 054602.

[130] JB Natowitz et al. "Caloric curves and critical behavior in nuclei". In: *Physical Review C* 65.3 (2002), p. 034618.

[131] D Mancusi et al. "Elusiveness of evidence for multifragmentation in 1-GeV proton-nucleus reactions". In: *Physical Review C* 84.6 (2011), p. 064615.

[132] VF Weisskopf and DH Ewing. "On the yield of nuclear reactions with heavy elements". In: *Physical Review* 57.6 (1940), p. 472.

[133] WJ Huang et al. "The AME2016 atomic mass evaluation (I). Evaluation of input data; and adjustment procedures". In: *Chinese Physics C* 41.3 (2017), p. 030002.

[134] R Bass and W von Oertzen. "Proceedings of the Symposium on Deep Inelastic and Fusion Reactions with Heavy Ions". In: (1980).

[135] AR Junghans et al. "Projectile-fragment yields as a probe for the collective enhancement in the nuclear level density". In: *Nuclear Physics A* 629.3-4 (1998), pp. 635–655.

[136] AR Junghans et al. "Collective excitations in hot nuclei-Up to which excitation energy do they persist?" In: *Nuclear Physics, Section A* 1.649 (1999), pp. 214C–217C.

[137] JL Egido and LM Robledo. "Fission Barriers at High Angular Momentum and the Ground State Rotational Band of the Nucleus N 254 o". In: *Physical review letters* 85.6 (2000), p. 1198.

[138] S Pedoux and J Cugnon. "Extension of the Liège intranuclear cascade model at incident energies between 2 and 12 GeV. Aspects of pion production". In: *Nuclear Physics A* 866.1 (2011), pp. 16–36.

[139] J Cugnon, C Volant, and S Vuillier. "Improved intranuclear cascade model for nucleon-nucleus interactions". In: *Nuclear Physics A* 620.4 (1997), pp. 475–509.

[140] JJ Gaardhoje. "Nuclear structure at high excitation energy studied with giant resonances". In: *Annual Review of Nuclear and Particle Science* 42.1 (1992), pp. 483–536.

[141] O Chamberlain and E Segrè. "Proton-proton collisions within lithium nuclei". In: *Physical Review* 87.1 (1952), p. 81.

[142] T Berggren and H Tyrén. "Quasi-free scattering". In: *Annual Review of Nuclear Science* 16.1 (1966), pp. 153–182.

[143] V Panin. "Fully exclusive measurements of quasi-free single-nucleon knockout reactions in inverse kinematics." PhD dissertation. Technische Universität, 2012.

[144] H Tyren, P Hillman, and Th AJ Maris. "High energy (p, 2p) reactions and proton binding energies". In: *Nuclear Physics* 7 (1958), pp. 10–23.

[145] W Henning. "Fission properties of neutron-rich". In: *10th ASRC Workshop, JAEA, Tokai, Japan*. 2013.

[146] LV Chulkov et al. "Quasi-free scattering with 6, 8He beams". In: *Nuclear Physics A* 759.1-2 (2005), pp. 43–63.

[147] D Suzuki. "Missing mass spectroscopy on oxygen isotopes beyond the proton-drip line: mirror symmetry of nuclear shell evolution". In: *The European Physical Journal A* 48.9 (2012), p. 130.

[148] YK Tanaka et al. "Missing-mass spectroscopy of the ^{12}C(p, d) reaction near the η'-meson production threshold". In: *Physical Review C* 97.1 (2018), p. 015202.

[149] C Louchart et al. "The PRESPEC liquid-hydrogen target for in-beam gamma spectroscopy of exotic nuclei at GSI". In: *Nuclear Instruments and Methods in Physics Research Section A: Accelerators, Spectrometers, Detectors and Associated Equipment* 736 (2014), pp. 81–87.

[150] M Borri et al. "Detector production for the R3B Si-tracker". In: *Nuclear Instruments and Methods in Physics Research Section A: Accelerators, Spectrometers, Detectors and Associated Equipment* 836 (2016), pp. 105–112.

[151] E Belau et al. "Charge collection in silicon strip detectors". In: *Nuclear Instruments and Methods in Physics Research* 214.2-3 (1983), pp. 253–260.

[152] M Aguilar et al. "The Alpha Magnetic Spectrometer (AMS) on the International Space Station: Part I–results from the test flight on the space shuttle". In: *Physics Reports* 366.6 (2002), pp. 331–405.

[153] J Alcaraz et al. "The alpha magnetic spectrometer silicon tracker: Performance results with protons and helium nuclei". In: *Nuclear Instruments and Methods in Physics Research Section A: Accelerators, Spectrometers, Detectors and Associated Equipment* 593.3 (2008), pp. 376–398.

[154] V Panin et al. "Exclusive measurements of quasi-free proton scattering reactions in inverse and complete kinematics". In: *Physics Letters B* 753 (2016), pp. 204–210.

[155] H Alvarez-Pol et al. "Performance analysis for the CALIFA Barrel calorimeter of the R3B experiment". In: *Nuclear Instruments and Methods in Physics Research Section A: Accelerators, Spectrometers, Detectors and Associated Equipment* 767 (2014), pp. 453–466.

[156] P Cabanelas et al. "Performance recovery of long CsI (Tl) scintillator crystals with APD-based readout". In: *Nuclear Instruments and Methods in Physics Research Section A: Accelerators, Spectrometers, Detectors and Associated Equipment* (2020), p. 163845.

[157] M Gascon et al. "Test of LAAPDs coupled to CsI (Tl) crystals for the CALIFA R3B/FAIR Calorimeter". In: *IEEE Transactions on Nuclear Science* 57.3 (2010), pp. 1465–1469.

[158] M Bendel et al. "iPhos, a new technique for the CALIFA CsI (Tl) calorimeter". In: *Journal of Physics: Conference Series*. Vol. 587. 1. IOP Publishing. 2015, p. 012049.

[159] O Tengblad et al. "LaBr3 (Ce): LaCl3 (Ce) Phoswich with pulse shape analysis for high energy gamma-ray and proton identification". In: *Nuclear Instruments and Methods in Physics Research Section A: Accelerators, Spectrometers, Detectors and Associated Equipment* 704 (2013), pp. 19–26.

[160] B Gastineau et al. "Design status of the R3B-Glad magnet: Large acceptance superconducting dipole with active shielding, graded coils, large forces and indirect cooling by thermosiphon". In: *IEEE transactions on applied superconductivity* 18.2 (2008), pp. 407–410.

[161] CA Douma et al. "Design studies for the NeuLAND VETO detector". In: *Journal of Physics: Conference Series*. Vol. 1024. 1. IOP Publishing. 2018, p. 012027.

[162] CA Douma et al. "Investigation of background reduction techniques for the NeuLAND neutron detector". In: *Nuclear Instruments and Methods in Physics Research Section A: Accelerators, Spectrometers, Detectors and Associated Equipment* 930 (2019), pp. 203–209.

[163] D Bertini. "R3BRoot, simulation and analysis framework for the R3B experiment at FAIR". In: *Journal of Physics: Conference Series*. Vol. 331. 3. IOP Publishing. 2011, p. 032036.

[164] D Kresan et al. "Event reconstruction and analysis in the R3BRoot framework". In: *Journal of Physics: Conference Series*. Vol. 523. 1. IOP Publishing. 2014, p. 012034.

[165] S Agostinelli et al. "GEANT4-a simulation toolkit". In: *Nuclear instruments and methods in physics research section A: Accelerators, Spectrometers, Detectors and Associated Equipment* 506.3 (2003), pp. 250–303.

[166] B Pietras et al. "CALIFA Barrel prototype detector characterisation". In: *Nuclear Instruments and Methods in Physics Research Section A: Accelerators, Spectrometers, Detectors and Associated Equipment* 729 (2013), pp. 77–84.

[167] B Pietras et al. "First testing of the CALIFA Barrel Demonstrator". In: *Nuclear Instruments and Methods in Physics Research Section A: Accelerators, Spectrometers, Detectors and Associated Equipment* 814 (2016), pp. 56–65.

[168] C Anderson et al. "Delta-ray Production in MCNP 6.2. 0". In: *Physics Procedia* 90 (2017), pp. 229–236.

[169] SB Reichert. "Detector Development for High Precision Measurements of (p, 2p) Reactions in Inverse Kinematics using the Missing Mass Spectroscopy". PhD dissertation. Technische Universität München, 2018.

USC UNIVERSIDADE DE SANTIAGO DE COMPOSTELA

USC
UNIVERSIDADE
DE SANTIAGO
DE COMPOSTELA

This work was partially supported by the Spanish "Ministerio de Economía, Industria y Competitividad", under the grant BES-2016-076598.

USC
UNIVERSIDADE
DE SANTIAGO
DE COMPOSTELA